INFRARED PROPERTIES OF THE Si-SiO_2 INTERFACE FROM FIRST PRINCIPLES

THÈSE N^{O} 3259 (2005)

PRÉSENTÉE À LA FACULTÉ SCIENCES DE BASE

Institut de théorie des phénomènes physiques

SECTION DE PHYSIQUE

ÉCOLE POLYTECHNIQUE FÉDÉRALE DE LAUSANNE

POUR L'OBTENTION DU GRADE DE DOCTEUR ÈS SCIENCES

PAR

Feliciano GIUSTINO

laurea in ingegneria nucleare, Politecnico di Torino, Italie
et de nationalité italienne

acceptée sur proposition du jury:

Prof. A. Pasquarello, directeur de thèse
Dr W. Andreoni, rapporteur
Prof. A. Baldereschi, rapporteur
Prof. H. Brune, rapporteur
Prof. X. Gonze, rapporteur

Lausanne, EPFL
2005

Contents

Version abrégée

Cette thèse est dédiée à l'étude des propriétés infrarouges de l'interface entre le silicium et son oxide par des calculs *ab initio*. Dans le but de fournir une description à l'échelle atomique de la permittivité électrique (aussi bien à haute fréquence que statique) et de l'absorption infrarouge à l'interface, on introduit ici deux schémas théoriques dont l'applicabilité est générale.

Premièrement, on développe une méthode pour examiner le comportement de la permittivité électrique à travers l'interface entre deux isolants. A partir de la densité de charge microscopique induite par un champ électrique appliqué, on calcule une permittivité locale qui décrit les variations de la réponse diélectrique sur des échelles de longueur de l'ordre des distances inter-atomiques. L'analyse de cette permittivité locale en termes de fonctions de Wannier localisées permet d'établir une liaison entre la réponse diélectrique et la structure microscopique sousjacente.

Deuxièmement, on introduit une méthode pour le calcul des spectres d'absorption infrarouge transversale et longitudinale des surfaces et des interfaces. D'abord on déduit les expressions pour les spectres d'absorption totale du système consideré. Ensuite on définit une décomposition spatiale qui fournit l'évolution de l'activité infrarouge à travers ce système, permettant ainsi d'associer des éléments spécifiques des spectres aux structures atomiques correspondantes.

En utilisant la première méthode, on détermine le comportement de la permittivité locale à travers plusieurs modèles de l'interface Si-SiO_2. Grâce à cela, on arrive à montrer que la transition diélectrique du silicium à l'oxide est accomplie dans l'espace de quelques angströms seulement, et que la couche interfaciale présente une permittivité accrue par rapport à la silice amorphe. En particulier, il en résulte que l'épaisseur équivalente d'oxide de la couche interfaciale est de $0.2-0.3$ nm inférieure à l'épaisseur physique correspondante. Cela a des conséquences favorables pour la miniaturisation des circuits intégrés sur silicium.

En utilisant la deuxième méthode, on résoud une controverse relative aux déplacements vers l'infrarouge lointain des bandes d'absorption infrarouge à haute fréquence des couches minces d'oxide, qui sont observés lorsque l'on en réduit l'épaisseur. En calculant les spectres d'absorption transversale et longitudinale pour un modèle réaliste de l'interface Si(100)-SiO_2, on arrive à attribuer l'origine microscopique de ces déplacements à l'allongement des liaisons entre les atomes de Si et O dans l'oxide sous-stoechiométrique à l'interface.

Abstract

We study the infrared properties of the Si-SiO_2 interface within a first-principles approach. In order to provide an atomic-scale description of the dielectric permittivity (both high-frequency and static) and of the infrared absorption at the interface, we introduce two theoretical schemes of general validity.

First, we develop a method for investigating atomic-scale dielectric permittivity profiles across interfaces between insulators. From the microscopic charge density induced by an applied electric field, we calculate a local permittivity which describes variations of the dielectric response over length scales of the order of interatomic distances. In order to establish a relation between the dielectric response and the underlying microscopic structure, the local permittivity is further analysed in terms of maximally localized Wannier functions.

Second, we develop a method for calculating from first principles both the transverse-optical and longitudinal-optical infrared absorption spectra at surfaces and interfaces. We derive expressions for the total absorption spectra of the system under consideration, and then define a spatial decomposition which provides the evolution of the infrared activity across that system. Such a decomposition is particularly suited for associating specific spectral features to the underlying local bonding arrangements.

By using the first method, we determine the profile of the local permittivity across several structural models of the Si-SiO_2 interface. We are able to show that the dielectric transition from the silicon to the oxide occurs within a width of only a few angstroms, and that the interfacial layer carries an enhanced permittivity with respect to bulk vitreous silica. Correspondingly, the equivalent oxide thickness of the interfacial oxide is found to be smaller than the corresponding physical thickness by 0.2–0.3 nm, with beneficial consequences for the scaling of Si-based electronic devices.

By using the second method, we solve a long-standing controversy related to the red shifts of the high-frequency peaks observed in the infrared spectra of ultrathin oxides on silicon with decreasing thickness. By calculating the transverse-optical and the longitudinal-optical absorption spectra across a realistic model of the Si(100)-SiO_2 interface, we are able to assign the microscopic origin of these shifts to the lengthening of the Si-O bonds in the interfacial substoichiometric oxide.

Chapter 1

Introduction

This thesis is devoted to the study of the *infrared properties* of the Si(100)-SiO_2 interface from *first principles*. The term *infrared* is meant to indicate the frequency range encompassing the whole phonon spectrum, and including the high-frequency spectral region just below the electronic transitions. The term *properties* specifically refers to the electronic and static dielectric permittivities and to the infrared absorption spectra. The theoretical investigation presented here is essentially based on *first principles* methods, which aim at describing the behavior of the material considered by directly solving the corresponding quantum-mechanical equations, without resorting to parametrizations based on experimental evidence or physical intuition.

The *atomic-scale* structural, electronic and dielectric properties of the interface between silicon and its oxide have received a great deal of attention in the past decades. Indeed, SiO_2 thermally grown on Si(100) has been hitherto the material of choice for the dielectric which isolates the gate electrode from the Si channel in complementary metal-oxide-semiconductor (CMOS) transistors. The reason for the almost exclusive use of SiO_2 as the gate insulator in CMOS devices resides in the excellent electrical and thermodynamical properties of the interface that it forms with the silicon substrate. Indeed, the growth of SiO_2 on Si(100) gives rise to a low interfacial defect density, a large band gap, and a good dielectric strength. However, the miniaturization of Si-based electronic devices has come to the point where gate dielectrics thinner than 1.5 nm are needed to meet the targeted performance requirements in terms of switching speed and power consumption. Such a small oxide thickness corresponds to a separation between the polycrystalline-Si gate and the Si substrate of only 5 SiO_4 tetrahedra, with at least two of them located at the interfaces with the substrate and the polycrystalline gate. As a consequence, the understanding of the Si(100)-SiO_2 interface at the atomic scale level constitutes today a crucial step for the further improvement of CMOS device performance, as it is witnessed by the growing interest of device manufacturers in first principles modelling of silicon-dielectric interfaces.

In particular, the understanding of the dielectric response of the Si(100)-SiO_2

interface at the atomic-scale carries direct implications on the scalability of integrated CMOS devices. Indeed, an essential requirement for device scaling is a larger gate capacitance density for each new technology generation. To date, the interfacial transition layer between Si and SiO_2 represents a significant fraction of the total gate dielectric thickness. Therefore, a detailed investigation of the dielectric properties of this interfacial layer is of paramount importance for the future scalability of Si-based devices. However, the theoretical treatment of atomic-scale permittivities at interfaces poses severe difficulties in terms of computational cost, and modelling schemes well established for bulk materials are no longer practical when addressing interfaces or surfaces.

One of the most commonly adopted techniques for the characterization of the interface between silicon and its oxide is infrared spectroscopy. This analytical technique probes the vibrational properties of a material and can provide unique insights into the microscopic structure of the interfacial layer, owing to its sensitivity to the details of the atomistic bonding arrangement. Unfortunately, the interpretation of the measured spectra is not straightforward, since the contributions of different structural properties are often difficult to disentangle. The proper interpretation of infrared spectra of ultrathin films must therefore be accompanied by accurate theoretical modelling, as can be provided by first principles methods. However, the calculation of full infrared spectra at the Si(100)-SiO_2 interface has so far not been achieved, because of the theoretical difficulties related to the determination of the infrared intensities and to the treatment of longitudinal optical excitations at interfaces.

The main goal of this thesis consists of providing accurate theoretical modelling of the dielectric permittivity of the interfacial layer at the Si(100)-SiO_2 interface and of the corresponding infrared absorption spectra. This is accomplished by

(i) generalizing the methods for calculating the infrared response of extended systems to the case of interfaces and surfaces, and

(ii) by applying such methods to realistic structural models of the Si(100)-SiO_2 interface.

The techniques developed within this work are of general validity and lay out the basis for the first-principles investigation of the *infrared properties of interfaces and surfaces*.

1.1 Transistor scaling and role of the gate oxide

During the last two decades, the demand for enhanced integrated circuit performance at lower cost has been met by a progressive *scaling* of the physical dimension of the CMOS transistor, leading to a corresponding increase of the device

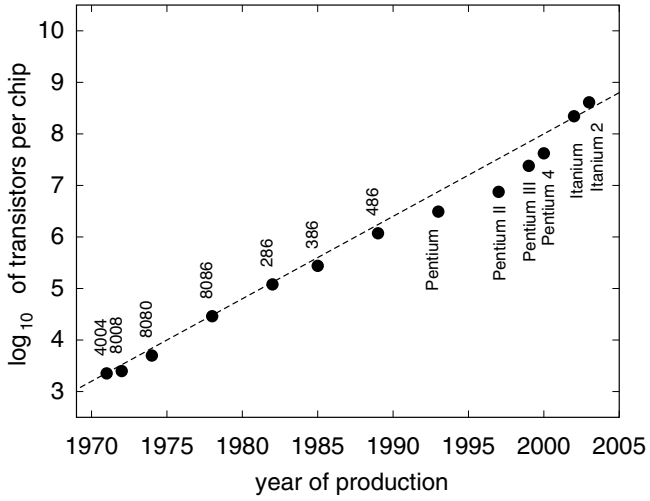

Figure 1.1: The scaling of the CMOS transistor for integrated circuit applications has led to the doubling of the number of transistors per chip every 18-24 months during the past four decades. This semilogarithmic plot shows the number of transistors per chip vs. year of production, for some common commercial processors [1]. The Moore's law is represented by the dashed line.

density on a Si wafer. The rate of increase of transistor density roughly corresponds to a doubling of the number of transistors per chip every 18-24 months (Fig. 1.1). This evolution holds almost unchanged since its first observation four decades ago by G. Moore [2], and is today commonly indicated as "Moore's law". Rather than a mere coincidence between an observation made in the mid sixties and present manufacturers throughput, Moore's law has become a sort of road map for the semiconductor industry. Indeed, after its formulation, an eventual slowdown with respect to the prospected trend was perceived as a threat to the economic expansion of the microelectronic industry. As a consequence, device manufacturers started optimizing their products in order to fall on the Moore's line at each new technology generation (Fig. 1.1). This trend still continues nowadays, but we arrived at a point were the scaling rules so effectively applied to date no longer hold. Indeed, the device dimensions are approaching the nanometer range, and in this regime several phenomena as polysilicon depletion, gate leakage currents, and short-channel effects begin to pose severe difficulties.

Figure 1.2 shows a schematic diagram of the central core of the n-type part of a CMOS transistor. It is comprised of a source and a drain of heavily doped silicon, a thin SiO_2 gate insulator, and a polycrystalline-Si gate electrode. Essentially, a CMOS transistor acts as a switch, allowing charge flow within the Si channel when the gate electrode supplies a sufficient bias voltage through the gate dielectric. The transistor miniaturization consists of reducing its lateral dimensions, namely the channel length (L) and the transistor width (W) (Fig. 1.2). However, such scaling has to be accomplished without reducing the gate capacitance $C = WL\ \varepsilon/t$, ε being the permittivity of the gate oxide and t the corresponding physical thickness. Indeed, the gate capacitance determines the amount of charge that can be induced in the Si channel by an applied gate voltage, and is therefore directly related to the transistor drive current [3]. Hence, in order to reduce the lateral dimensions of the device without lowering the gate

capacitance, it is necessary to simultaneously increase the capacitance density ε/t of the gate dielectric.

To date, the latter requirement has been fulfilled by progressively reducing the thickness t of the gate oxide, typically SiO_2 thermally grown on Si(100) substrates, reaching values as small as 2 nm in present generation devices. However, it has been shown that quantum-mechanical tunneling of electrons and holes from the gate electrode limits the scalability of SiO_2 as a gate oxide to about 13 Å [4, 5]. As a consequence, alternative materials with higher dielectric permittivity (most often transition metal silicates) are under consideration for replacing the natural oxide of silicon and increasing the gate capacitance density ε/t through the permittivity ε [3].

Since for many years the increase of the gate capacitance density has been achieved by reducing the thickness of the SiO_2 layer between the gate electrode and the Si substrate, it is common practice to use the notion of *equivalent oxide thickness* (EOT) of a dielectric as a measure of the gate capacitance density. The equivalent thickness t_{eq} is defined as the theoretical thickness of a SiO_2 layer that would be required to achieve the same capacitance density as the dielectric under consideration: $t_{eq} = (\varepsilon_{SiO_2}/\varepsilon)\ t$. As a reference, the EOT predicted for high-performance applications is required to be as small as 0.8 nm for the technology generation with a channel length of 50 nm, anticipated by the Semiconductor Industry Association for the year 2009 [6].

A common problem encountered in the EOT scaling consists in the formation of an undesired SiO_2 interlayer at the interface between the substrate and high-permittivity oxides [7]. Indeed, during the post-deposition annealing process for the activation of dopants, O atoms diffuse out of the high-permittivity material, and oxidize the Si substrate forming an interfacial oxide layer [8]. Even if potentially beneficial as it provides an intermediate high-quality interface between silicon and the high-permittivity oxide, the contribution of this interlayer to the EOT of the gate stack could be substantial, raising questions about the practi-

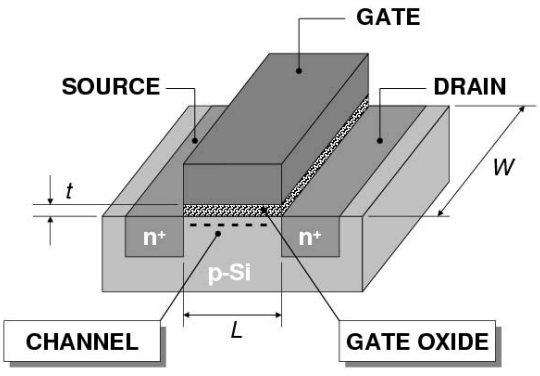

Figure 1.2: Schematic view of a n-MOS transistor. The substrate is p-type Si, while the source and drain contacts are heavily doped n-type Si. At sufficiently high positive gate voltage, the substrate undergoes carrier inversion and a tiny electron channel forms under the gate oxide, leading the device into the conducting state. The transistor width W, the channel length L, and the gate oxide thickness t are indicated.

cal scalability limit of gate dielectrics for CMOS applications [7]. Understanding the structural and the dielectric properties of this interfacial layer is therefore of primary importance for the progress of Si-based microelectronics.

So far, when addressing the permittivity of the gate dielectric, we implicitly referred to the *static* permittivity, corresponding to the dielectric function evaluated at frequencies just below the far infrared region. This is because the operational range of currently available devices is between approximately 100 MHz and 10 GHz. When translated into the frequency units adopted throughout this thesis, the upper bound becomes 30 cm^{-1}, which is well below the main absorption peaks of both bulk SiO_2 and the substoichiometric interfacial layer (cf. Fig. 6.4).

1.2 The Si(100)-SiO_2 interface

It is widely recognized that the outstanding electrical and thermodynamical properties of the interface between the Si channel and the SiO_2 gate oxide have been the key enabler for the scaling of CMOS devices [3]. Therefore, it is not surprising that a huge effort has been devoted to the characterization of this interface at a microscopic level during the past two decades [9].

Several experimental techniques [9] contributed to outline a detailed atomic-scale picture of the Si(100)-SiO_2 interface (Fig. 1.3). First of all, the amorphous nature of the oxide has unambiguously been demonstrated by both transmission electron microscopy and X-ray scattering [10]. X-ray scattering measurements also revealed a disordered bonding pattern at the interface [10, 11]. Despite the disordered reconstruction, the interfacial bonding network is topologically almost perfect, as indicated by the very low density of interface states obtained from electrical measurements and from electron-spin resonance experiments [12, 13].

Photoemission spectroscopy has gathered very detailed informations about the composition of the interfacial layer. In fact, by monitoring the shift of the Si-2p core-levels across the Si(100)-SiO_2 interface, it has been shown that all the intermediate oxidation states of Si, corresponding to Si atoms with one to three O nearest neighbors, occur within the interfacial layer [14, 15, 16, 17, 18]. Furthermore, at a distance of about 1 nm from the Si substrate, the oxide is already stoichiometric, as indicated by ion scattering experiments [10, 19].

Several structural models of the Si(100)-SiO_2 interface have been proposed in the past [17, 18, 20, 21, 22, 23, 24, 25, 26, 27, 28, 29, 30]. However, none of these models matches the full list of atomic-scale properties determined from the available experimental data. An important step towards the atomic-scale modelling of the Si(100)-SiO_2 interface has been made very recently by introducing structural models purposely designed in order to fulfill a variety of constraints set by experiment [31, 32]. Within this thesis, particular emphasis is given to the investigation of the infrared properties at the Si(100)-SiO_2 interface through such *realistic* structural models.

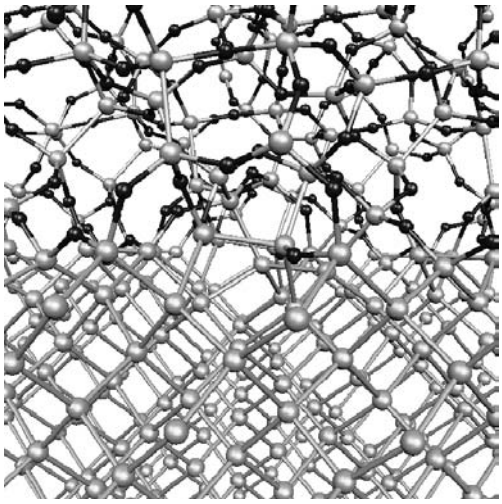

Figure 1.3: Ball-and-stick representation of a model Si(100)-SiO_2 interface. The (001) termination of the Si substrate (bottom, gray balls) exposes two dangling bonds per Si atom, which are saturated either by the O atoms of the oxide (black balls), or by the formation of Si-Si dimers. The region containing partially oxidized Si atoms with their O nearest neighbors, $Si^{+1}O$, $Si^{+2}O_2$, and $Si^{+3}O_3$, constitutes the interfacial layer. This layer shows peculiar electronic, dielectric, and vibrational properties, and affects the electron and hole flow in the Si channel of CMOS devices.

1.3 Dielectric permittivity of ultrathin SiO_2 films on Si(100)

In view of the EOT scaling, the accurate determination of the dielectric permittivity at the Si(100)-SiO_2 interface is of primary importance. However, a thorough understanding of the dielectric effect of the interfacial layer is still missing to date.

Certainly, the use of the permittivity of bulk SiO_2 to take into account the interfacial layer contribution to the EOT is questionable, because of the peculiar structural and electronic properties of that layer. Indeed, electron-energy-loss spectroscopy measurements of the O-K edge profile across the Si(100)-SiO_2 interface indicated a reduced band gap within the interfacial oxide [5], and have been interpreted in terms of silicon states with energies located inside the SiO_2 band gap. Furthermore, it has been speculated that the presence of such states could alter the dielectric screening within the interfacial oxide, possibly leading to an enhanced permittivity [5, 7].

Indirect evidence for an enhanced permittivity within the interfacial oxide has already been reported [33], based on capacitance-voltage measurements on a set of SiO_2-ZrO_2 metal-oxide-semiconductor (MOS) capacitors. The MOS capacitors considered in Ref. [33] included a gate oxide made of a SiO_2 layer of fixed thickness, and ZrO_2 layers of varying thickness. Extrapolation of the measured EOT of the gate dielectric stack to zero ZrO_2 physical thickness, yielded a static dielectric permittivity of the interfacial layer between 6 and 7, appreciably larger than that of bulk SiO_2 ($\varepsilon_{SiO_2} = 3.9$).

Another indication of an interfacial layer with an altered dielectric permittivity has been provided by a recent comparison between the thicknesses of ultrathin

oxides as measured by medium energy ion scattering and by spectroscopic ellipsometry [34]. Indeed, ellipsometric measurements probe the optical path of a light beam, hence the determination of the film thickness relies on *a priori* assumptions about the corresponding dielectric response. In Ref. [34] it was found that, when describing the MOS gate dielectric through the bulk SiO_2 permittivity, the ellipsometric thickness overestimated the physical thickness (as measured by ion scattering) by about 0.2-0.3 nm. The two estimates could be reconciliated only by including an interfacial layer with a permittivity intermediate between those of bulk Si and bulk SiO_2, in line with the discussion above.

As for the extent of the region with an altered dielectric screening, measurements based on Auger spectroscopy suggested that, at a distance of about 6 Å from the substrate, the oxide permittivity recovers the bulk SiO_2 value [35]. However, it must be pointed out that the conclusions drawn in Ref. [35] were based on the observation that the Auger parameter relates to the electrostatic energy associated to the core-hole generated in the photoionization process, which in turn scales with the inverse of the oxide dielectric permittivity. Therefore, the association of the Auger parameter to the oxide permittivity again relies on *a priori* assumptions about the dielectric response of the oxide.

From the above observations it is clear that, while experimental indications of an interfacial layer between Si and SiO_2 with a dielectric permittivity different from that of vitreous silica do indeed exist, they are mainly based on a *classical* interpretation of the measured data. However, in the sub-nanometer regime, the understanding of the dielectric response can no longer be inferred from macroscopic electrostatics, and demands a proper *quantum mechanical* description of the electronic structure [36].

1.4 Infrared absorption of ultrathin SiO_2 films on Si(100)

Infrared spectroscopy has emerged as one of the most successful analytical techniques for investigating surfaces and interfaces [37]. This technique plays nowadays a major role in the experimental characterization of catalytic processes [38], electrode/electrolyte interfaces [39], and thin films for device applications [40].

Since the transverse-optical (TO) peak at 1076 cm^{-1} and the longitudinal-optical (LO) peak at 1256 cm^{-1} in the infrared spectra of SiO_2 arise from the stretching motion of Si-O bonds [41], the corresponding spectral regions carry significant information on the local bonding environment in vitreous silica.

Infrared spectroscopic studies of ultrathin SiO_2 films on Si(100) recorded red shifts of the TO and the LO high-frequency peaks for decreasing oxide thicknesses (Fig. 1.4) [42, 43, 44, 45, 46, 47, 48, 49]. These shifts have variably been ascribed to the compressive strain of the interfacial oxide [45, 46], to void incorporation

[47], or to the presence of substoichiometric silica [42].

In Ref. [45], by studying the TO spectra of thermal oxides on Si(100) with a thickness ranging between 30 and 500 Å, the stretching peak was found to red shift continuously with decreasing thickness, by up to 20 cm^{-1}. Since the interfacial substoichiometric oxide extended up to 10 Å, the effect of substoichiometry on the peak frequency was ruled out, and the authors associated the red shift to the presence of some compressive strain in the oxide. Rather similar conclusions were reached in Ref. [46], after observing a red shift of 50 cm^{-1} with respect to bulk vitreous silica for films with thickness between ∼5 and ∼30 Å.

A different proposal about the origin of the red shifts was put forward in Ref. [47]. Indeed, by comparing the LO and TO spectra measured for a 15 Å thick oxide with simulations based on effective medium theories [50], the authors determined that the softer infrared modes of ultrathin SiO_2 films on Si(100) were due to the incorporation of void in the interfacial layer.

The conclusions drawn in Ref. [42] were also based on effective medium models. In that work, the TO and LO peak frequencies were observed to red shift by up to ∼30 cm^{-1} as the oxide was thinned from ∼30 Å to ∼5 Å. However, by comparing the simulated spectra with experiment, the authors ruled out effects related to the oxide strain and void incorporation, and associated the red shifts to the presence of an interfacial substoichiometric oxide.

A different approach was followed in Ref. [44], where red shifts of ∼40 cm^{-1} were observed for oxides of thickness between 300 and ∼20 Å. In that work, the authors modelled the oxide through a classical SiO_x-SiO_2 stack. By keeping fixed the thickness of the substoichiometric layer SiO_x and by varying the thickness of the pure SiO_2 oxide, the authors showed that a tiny suboxide layer may affect

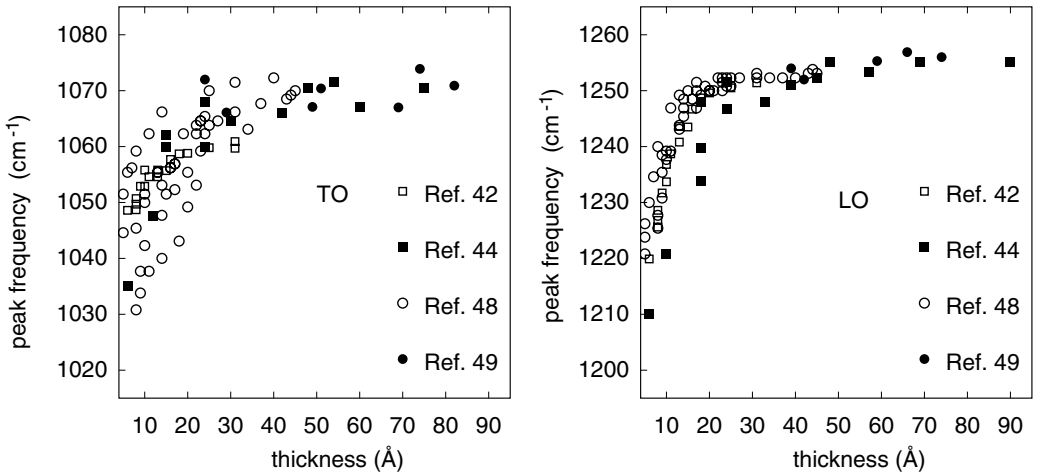

Figure 1.4: Experimentally measured frequency of the Si-O stretching peaks in the TO and LO infrared absorption spectra of SiO_2 films on Si(100) vs. film thickness. The red shift has been alternatively associated to compressive strain, to void incorporation, or to substoichiometry, but its microscopic origin remains unclear.

the infrared spectra of oxides as thick as 100 Å.

From the preceding survey, it emerges that a general consensus on the origin of the TO and LO red shifts of ultrathin oxides on Si(100) has not been reached so far. Now, it must be noted that the different works mentioned above share one common element: they all resort to some *classical* modelling to interpret the measured spectra. However, when applied to ultrathin oxides, classical models such as effective medium theories are questionable and possibly misleading. In this context, the need for a direct comparison with experiment through *first-principles* modelling acquires a primary importance [42].

The understanding of the microscopic origin of the TO and LO red shifts at the Si(100)-SiO_2 interface may also carry direct implications on CMOS integrated circuit manufacturing. Indeed, it has recently been suggested that the frequency of the Si-O stretching peak could effectively be used to distinguish between ordered and disordered Si(100)-SiO_2 interfaces [51]. The advantage of having an ordered interface with an abrupt transition region is substantial. Indeed, such an interface would be accompanied by an enhanced channel mobility due to the reduced scattering by the inhomogeneities of the interfacial layer, leading to larger drive currents and increased transistor performance.

1.5 Outline and organization of the thesis

In order to investigate the dielectric and infrared properties at the Si(100)-SiO_2 interface from first principles, we needed to develop suitable theoretical schemes for addressing heterogeneous systems such as interfaces and surfaces. The theory for the *ab-initio* calculation of the high-frequency (i.e. electronic) and static dielectric permittivities of bulk crystalline systems is well established [52], and the extension to bulk disordered systems has recently been accomplished [53]. However, a general formalism allowing a systematic analysis of layered structures is still missing. A similar consideration applies to the theory for the *ab initio* calculation of infrared spectra: while the formalism for the calculation of phonon dispersions [54] and dipole strengths [52] is well established for bulk crystalline systems, and can be applied to disordered solids as well [55], the generalization to heterogeneous systems such as interfaces and surfaces has not been achieved so far.

In Chap. 2 we present a method for investigating atomic-scale dielectric permittivity profiles at the interface between insulators. The method is based on the observation that the microscopic dielectric function matrix $\varepsilon_{ij}(\mathbf{r}, \mathbf{r}'; \omega)$ is characterized by a spatial nonlocality which typically extends over distances of the order of a bond length. Therefore, by focusing on the latter length scale, the nonlocality does not intervene in the formulation and a local permittivity $\varepsilon_{ij}(\mathbf{r}; \omega)$ can be used to monitor the dielectric properties across an interface. The local permittivity is then decomposed into contributions pertaining to maximally lo-

calized Wannier functions [56], thus establishing a link between variations of the microscopic dielectric response and specific bonding configurations.

In Chap. 3 we introduce a scheme for calculating transverse-optical and longitudinal-optical infrared absorption spectra at surfaces and interfaces. The key idea is to calculate the transverse and longitudinal infrared absorption spectra by adopting a dielectric function which is referred to the *external* electric field rather than to the macroscopic selfconsistent field. This choice allowed us to avoid difficulties related to the inversion of the dielectric function required for the longitudinal spectrum. In addition, we describe a spatial decomposition of the infrared absorption functions which is useful for following the evolution of the infrared activity across interfaces and surfaces. The definition of this spatial decomposition follows the spirit of Chap. 2 and is based on the determination of the lattice dielectric response of atomically thin layers.

Chapter 4 reviews the structural models of the Si(100)-SiO_2 adopted in this work. We describe the procedures followed for generating the models, and the corresponding structural and the electronic properties. We start from simple models in which the interface is obtained by matching a crystalline phase of SiO_2 to Si(100), and then we consider more realistic interface models featuring disordered interfacial layers and amorphous oxides.

In Chap. 5 we present the calculated dielectric permittivity profile across the Si(100)-SiO_2 interface, as obtained by applying the scheme introduced in Chap. 2 to the interface models of Chap. 4. We show that the dielectric transition from the Si substrate to the SiO_2 oxide occurs within a width of only a few angstroms, corresponding to the extent of the interfacial suboxide layer. The polarizabilities associated to partially oxidized Si atoms together with their nearest neighbor O atoms are found to be enhanced with respect to bulk SiO_2, leading to an enhanced permittivity within the interfacial layer, in agreement with experiment.

Chapter 6 is devoted to the study of the transverse-optical and longitudinal-optical infrared absorption spectra at the Si(100)-SiO_2 interface. We applied the formalism developed in Chap. 3 to one of the realistic interface models described in Chap. 4. The calculated infrared absorption spectra are shown to compare well with experiment on bulk SiO_2 and to reproduce the red shifts of the stretching peaks with decreasing oxide thickness. We further show that the stretching frequency decreases with increasing Si-O bond length. As a consequence, the longer Si-O bond lengths observed within the interfacial oxide result in softer stretching modes as compared to bulk SiO_2. This effect is shown to be at the origin of the measured red shifts of the TO and LO high-frequency peaks of ultrathin oxide films on Si(100).

Finally, Chap. 7 summarizes the main results of this thesis. It is worth mentioning that, among the others, Appendix F deserves consideration since it reports about our first steps towards the *ab initio* investigation of $Zr_xSi_{1-x}O_2$ gate oxides, which are nowadays considered as possible replacements of SiO_2 in future CMOS

devices. By modelling Si $2p$ core-level shifts at Si(100)-$Zr_xSi_{1-x}O_2$ interfaces, we found that the Si $2p$ line shifts to lower binding energies with increasing Zr content, in agreement with experiment.

Chapter 2

Theory of dielectric permittivity at surfaces and interfaces

In this chapter, we develop a scheme for investigating atomic-scale dielectric permittivity profiles across interfaces between insulators. A local permittivity $\varepsilon(x;\omega)$ is introduced to describe variations of the dielectric response over length scales of the order of interatomic distances (Sec. 2.1.1). The nonlocality of the microscopic permittivity tensor $\varepsilon_{ij}(\mathbf{r},\mathbf{r}';\omega)$ occurs on smaller distances and therefore does not intervene in our formulation.

We show that the permittivity can conveniently be analysed in terms of maximally localized Wannier functions (Sec. 2.1.2). In this way, we can relate variations of the microscopic dielectric response to specific features of the local bonding arrangement. In addition to a continuous description in terms of the local permittivity, we introduce an alternative scheme based on discrete polarizabilities (Sec. 2.1.3). In the latter case, electronic polarizabilities $\alpha^{(n)}_{\text{elec}}$ are obtained in terms of the displacements of maximally localized Wannier functions, while ionic polarizabilities $\alpha^{(I)}_{\text{ion}}$ are determined from the induced ionic displacements and the corresponding dynamical charges.

The scheme is then illustrated through applications to bulk Si with a defective layer (Sec. 2.3.1) and to Si slabs of finite thickness (Sec. 2.3.2). In the latter case, we investigate the origin of the size-dependent permittivity (Sec. 2.3.2) by addressing the local permittivity profile across silicon slabs of finite thickness. Our analysis indicates that the variation of the permittivity relates to the reduced screening of the outermost Si planes. This effect becomes progressively more important as the surface-to-volume ratio increases, and explains the reduction of the average slab permittivity with decreasing thickness.

2.1 Theory of the local permittivity

2.1.1 Permittivity profile

We are going to introduce a procedure for calculating the dielectric permittivity profile of an insulating material along a given direction. Our approach is based on the definition of a *microscopic* polarization through the transient current induced by an electric field [57]. This approach carries the advantage that the polarization field is well-defined down to atomistic length scales and does not suffer from any gauge arbitrariness [58].

In the linear regime and in stationary conditions, an applied microscopic electric field $e_i(\mathbf{r};\omega)$ induces a microscopic polarization $p_i(\mathbf{r};\omega)$ given by

$$p_i(\mathbf{r};\omega) = \int d\mathbf{r}' \chi_{ij}(\mathbf{r},\mathbf{r}';\omega) e_j(\mathbf{r}';\omega), \tag{2.1}$$

where $\chi_{ij}(\mathbf{r},\mathbf{r}';\omega)$ denotes the microscopic dielectric susceptibility tensor, ω corresponds to the frequency of the applied field, and the indices indicate Cartesian directions. In Eq. (2.1), the electric field $e_i(\mathbf{r};\omega)$ includes the selfconsistent response of the system to the external applied field. The frequency ω appearing in Eq. (2.1) is here assumed to be smaller than typical electronic excitation energies.

We are interested in defining a dielectric permittivity which varies in the x direction on length scales corresponding to interatomic distances. For this purpose, we smooth atomic scale fluctuations of the charge density in the x direction by a convolution with a Gaussian kernel. The width of this kernel then defines the typical length scale over which variations of the permittivity are meaningful. In the orthogonal directions, we consider macroscopic planar averages. Under these conditions, the dielectric susceptibility takes the form:

$$\chi_{ij}(\mathbf{r},\mathbf{r}';\omega) \simeq \chi_i(x;\omega)\delta(\mathbf{r}-\mathbf{r}')\delta_{ij}, \tag{2.2}$$

where the off-diagonal components vanish because of the planar average.

In Eq. (2.2), we assume in addition that the dielectric response is local. This assumption of locality is well justified when averages over interatomic distances are considered. Indeed, for insulators, the homogeneous real-space dielectric function generally decays with a characteristic length of the order of interatomic distances. For instance, we estimated decay lengths of 0.7 Å for SiO_2 and of 1.7 Å for Si (cf. Appendix A).

Combining Eqs. (2.1) and (2.2), we obtain

$$\overline{\overline{p}}_x(x;\omega) = \chi(x;\omega)\overline{\overline{e}}_x(x;\omega), \tag{2.3}$$

where the double bars indicate the average over the yz plane and the Gaussian filter. In Eq. (2.3), we dropped the Cartesian index of the dielectric susceptibility

specifying the x direction. In the following, we will refer to $\chi(x;\omega)$ as to the *local* susceptibility, and to

$$\varepsilon(x;\omega) \equiv 1 + 4\pi\chi(x;\omega) \tag{2.4}$$

as to the corresponding *local* permittivity.

In Eq. (2.3), the electric field $\overline{\overline{e}}_x(x;\omega)$ is obtained from the induced charge density $\rho_{\rm ind}$ through the Gauss relation:

$$\frac{d}{dx}\overline{\overline{e}}_x(x;\omega) = 4\pi\overline{\overline{\rho}}_{\rm ind}(x;\omega). \tag{2.5}$$

The induced polarization $\overline{\overline{p}}_x(x;\omega)$ is defined through the transient current induced by an electric field [57]. However, in the case of one-dimensional systems, this polarization can be obtained following an alternative procedure. In general, the equation,

$$\nabla \cdot \mathbf{p}(\mathbf{r};\omega) = -\rho_{\rm ind}(\mathbf{r};\omega), \tag{2.6}$$

specifies the polarization within a divergence-free vector field. For one-dimensional systems, the planar average of the latter field vanishes and the polarization $\overline{\overline{p}}_x$ satisfies the relation

$$\frac{d}{dx}\overline{\overline{p}}_x(x;\omega) = -\overline{\overline{\rho}}_{\rm ind}(x;\omega). \tag{2.7}$$

Equations (2.5) and (2.7) give the electric field $\overline{\overline{e}}_x$ and the polarization $\overline{\overline{p}}_x$, respectively, up to two additive constants. For a finite system, the first constant is fixed by the requirement that the electric field away from the system equals the external field, while the second constant is fixed by the condition that the induced polarization vanishes in the region with vanishing charge density. At variance, when an extended periodic model is adopted, the unknown constant in $\overline{\overline{e}}_x$ is determined by the average selfconsistent electric field in the supercell, while the corresponding term in $\overline{\overline{p}}_x$ is determined by the macroscopic Berry-phase polarization.

When the calculation is performed within a supercell, it is convenient to express the local susceptibility in terms of the polarization $\overline{\overline{p}}_x$. From Eqs. (2.3), (2.5), and (2.7), we obtain:

$$\frac{4\pi\chi(x;\omega)}{1+4\pi\chi(x;\omega)} = \Big(1 - \frac{1}{\varepsilon(\omega)}\Big)\frac{\overline{\overline{p}}_x(x;\omega)}{\langle\overline{\overline{p}}_x(x;\omega)\rangle}, \tag{2.8}$$

where the brackets $\langle\cdots\rangle$ indicate an average over the simulation cell, and $\varepsilon(\omega)$ corresponds to the permittivity of the full cell:

$$\varepsilon(\omega) \equiv 1 + 4\pi\frac{\langle\overline{\overline{p}}_x(x;\omega)\rangle}{\langle\overline{\overline{e}}_x(x;\omega)\rangle}. \tag{2.9}$$

We note that Eqs. (2.4), (2.7) and (2.8) establish a direct link between the induced charge density and the local permittivity regardless of the frequency ω. Thus, the derived relations hold in particular for the electronic $\varepsilon^{\infty}(x)$ and the static $\varepsilon^{0}(x)$ permittivities.

In practical applications, it is often convenient to define a permittivity pertaining to a slab of finite thickness, delimited by the planes $x = x_1$ and $x = x_2$. From Eqs. (2.3), (2.4), (2.5) and (2.7), one derives:

$$\frac{\partial}{\partial x}\left[\varepsilon(x,\omega)\cdot\overline{\overline{e}}_x(x,\omega)\right] = 0, \tag{2.10}$$

which is analogous to the conservation of the component of the displacement field orthogonal to the interfaces in classical electrostatics. This analogy is also at the basis of the following relation which holds between the permittivity of the slab $\varepsilon([x_1,x_2];\omega)$ and the local permittivity $\varepsilon(x,\omega)$:

$$\frac{1}{\varepsilon([x_1,x_2];\omega)} = \frac{1}{x_2-x_1}\int_{x_1}^{x_2}\frac{1}{\varepsilon(x,\omega)}dx. \tag{2.11}$$

2.1.2 Wannier decomposition of the permittivity profile

To analyze the dielectric properties at the atomic scale, we describe the electronic structure in terms of localized Wannier functions [56]. A given decomposition in Wannier functions directly defines a partition of the electronic charge density in localized contributions. We here restrict the discussion to a single-particle description. While we refer to the Wannier terminology pertaining to extended periodic systems, the same concepts apply in a fully equivalent way to finite systems.

For an insulator in an electric field $\mathcal{E}$, the material state of interest corresponds to a long-living excited state [59], for which the density matrix preserves the periodicity of the ground state and its insulator-like properties [60, 61]. Hence, for this state, it remains possible to define a set of localized Wannier functions $\{w_n^{\mathcal{E}}\}$ [62]. By continuity, an unambiguous one-to-one correspondence can be established between these polarized Wannier functions and the respective ones in absence of electric field $\{w_n^{\mathcal{E}=0}\}$. This correspondence defines a partition of the induced charge density in localized contributions $\rho_{\mathrm{ind}}^{(n)} = |w_n^{\mathcal{E}}|^2 - |w_n^{\mathcal{E}=0}|^2$:

$$\overline{\overline{\rho}}_{\mathrm{ind}} = \sum_n \overline{\overline{\rho}}_{\mathrm{ind}}^{(n)}, \tag{2.12}$$

where the double bars correspond to the double averages defined in Sec. 2.1.1. The localized contributions to the dipole density $\overline{\overline{p}}_x^{(n)}(x;\omega)$ are then defined through the analogous of Eq. (2.7):

$$\frac{d}{dx}\overline{\overline{p}}_x^{(n)}(x;\omega) = -\overline{\overline{\rho}}_{\mathrm{ind}}^{(n)}(x;\omega). \tag{2.13}$$

When integrating Eq. (2.13), we fix the unknown constant through the condition:

$$A\int_{-\infty}^{\infty}\overline{\overline{p}}_x^{(n)}(x;\omega)dx \equiv e(x_n^{\mathcal{E}} - x_n^{\mathcal{E}=0}), \tag{2.14}$$

where A corresponds to the transverse area of the simulation cell, e is the electron charge, and $x_n^{\mathcal{E}}$ stands for the center of the Wannier function $w_n^{\mathcal{E}}$. This choice ensures that the sum of the individual contributions gives the full induced polarization:

$$\begin{aligned} A\int_0^{L_x}\overline{\overline{p}}_x(x;\omega)dx &\equiv A\int_0^{L_x}\sum_n\overline{\overline{p}}_x^{(n)}(x;\omega)dx \\ &= \sum_n e(x_n^{\mathcal{E}} - x_n^{\mathcal{E}=0}) = \Omega(P_x^{\mathcal{E}} - P_x^{\mathcal{E}=0}), \end{aligned} \tag{2.15}$$

where Ω is the volume of the simulation cell. In Eq. (2.15), the integral extends over a periodic cell and the sum over the corresponding Wannier functions. The assignment in Eq. (2.14) is therefore consistent with the way we determined the constant when integrating Eq. (2.7). The last equality in Eq. (2.15) results from the very basic definition of the Berry-phase polarization (denoted by P_x) [63].

To evaluate the contribution to the local susceptibility $\chi^{(n)}(x;\omega)$ resulting from each Wannier function, we proceed along the same lines as in Sec. 2.1.1:

$$\overline{\overline{p}}_x^{(n)}(x;\omega) = \chi^{(n)}(x;\omega)\overline{\overline{e}}_x(x;\omega). \tag{2.16}$$

Repeating the derivation which led to Eq. (2.8), we obtain:

$$\frac{4\pi\chi^{(n)}(x;\omega)}{1+4\pi\chi(x;\omega)} = \big(1-\frac{1}{\varepsilon(\omega)}\big)\frac{\overline{\overline{p}}_x^{(n)}(x;\omega)}{\langle\overline{\overline{p}}_x(x;\omega)\rangle}, \tag{2.17}$$

which relates the dipole density associated to a Wannier function to the corresponding local susceptibility. From Eqs. (2.8) and (2.17), it follows that

$$\varepsilon(x;\omega) = 1 + \sum_n 4\pi\chi^{(n)}(x;\omega). \tag{2.18}$$

For one-dimensional systems, it is convenient to use Wannier functions *maximally* localized along the x direction, the so-called hermaphrodite Wannier functions [64]. Since the typical localization length of such functions is of the order of bond lengths [64], the resulting decomposition of the local susceptibility $\chi(x;\omega)$ turns out to be particularly suitable for assigning variations of the local susceptibility to specific structural features, as we demonstrate in the following sections. Furthermore, hermaphrodite Wannier functions carry a special significance, since they are eigenstates of the one-dimensional position operator in extended systems [64].

2.1.3 Decomposition in discrete polarizabilities

An alternative way to investigate the variation of the local permittivity consists in decomposing the continuous dielectric medium in discrete units. In this section, we consider separately the electronic and ionic responses to the electric field.

Electronic polarizabilities

Using the decomposition introduced in Sec. 2.1.2, we define an *effective* electronic polarizability $\alpha_{\text{elec}}^{(n)}$ for each Wannier function by relating its induced dipole to the electric field at its center x_n:

$$e(x_n^{\mathcal{E}} - x_n^{\mathcal{E}=0}) \equiv \alpha_{\text{elec}}^{(n)} \overline{\overline{e}}_x(x_n), \tag{2.19}$$

where the same approximations leading to Eq. (2.3) are assumed. To make connection with Sec. 2.1.2, we point out that there is a simple relationship between the effective polarizabilities $\alpha_{\text{elec}}^{(n)}$ and the contribution to the local susceptibility of a given Wannier function $\chi^{(n)}(x)$. Using Eqs. (2.14) and (2.16), one derives:

$$\alpha_{\text{elec}}^{(n)} = \frac{A}{\overline{\overline{e}}_x(x_n)} \int_0^{L_x} \chi^{(n)}(x) \overline{\overline{e}}_x(x) dx. \tag{2.20}$$

Using the last equality in Eq. (2.15), we then recover the electronic permittivity of the full simulation cell as follows:

$$\varepsilon_\infty = 1 + \frac{4\pi}{\Omega} \sum_n \frac{\overline{\overline{e}}_x(x_n)}{\langle \overline{\overline{e}}_x(x) \rangle} \alpha_{\text{elec}}^{(n)}. \tag{2.21}$$

In particular, when the effective field is slowly varying, as for instance well inside homogeneous regions, Eq. (2.20) simplifies to

$$\alpha_{\text{elec}}^{(n)} = A \int_0^{L_x} \chi^{(n)}(x) dx, \tag{2.22}$$

establishing a transparent relation with the local susceptibility of the Wannier function $\chi^{(n)}(x)$. Similarly, Eq. (2.21) reduces to

$$\varepsilon_\infty = 1 + \frac{4\pi}{\Omega} \sum_n \alpha_{\text{elec}}^{(n)}. \tag{2.23}$$

Ionic polarizabilities

With the same spirit as for the electronic polarizabilities, we define effective ionic polarizabilities through the induced dipole associated to a given ion. The latter can be expressed in terms of the induced ionic displacement and the corresponding dynamical charge.

In nonhomogeneous systems such as superlattices, the local electric field might present significant spatial variations. In order to define truely local quantities, we introduce in this work dynamical charges ζ_I which are defined with respect to the effective local field $\overline{\overline{e}}_x$ rather than to the macroscopic field:

$$\zeta_{I,x\alpha} \equiv \frac{\partial F_{I,\alpha}}{\partial \overline{\overline{e}}_x(R_{Ix})}, \tag{2.24}$$

where $F_{I\alpha}$ and $R_{I\alpha}$ indicate the ionic force and coordinate along the x axis, respectively. The dynamical charges ζ_I are related to the Born (Z_I^{B}) and Callen (Z_I^{C}) charges [65] through:

$$\zeta_{I,x\alpha} = \frac{\varepsilon^\infty(x)}{\varepsilon^\infty} Z^{\mathrm{B}}_{I,x\alpha} = \varepsilon^\infty(x) Z^{\mathrm{C}}_{I,x\alpha}, \tag{2.25}$$

where $\varepsilon^\infty(x)$ corresponds to the local electronic permittivity introduced in Sec. 2.1.1 and ε^∞ is the electronic permittivity of the simulation cell. In the homogeneous regions on both sides of a heterojunction, the charges ζ_I defined by Eq. (2.24) reduce to the Born charges of the corresponding bulk materials.

In analogy with the electronic polarizabilities in Eq. (2.19), we then define an effective ionic polarizability as

$$\sum_\alpha \zeta_{I,x\alpha}(R^{\mathcal{E}}_{I\alpha} - R^{\mathcal{E}=0}_{I\alpha}) \equiv \alpha^{(I)}_{\mathrm{ion}} \overline{\overline{e}}_x(R_{Ix}). \tag{2.26}$$

From the ionic contribution to the induced macroscopic polarization along x [66],

$$P^{\mathrm{ion}}_{x,\mathcal{E}} - P^{\mathrm{ion}}_{x,\mathcal{E}=0} = \frac{1}{\Omega} \sum_{I,\alpha} Z^{(B)}_{I,x\alpha}(R^{\mathcal{E}}_{I\alpha} - R^{\mathcal{E}=0}_{I\alpha}), \tag{2.27}$$

the lattice contribution to the static permittivity is obtained as

$$\varepsilon_0 - \varepsilon_\infty = 4\pi \frac{P^{\mathrm{ion}}_{x,\mathcal{E}} - P^{\mathrm{ion}}_{x,\mathcal{E}=0}}{\langle \overline{\overline{e}}_x(x) \rangle}. \tag{2.28}$$

From Eqs. (2.25)–(2.28), we then derive the explicit relation between the effective ionic polarizabilities and the permittivity of the full simulation cell:

$$\varepsilon_0 - \varepsilon_\infty = \frac{4\pi}{\Omega} \sum_I \frac{\varepsilon^\infty}{\varepsilon^\infty(R_{Ix})} \frac{\overline{\overline{e}}_x(R_{Ix})}{\langle \overline{\overline{e}}_x(x) \rangle} \alpha^{(I)}_{\mathrm{ion}}. \tag{2.29}$$

When the effective field and the electronic permittivity vary slowly, as for instance inside homogeneous regions, Eq. (2.29) simplifies to

$$\varepsilon_0 - \varepsilon_\infty = \frac{4\pi}{\Omega} \sum_I \alpha^{(I)}_{\mathrm{ion}}. \tag{2.30}$$

In this section, we provided a description of the variation of the local permittivity along a given direction. After taking averages in the orthogonal planes, we critically relied on Eq. (2.6) for deriving the microscopic polarization from the induced charge density in a gauge-invariant way. The definition of a local dielectric permittivity varying in three dimensions constitutes a desirable extension of the present scheme. However, in this case, Eq. (2.6) alone is no longer sufficient for determining the microscopic polarization, which remains undetermined by a divergence-free component. While the induced local polarization can in principle be calculated through the transient induced current [58], the computational effort becomes significantly more demanding.

Nonetheless, it should be noted that a truely three-dimensional description remains easily accessible through the effective polarizabilities defined in Sec. 2.1.3. Indeed, these polarizabilities are well defined also in the three-dimensional case through the sole knowledge of the induced dipoles and the effective electric field, without requiring the microscopic polarization. A description in terms of such polarizabilities can be highly effective in identifying the dielectric response of specific structural units.

2.2 Practical implementation

2.2.1 General methods

The calculations described in the present chapter and in Chap. 5 were performed adopting a generalized gradient approximation to density functional theory [67]. We accounted for valence electronic states using a pseudopotential scheme [68, 69]. We adopted a normconserving pseudopotential for Si atoms [70] and ultrasoft ones for O and H atoms [71]. The wave functions and the charge density were expanded in plane-wave basis sets with kinetic energy cutoffs of 24 and 150 Ry, respectively. The Brillouin zone of the investigated systems were sampled at the Γ point. Structural relaxations were performed within a damped molecular dynamics approach [72], and carried on until the ionic forces were smaller than 0.005 eV/Å.

We calculated the static and high-frequency dielectric permittivities through the application of a finite electric field, as described in Ref. [53] within the context of the Berry-phase theory of the polarization [63, 73, 74], unless specified otherwise. The induced charge density appearing in Eqs. (2.5)-(2.7) was evaluated by calculating the difference between the charge densities corresponding to two opposite macroscopic electric fields. The local dielectric permittivity was then derived as described in Sec. 2.1.1. We note that, in the case of finite systems (cf. Sec. 2.3.2), the local dielectric response can also be obtained through the application of a simple saw-tooth potential.

The smoothing required to remove nonlocality effects was performed by means

of a Gaussian kernel with a standard deviation of 1 Å. With this kernel, the smoothed polarization and electric fields vary by less than 1% well inside the bulk components (cf. Appendix B).

To obtain Wannier functions maximally localized along the x direction, we made use of the algorithm described in Ref. [75]. This procedure consists in determining the unitary transformation which minimizes the off-diagonal matrix elements of the position operator [76] (cf. Appendix D). We note that, at the Γ point, the position operator is nonhermitian [64]. Therefore, the optimal unitary transformation does not diagonalize this operator exactly [64], and the centers $\{x_n\}$ of the resulting Wannier functions,

$$x_n \equiv \frac{L_x}{2\pi}\mathrm{Im}\,\ln\langle w_n|e^{i2\pi x/L_x}|w_n\rangle, \tag{2.31}$$

only approximately correspond to the eigenvalues of the position operator. This difference affects the last equality in Eq. (2.15). However, this effect vanishes in the limit of large supercell size [64]. Indeed, we found that such differences amount to at most 1% for the large supercells in our calculations.

2.2.2 Bulk permittivities: convergence issues

We determine the permittivity using a finite-field approach with a Γ-point sampling, by taking finite differences of the polarization with respect to the electric field [53]. Therefore, it is important (i) to determine the range of electric fields in which the polarization scales linearly, and (ii) to study the scaling of the permittivity with the size L_x of the simulation cell.

To determine the range of electric fields in which the polarization scales linearly we proceeded as follows. In view of the systems considered, we focused on bulk Si. We calculated the susceptibility of a bulk Si sample as a function of the electric field $\mathcal{E}_x$. We considered a simulation cell of size $L_x = 21.94$ Å in the [100] direction (16 MLs), with a transverse 2×2 repeat unit. Figure 2.1 shows that the dielectric response is almost linear up to a field of 0.001 a.u. Beyond this value, the permittivity progressively increases until the electric field value of 0.01 a.u., beyond which the electronic structure could no longer be converged [53]. Since the numerical convergence is faster for larger fields, we chose to work with an optimal value for the electric field given by $\mathcal{E}_x \cdot L_x = 0.001 \cdot 21.94$ a.u. $\cdot$ Å.

The study of the permittivity as a function of the simulation cell size relates to the choice of sampling the Brillouin zone of the simulation cell with the sole Γ point, and therefore corresponds to the study of the k-point convergence [77]. For this purpose, we calculated the permittivity of bulk Si using simulation cells with the same transverse size as above but with varying L_x (Fig. 2.1). For large cell parameters ($L_x > 20$ Å), we found a L_x^{-2} behavior [77] (cf. Appendix D), and we extrapolated the trend to obtain a converged value of $\varepsilon_{\mathrm{Si}} = 14.3$. Given the limited yz sampling of the Brillouin zone in the present calculation, this converged

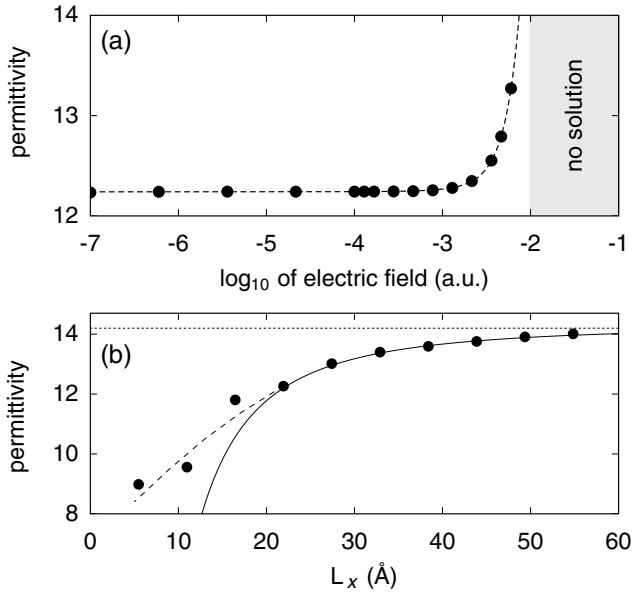

Figure 2.1: (a) Permittivity of bulk Si as a function of the electric field (disks). The region where the electronic structure could not be converged is shaded. (b) Permittivity of bulk Si as a function of the size of the simulation cell L_x (disks). The solid line corresponds to the L_x^{-2} limiting behavior. The dotted line indicates the value extrapolated for an extended system. Dashed lines in (a) and (b) are guides to the eye.

value differs from that determined with a full k-point sampling, overestimating the latter by 13% [78].

At this stage, it is worth noting that the convergence with k-point sampling of the local permittivity of a layered system is more demanding than the convergence of the corresponding overall permittivity. Indeed, while the induced charge density appearing in Eq. (2.7) rapidly converges with the Brillouin zone sampling, the Berry-phase polarization which enters $\overline{\overline{p}}_x$ through the additive constant does not. As a result, when the macroscopic polarization is converged within an error δ, the corresponding error on the local permittivity is $\sim \varepsilon(x)\delta$.

2.3 Local permittivity in silicon slabs

2.3.1 Bulk Si with a defect layer

To illustrate our procedure for determining the local dielectric permittivity, we focus in this section on a model system with a localized defect layer. We first considered a bulk Si system with a supercell containing 16 ML in the [100] direction and a 2×2 repeat unit in the orthogonal plane. Using a finite electric field [53], we calculated a permittivity of 12.3 for this system. Next, we introduced the following perturbation: we increased the supercell size L_x in the [100] direction while maintaining all the (100) interplane separations but one at the equilibrium distance. In the resulting structure, all Si-Si bond distances are at equilibrium (2.37 Å) except those corresponding to the larger interplane separation (2.63 Å). Furthermore, the latter bonds are slightly tilted towards the [100] direction. In Fig. 2.2, we show the local susceptibility profile as a function of a coordinate

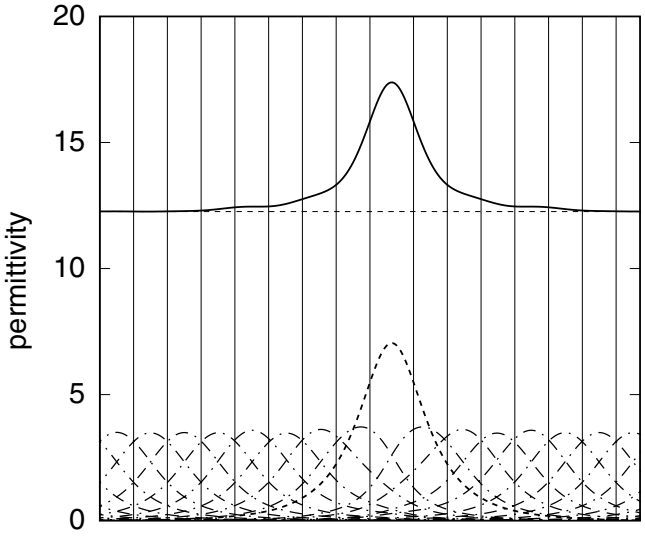

Figure 2.2: Permittivity profile (solid) along the [100] direction of bulk Si, showing a defective layer with a larger interplanar separation. The horizontal dashed line indicates the permittivity of the regular structure. The Wannier contributions to the local permittivity arising from the defective (dotted) and the regular (dash-dotted) Si layers are also shown. Vertical lines represent planes of Si atoms.

along the [100] direction.

An enhancement of the local susceptibility is observed in correspondence of the stretched layer. At a distance of about two monolayers from the defect, the bulk Si value is essentially recovered. To understand this behavior, we decomposed the local susceptibility in localized contributions pertaining to maximally localized Wannier functions of individual layers (Fig. 2.2). It is evident that all the regular Si-Si bonds give very similar contributions, irrespective of their location with respect to the defective bonds. In particular, these regular contributions are fully consistent with the susceptibility of the undefected system. On the other hand, the defective layer shows a much larger susceptibility, which is responsible for the observed enhancement of the local screening.

2.3.2 Silicon slabs

In this section, we study the effect of the finite size on the high-frequency dielectric permittivity of Si quantum wells by performing the local analysis described in Sec. 2.1.1. The quantum confinement of the electrons in a system of finite size induces a blue shift of the optical absorption spectrum [79, 80]. Since the absorption spectrum is directly related to the real part of the dielectric function through the Kramers-Krönig relations, it has been suggested that the confinement should affect the dielectric permittivity [81]. The decrease of the electronic permittivity with size has already been predicted for various silicon nanostructures [82, 83]. However, methods based on macroscopic approaches are not able to establish whether the size-dependence of the permittivity arises from a quantum confinement effect, or from the increased surface-to-volume ratio in small nanostructures [82, 83]. Recent work supports that quantum confinement has a negligible effect,

the permittivity reduction being essentially due to the lower polarizability at the surfaces [84].

Here, we considered Si slabs with (100) surfaces. We used a periodic repeat unit of 2×2 in the planes parallel to the surfaces. The slabs were terminated by H atoms, with Si-H bond lengths as in silane (1.5 Å) and H-Si-H angles at the tetrahedral value. To investigate the size-dependence of the slab permittivity, we calculated the local permittivity profiles for Si slabs with thicknesses ranging between 0.5 and 4 nm, corresponding to 3 and 29 MLs, respectively. We included a finite electric field in our calculation through a saw-tooth shaped potential, and we fixed the unknown constant in Eq. (2.7) by requiring that the microscopic polarization vanishes in the middle of the vacuum region of the simulation cell. This approach allowed us to avoid the convergence issues related to the Berry-phase polarization. Figure 2.3 shows that, beyond a critical size of 13 MLs, the permittivity profile in the slab interior is flat and closely matches (within 1%) the bulk value of $\varepsilon_{\mathrm{B}} = 14.3$ determined in Sec. 2.2.2, while the local permittivity in the outermost Si planes decreases as the surface is approached.

For slabs with less than 13 MLs, the permittivity of the inner layers is appreciably smaller than the bulk Si value, and decreases with decreasing thickness. Within this range, a detailed analysis of the Wannier function contributions to the local permittivity reveals that the Si–H bonds at the surface and the Si–Si bonds between the two outermost Si planes exhibit a reduced polarizability if compared to bulk Si–Si bonds. As a result, when the slab is thinner than 13 MLs, the proximity of the surfaces prevents the inner layers from reaching the bulk value. Overall, the combined effect of an inner region with the permittivity of bulk Si and of two outer regions with lower permittivities results into an average value which approaches the bulk permittivity rather slowly with increasing

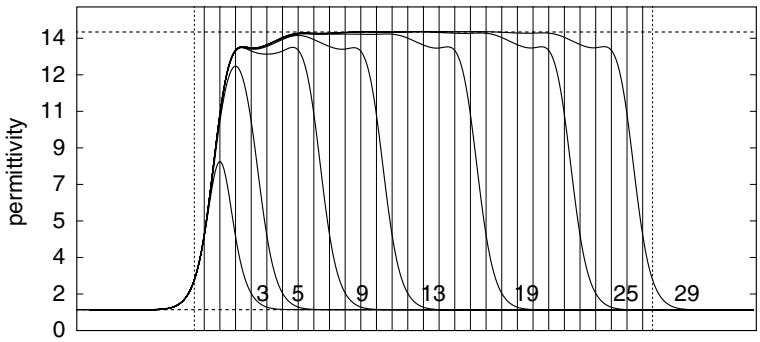

Figure 2.3: Permittivity profiles along the [100] direction for Si(100) slabs with H-terminated surfaces. The numbering refers to the slab size in terms of Si planes. Vertical lines represent planes of Si (solid) and H (dotted) atoms for the largest considered slab. All the slabs are aligned through the positions of the H atoms of the surface on the left. The permittivities of the extended bulk (14.3) and of the vacuum are indicated by horizontal lines.

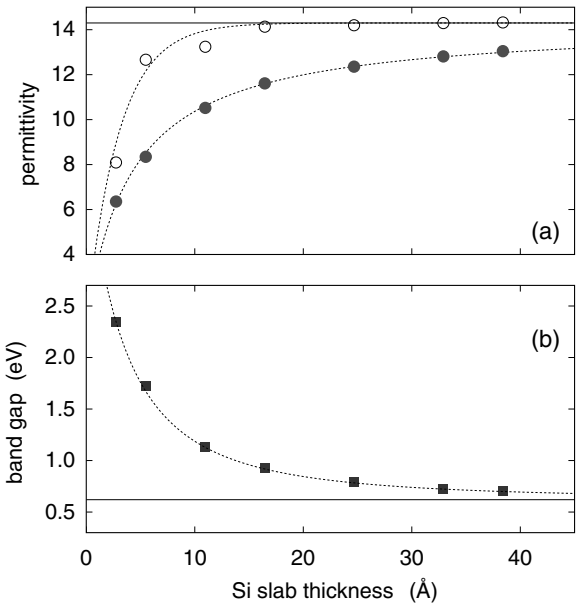

Figure 2.4: (a) Permittivity of a Si slab as a function of thickness d: local permittivity in the central Si plane (circles) compared to the overall slab permittivity (disks). The horizontal line indicates the permittivity of a slab of infinite thickness (14.3), as determined in Sec. 2.2.2. The dashed lines are guides to the eye. (b) Band gap of a Si slab as a function of thickness d (squares). The horizontal line indicates the band gap of a slab of infinite thickness (0.62 eV). The dashed line is a guide to the eye.

thickness. This is shown in Fig. 2.4, where we compare the local permittivity in the central Si plane with the average permittivity over the slab. To evaluate the average permittivity, we used Eq. (2.11) with the slab boundaries taken at the outermost Si planes. This choice sets the slab thickness d equal to the distance between the farmost Si layers.

In Fig. 2.4 we also report for comparison the band gaps of the considered Si slabs. The dependence of the Si band gap on slab thickness approximately follows the d^{-2} behavior expected for an infinite potential well, and agrees with previous calculations within 0.1 eV [85]. While the relative band gap reduction from the slab with 13 Si MLs to the one with 31 MLs is $\sim$30%, the corresponding increase in the permittivity of the inner layers is $\sim$1%, indicating that the band gap and the permittivity are not correlated. This finding can be rationalized by considering that the permittivity depends on the whole absorption spectrum and not only on the band gap energy.

To summarize our results on hydrogen-terminated Si(100) slabs, quantum confinement is found to have a negligible effect on the permittivity, at least beyond a critical thickness corresponding to 13 Si MLs. Furthermore, the reduction of the average slab permittivity with decreasing thickness originates from the increasing surface-to-volume ratio. Despite the rather different methodological approaches, our results are in good overall agreement with the calculations of Ref. [84].

Chapter 3

Theory of infrared spectra at surfaces and interfaces

In this chapter we introduce a scheme for calculating from first principles the transverse-optical and the longitudinal-optical infrared absorption spectra at surfaces and interfaces. Furthermore, we describe a spatial decomposition for following the evolution of the infrared activity across the considered system.

After defining a proper framework for the calculation of infrared spectra (Sec. 3.1), we develop the procedure for obtaining the total absorption of surfaces and interfaces (Sec. 3.2). Then, we make a further step by showing how this procedure can be generalized in order to achieve a spatial decomposition of the infrared spectra (Sec. 3.3). Finally, we establish the connection with the local permittivity introduced in Chap. 2 (Sec. 3.4). The discussion of the computational details (Sec. 3.5) concludes this chapter.

3.1 Formulation of the problem

In a dielectric medium, transverse and longitudinal frequencies correspond to singularities and nodes of the dielectric function, respectively. Thus, in an *extended solid*, a phonon with a TO (LO) frequency carries a polarization field which is perpendicular (parallel) to the phonon wave vector $\mathbf{q}$. At variance, for a *thin film*, the Maxwell boundary conditions at the film surface imply that the polarization field associated to vibrational excitations is either perpendicular (TO) or parallel (LO) to the normal direction of the film [86, 41].

The absorption coefficients for a thin film can be expressed in terms of two key quantities, which we here refer to as the transverse (I_t) and longitudinal (I_ℓ) infrared absorption functions, and which can be expressed in terms of the dielectric response function ε (we omit tensor indices for clarity):

$$I_t(\omega) \;=\; \frac{\omega d}{c}\,\mathrm{Im}\,[\varepsilon(\omega)], \tag{3.1}$$

$$I_\ell(\omega) = \frac{\omega d}{c} \operatorname{Im}[-1/\varepsilon(\omega)], \tag{3.2}$$

where c is the speed of light, d the film thickness, and ω the frequency of the electromagnetic field. For instance, in the case of a free-standing thin film, the absorption coefficients for s- and p-polarized incoming radiation read

$$A_s(\omega) = I_t(\omega)/\cos\theta, \tag{3.3}$$
$$A_p(\omega) = [\cos^2\theta I_t(\omega) + \sin^2\theta I_\ell(\omega)]/\cos\theta, \tag{3.4}$$

where the prefactors only depend on the angle of incidence θ. In other situations, the specific scattering geometry or the optical effect of the substrate only give modifications of the prefactors of I_t and I_ℓ [86, 41, 37]. Therefore, the infrared spectra of a thin film are completely defined once the dielectric function of the film is known.

Equations (3.1) and (3.2) are based on the observation that, unlike an extended solid, the longitudinal modes of a thin film can couple to the electromagnetic radiation due to the boundary conditions at the film surface [86]. The explicit inclusion of retardation effects in the formalism, leading to the polariton dispersions, would not affect the results. Indeed, in the limit of very thin film, the polariton eigenfrequencies reduce to the TO and LO frequencies of the corresponding extended solid [87]. This limit is very well verified in the case of ultrathin SiO_2 films on Si(100), for which the typical thickness and wavenumber are $d \sim 1$ nm and $q \sim 1000$ cm^{-1}, respectively, resulting in a negligible phase shift $qd \sim 10^{-4}$ across the film.

3.2 Total absorption spectra

To calculate I_t and I_ℓ from first principles, we find it convenient to adopt dielectric functions $\varepsilon_t^{\mathrm{r}}$ and $\varepsilon_\ell^{\mathrm{r}}$ which are referred to the *external* electric field rather than to the macroscopic selfconsistent field [88]:

$$\varepsilon_t^{\mathrm{r}}(\omega) = 1 + 4\pi P_t(\omega)/E_t^{\mathrm{ext}}(\omega), \tag{3.5}$$

$$\varepsilon_\ell^{\mathrm{r}}(\omega) = 1 + 4\pi P_\ell(\omega)/E_\ell^{\mathrm{ext}}(\omega), \tag{3.6}$$

where P_t (P_ℓ) and E_t^{ext} (E_ℓ^{ext}) are the induced polarization and the external field along the transverse (longitudinal) direction. The dielectric functions $\varepsilon_t^{\mathrm{r}}$ and $\varepsilon_\ell^{\mathrm{r}}$ are related to the conventional one through [41]:

$$\varepsilon_t^{\mathrm{r}} = \varepsilon, \tag{3.7}$$
$$\varepsilon_\ell^{\mathrm{r}} = 2 - \varepsilon^{-1}. \tag{3.8}$$

Using these relations, the infrared absorption functions are simply expressed in terms of $\varepsilon_t^{\mathrm{r}}$ and $\varepsilon_\ell^{\mathrm{r}}$:

$$I_t(\omega) = \frac{\omega d}{c} \operatorname{Im}\left[\varepsilon_t^{\mathrm{r}}(\omega)\right], \tag{3.9}$$

$$I_\ell(\omega) = \frac{\omega d}{c} \operatorname{Im}\left[\varepsilon_\ell^{\mathrm{r}}(\omega)\right]. \tag{3.10}$$

The advantage of this formulation is that the determination of I_ℓ does not require the *explicit* inversion of the dielectric function. According to Eqs. (3.9) and (3.10), in order to obtain the infrared spectra of a thin film (either interfacial layer or surface), all we need is to compute the dielectric response functions $\varepsilon_t^{\mathrm{r}}(\omega)$ and $\varepsilon_\ell^{\mathrm{r}}(\omega)$.

In the following, we assume a supercell geometry and treat the lattice dynamics within the harmonic approximation. Hence, we do not explicitly compute phonon linewidths, even though the spectral broadening can in principle be included *a posteriori* through a separate evaluation of the phonon lifetimes [89].

3.2.1 Transverse-optical spectrum

To compute the dielectric response $\varepsilon_t^{\mathrm{r}}$ needed for the TO spectrum, we observe that the external field E_t^{ext} equals the macroscopic selfconsistent field E_t because of the Maxwell boundary conditions at the surface. Hence, $\varepsilon_t^{\mathrm{r}}$ of the computational cell is given by the standard expression for the dielectric function [52]:

$$\operatorname{Re}[\varepsilon_t^{\mathrm{r}}(\omega)] = \varepsilon_{\alpha\alpha}^{\infty} + \frac{4\pi}{\Omega} \sum_{IJ,\beta\gamma,n} \frac{Z^{\mathrm{B}}_{I,\alpha\beta}\xi^{t,n}_{I\beta}}{\sqrt{m_I}} \frac{Z^{\mathrm{B}}_{J,\alpha\gamma}\xi^{t,n}_{J\gamma}}{\sqrt{m_J}} (\omega^2 - \omega_{t,n}^2)^{-1}, \tag{3.11}$$

$$\operatorname{Im}[\varepsilon_t^{\mathrm{r}}(\omega)] = \frac{2\pi^2}{\Omega} \sum_{IJ,\beta\gamma,n} \frac{Z^{\mathrm{B}}_{I,\alpha\beta}\xi^{t,n}_{I\beta}}{\sqrt{m_I}} \frac{Z^{\mathrm{B}}_{J,\alpha\gamma}\xi^{t,n}_{J\gamma}}{\sqrt{m_J}} \frac{\delta(\omega-\omega_{t,n})}{\omega_{t,n}}. \tag{3.12}$$

Here, Ω is the volume of the supercell, m_I and $Z^{\mathrm{B}}_{I,\alpha\beta}$ are the mass and the Born charge for atom I, the index n runs over the vibrational modes, and the greek indices refer to Cartesian directions. In Eqs. (3.11), (3.12), the index α is taken along a transverse direction. The vibrational frequencies $\omega_{t,n}$ and their corresponding normalized eigenmodes $\xi^{t,n}_{I\alpha}$ result from the analytical part of the dynamical matrix.

By combining Eqs. (3.9) and (3.12), we obtain the transverse infrared absorption function:

$$I_t(\omega) = \frac{2\pi^2}{Ac} \sum_{IJ,\beta\gamma,n} \frac{Z^{\mathrm{B}}_{I,\alpha\beta}\xi^{t,n}_{I\beta}}{\sqrt{m_I}} \frac{Z^{\mathrm{B}}_{J,\alpha\gamma}\xi^{t,n}_{J\gamma}}{\sqrt{m_J}} \delta(\omega-\omega_{t,n}), \tag{3.13}$$

A being the supercell transverse area.

3.2.2 Longitudinal-optical spectrum

The longitudinal spectrum can be obtained through Eqs. (3.6) and (3.10) by expressing the induced polarization as a function of the external field $P_\ell = P_\ell(E_\ell^{\rm ext})$ rather than the macroscopic selfconsistent field E_ℓ. For this purpose, we first write the induced polarization along the longitudinal direction as a function of the selfconsistent macroscopic field [90]:

$$P_\ell = \frac{1}{4\pi}(\varepsilon^\infty_{\alpha\alpha} - 1)E_\ell + \frac{1}{\Omega}\sum_{I\beta} Z^{\rm B}_{I,\alpha\beta} u_{I\beta}(E_\ell), \tag{3.14}$$

where $u_{I\beta}(E_\ell)$ indicate the ionic displacements induced by the field E_ℓ, and α is along the longitudinal direction. Second, we write the dynamical equation for the harmonic motion of the ions [90]:

$$\omega^2 u_{I\beta}(\omega) = \sum_{J\gamma} C^{\beta\gamma}_{IJ} u_{J\gamma}(\omega) - Z^{\rm B}_{I,\beta\alpha} E_\ell. \tag{3.15}$$

Third, we state the relation between the external field $E_\ell^{\rm ext}$ and the macroscopic selfconsistent field E_ℓ along the longitudinal direction:

$$E_\ell^{\rm ext} = E_\ell + 4\pi P_\ell, \tag{3.16}$$

which follows from the conservation of the longitudinal component of the displacement field across the film surface. By combining Eqs. (3.14), (3.15), and (3.16) we obtain

$$\omega^2 u_{I\beta}(\omega) = \sum_{J\gamma} C^{\beta\gamma}_{\ell,IJ} u_{J\gamma}(\omega) - Z^{\rm C}_{I,\beta\alpha} E_\ell^{\rm ext}, \tag{3.17}$$

which is formally similar to Eq. (3.15), except for the replacement of the Born charges with the corresponding *Callen charges*, and the matrix of force constants C with the *longitudinal dynamical matrix* C_ℓ defined as follows:

$$C^{\beta\gamma}_{\ell,IJ} = C^{\beta\gamma}_{IJ} + \frac{4\pi}{\Omega}\frac{1}{\varepsilon^\infty_{\alpha\alpha}} Z^{\rm B}_{I,\beta\alpha} Z^{\rm B}_{J,\alpha\gamma}. \tag{3.18}$$

The induced displacements can now be evaluated by inverting Eq. (3.17) through the diagonalization of the matrix C_ℓ. By inserting the induced displacements in Eq. (3.14) and then using Eq. (3.6) we obtain the dielectric response to a longitudinal external field:

$$\mathrm{Re}[\varepsilon^{\rm r}_\ell(\omega)] = 2 - \frac{1}{\varepsilon^\infty_{\alpha\alpha}} + \frac{4\pi}{\Omega}\sum_{IJ,\beta\gamma,n} \frac{Z^{\rm C}_{I,\alpha\beta}\xi^{\ell,n}_{I\beta}}{\sqrt{m_I}} \frac{Z^{\rm C}_{J,\alpha\gamma}\xi^{\ell,n}_{J\gamma}}{\sqrt{m_J}} (\omega^2 - \omega^2_{\ell,n})^{-1}, \tag{3.19}$$

$$\mathrm{Im}[\varepsilon^{\rm r}_\ell(\omega)] = \frac{2\pi^2}{\Omega}\sum_{IJ,\beta\gamma,n} \frac{Z^{\rm C}_{I,\alpha\beta}\xi^{\ell,n}_{I\beta}}{\sqrt{m_I}} \frac{Z^{\rm C}_{J,\alpha\gamma}\xi^{\ell,n}_{J\gamma}}{\sqrt{m_J}} \frac{\delta(\omega-\omega_{\ell,n})}{\omega_{\ell,n}}, \tag{3.20}$$

The vibrational frequencies $\omega_{\ell,n}$ and their corresponding normalized eigenmodes $\xi_{I\alpha}^{\ell,n}$ correspond now to the longitudinal dynamical matrix. Note the appearance of the Callen charges in the oscillator strengths of Eqs. (3.19) and (3.20), as opposed to the Born charges of Eqs. (3.11) and (3.12).

Similarly to the transverse-optical case, by combining Eqs. (3.10) and (3.20), we obtain the longitudinal infrared absorption function:

$$I_\ell(\omega) = \frac{2\pi^2}{Ac} \sum_{IJ,\beta\gamma,n} \frac{Z^{\mathrm{C}}_{I,\alpha\beta}\xi^{\ell,n}_{I\beta}}{\sqrt{m_I}} \frac{Z^{\mathrm{C}}_{J,\alpha\gamma}\xi^{\ell,n}_{J\gamma}}{\sqrt{m_J}} \delta(\omega-\omega_{\ell,n}). \tag{3.21}$$

The infrared absorption functions given in Eqs. (3.13) and (3.21) carry an important additivity property. Indeed, the polarization appearing in Eq. (3.14) can be decomposed into localized dipolar contributions. By consequence, the total infrared absorption functions (either I_t or I_ℓ) of a multilayer structure can be expressed as the sum of the corresponding functions of the individual layers. This additivity property is also reflected in the expressions for I_t and I_ℓ which only involve local quantities as the *transverse* components of the Born charges and the *longitudinal* components of the Callen charges. Indeed, the transverse components of the Born charges can be calculated as the derivatives of the ionic forces with respect to the macroscopic transverse electric field, which is conserved across a multilayer structure. Therefore, the transverse components of the Born charges calculated for a bulk material and for the same material embedded in a layered structure do coincide (apart from the differences due to the structural relaxation). A similar observation holds for the longitudinal components of the Callen charges. Indeed, these can be calculated as derivatives of the ionic forces with respect to the longitudinal displacement field, which is again conserved across a multilayer structure [65].

In the case of an infrared-active film (either interfacial layer or surface) on a transparent substrate, the additivity of the absorption functions implies that $I_t(\omega)$ and $I_\ell(\omega)$ calculated for the full simulation cell through Eqs. (3.13) and (3.21) correspond to the absorption functions of the film alone, i.e. they do not depend on the extent of vacuum or substrate included in the simulation cell.

3.3 Local absorption spectra

In the case of an interface with a complex chemical grading, it is of interest to use the additivity of I_t and I_ℓ to analyze their spatial variation along the direction normal to the interface. This can be achieved by carrying out a derivation similar to that in Secs. 3.2.1 and 3.2.2. However, the *local* dielectric responses are now expressed with respect to the external electric field rather than to the macroscopic selfconsistent one. The local dielectric functions can be defined under the same assumptions of Sec. 2.1, and therefore are intended to describe the response of

atomistic layers with a thickness of $\sim$2–3 Å (so that nonlocality effects do not intervene in the formulation).

3.3.1 Transverse-optical spectrum

In this section we obtain the expression for the local transverse response $\varepsilon_t^{\mathrm{r}}(x;\omega)$ to the external electric field E_t^{ext}. We write the analogous of Eqs. (2.3) and (2.4):

$$\varepsilon_t^{\mathrm{r}}(x;\omega) = 1 + 4\pi \frac{\overline{\overline{p}}_t(x;\omega)}{E_t^{\mathrm{ext}}(\omega)}, \tag{3.22}$$

where the double bars indicate again the planar average along the transverse directions and a suitable smoothing along the longitudinal direction (cf. Sec. 2.1.1). The microscopic induced dipole density of an atomistic layer with coordinate x along the interface normal can be written in analogy with Eq. (3.14):

$$\overline{\overline{p}}_t(x;\omega) = \frac{1}{4\pi}(\varepsilon^{\infty}_{\alpha\alpha}(x) - 1)\overline{\overline{e}}_t(x;\omega) + \frac{1}{A}\sum_{I\beta} \zeta_{I,\alpha\beta} u_{I\beta}(E_t) w(x - X_I), \tag{3.23}$$

with α along a transverse direction. Here, the microscopic dipole is induced by the local transverse electric field $\overline{\overline{e}}_t(x;\omega)$, and the ionic contribution is taken into account via the effective dynamical charges $\zeta_{I,\alpha\beta}$, introduced in Sec. 2.1.3 in order to obtain a local dielectric response. In Eq. (3.23), $w(x)$ is a suitable normalized weight function localized around $x = 0$, and X_I is the ionic coordinate along the interface normal. The width of $w(x)$ should be chosen consistently with the decay length of the dynamical matrix. Now, we observe that

(i) the local transverse electric field equals the external transverse field:

$$\overline{\overline{e}}_t(x;\omega) = E_t^{\mathrm{ext}}(\omega), \tag{3.24}$$

(ii) the components of the effective charges and of the Born charges coincide along the transverse directions because of the definition in Eq. (2.24).

(iii) The displacements appearing in Eq. (3.23) are obtained from the dynamical equation for the harmonic motion of the ions [90]:

$$\omega^2 u_{I\beta}(\omega) = \sum_{J\gamma} C_{IJ}^{\beta\gamma} u_{J\gamma}(\omega) - Z^{\mathrm{B}}_{I,\beta\alpha} E_t(\omega). \tag{3.25}$$

By combining Eqs. (3.22) and (3.23), and making use of these observations, we obtain the local transverse response function $\varepsilon_t^{\mathrm{r}}(x;\omega)$:

$$\mathrm{Re}[\varepsilon_t^{\mathrm{r}}(x;\omega)] = \varepsilon^{\infty}_{\alpha\alpha}(x) + \frac{4\pi}{A}\sum_{IJ,\beta\gamma,n} \frac{Z^{\mathrm{B}}_{I,\alpha\beta}\xi^{t,n}_{I\beta}}{\sqrt{m_I}} \frac{Z^{\mathrm{B}}_{J,\alpha\gamma}\xi^{t,n}_{J\gamma}}{\sqrt{m_J}} (\omega^2 - \omega^2_{t,n})^{-1} w(x - X_I), \tag{3.26}$$

$$\mathrm{Im}[\varepsilon_t^{\mathrm{r}}(x;\omega)] = \frac{2\pi^2}{A}\sum_{IJ,\beta\gamma,n}\frac{Z^{\mathrm{B}}_{I,\alpha\beta}\xi^{t,n}_{I\beta}}{\sqrt{m_I}}\frac{Z^{\mathrm{B}}_{J,\alpha\gamma}\xi^{t,n}_{J\gamma}}{\sqrt{m_J}}\frac{\delta(\omega-\omega_{t,n})}{\omega_{t,n}}w(x-X_I). \tag{3.27}$$

The last equation allows us to write the density for the transverse infrared absorption function as

$$i_t(x,\omega) = \frac{2\pi^2}{Ac}\sum_{IJ,\beta\gamma,n}\frac{Z^{\mathrm{B}}_{I,\alpha\beta}\xi^{t,n}_{I\beta}}{\sqrt{m_I}}\frac{Z^{\mathrm{B}}_{J,\alpha\gamma}\xi^{t,n}_{J\gamma}}{\sqrt{m_J}}\delta(\omega-\omega_{t,n})w(x-X_I). \tag{3.28}$$

3.3.2 Longitudinal-optical spectrum

We now derive the expression for the local longitudinal response $\varepsilon_\ell^{\mathrm{r}}(x;\omega)$ to the external electric field E_ℓ^{ext}, following the same procedure outlined in the preceding section. The local dielectric response to the external field can be defined as

$$\varepsilon_\ell^{\mathrm{r}}(x;\omega) = 1 + 4\pi\frac{\overline{\overline{p}}_\ell(x;\omega)}{E_\ell^{\mathrm{ext}}(\omega)}, \tag{3.29}$$

with the microscopic induced dipole density

$$\overline{\overline{p}}_\ell(x;\omega) = \frac{1}{4\pi}(\varepsilon^\infty_{\alpha\alpha}(x)-1)\overline{\overline{e}}_\ell(x;\omega) + \frac{1}{A}\sum_{I\beta}\zeta_{I,\alpha\beta}u_{I\beta}(E_\ell)w(x-X_I). \tag{3.30}$$

Here, α is along the longitudinal direction, and $\overline{\overline{e}}_\ell(x;\omega)$ stands for the local longitudinal electric field. To derive an explicit expression for $\varepsilon_\ell^{\mathrm{r}}(x;\omega)$, we first observe that

(i) the local longitudinal electric field relates to the external field through:

$$\overline{\overline{e}}_\ell(x;\omega) + 4\pi\overline{\overline{p}}_\ell(x;\omega) = E_\ell^{\mathrm{ext}}(\omega), \tag{3.31}$$

(ii) the components of the effective charges along the longitudinal direction are related to the corresponding components of the Callen charges through Eq. (2.25),

(iii) the ionic displacements induced by the external electric field are given by Eq. (3.17), which involves the longitudinal dynamical matrix (cf. Sec. 3.2.2).

Next, we combine Eqs. (3.29) and (3.30), and make use of the previous observations to obtain

$$\mathrm{Re}[\varepsilon_\ell^{\mathrm{r}}(x;\omega)] = 2 - \frac{1}{\varepsilon^\infty_{\alpha\alpha}(x)} + \frac{4\pi}{A}\sum_{IJ,\beta\gamma,n}\frac{Z^{\mathrm{C}}_{I,\alpha\beta}\xi^{\ell,n}_{I\beta}}{\sqrt{m_I}}\frac{Z^{\mathrm{C}}_{J,\alpha\gamma}\xi^{\ell,n}_{J\gamma}}{\sqrt{m_J}}(\omega^2-\omega^2_{\ell,n})^{-1}w(x-X_I), \tag{3.32}$$

$$\mathrm{Im}[\varepsilon_\ell^{\mathrm{r}}(x;\omega)] = \frac{2\pi^2}{A}\sum_{IJ,\beta\gamma,n}\frac{Z^{\mathrm{C}}_{I,\alpha\beta}\xi^{\ell,n}_{I\beta}}{\sqrt{m_I}}\frac{Z^{\mathrm{C}}_{J,\alpha\gamma}\xi^{\ell,n}_{J\gamma}}{\sqrt{m_J}}\frac{\delta(\omega-\omega_{\ell,n})}{\omega_{\ell,n}}w(x-X_I). \tag{3.33}$$

As for the transverse case, the last equation allows us to write the local density of the longitudinal absorption function as

$$i_\ell(x,\omega) = \frac{2\pi^2}{Ac} \sum_{IJ,\beta\gamma,n} \frac{Z^{\mathrm{C}}_{I,\alpha\beta}\xi^{\ell,n}_{I\beta}}{\sqrt{m_I}} \frac{Z^{\mathrm{C}}_{J,\alpha\gamma}\xi^{\ell,n}_{J\gamma}}{\sqrt{m_J}} \delta(\omega-\omega_{\ell,n}) w(x-X_I). \tag{3.34}$$

At the end of the derivation which led to the infrared absorption functions Eqs. (3.13), (3.21), and to the corresponding local decompositions Eqs. (3.28), (3.34), it is interesting to note the remarkable symmetry between the expressions for the transverse and the longitudinal functions. Indeed, to switch from the TO to the LO spectrum it is sufficient to replace the Born charges by the corresponding Callen charges, and the transverse eigenmodes and eigenfrequencies by their longitudinal counterpart.

In analogy with Eq. (2.11), we find it convenient to define infrared absorption functions pertaining to a slab of finite thickness, delimited by the planes $x = x_1$ and $x = x_2$. From Eqs. (3.22) and (3.29) we find immediately

$$\varepsilon^{\mathrm{r}}_{t,\ell}([x_1,x_2];\omega) = \frac{1}{x_2-x_1} \int_{x_1}^{x_2} \varepsilon^{\mathrm{r}}_{t,\ell}(x,\omega)dx, \tag{3.35}$$

which combined with the definitions Eqs. (3.1) and (3.2) yields the infrared absorption function of the slab in terms of the corresponding absorption densities:

$$I_{t,\ell}([x_1,x_2];\omega) = \int_{x_1}^{x_2} i_{t,\ell}(x,\omega)dx. \tag{3.36}$$

The last equation corresponds to the additivity property discussed in Sec. 3.2.2.

3.4 Relation with the theory of the local permittivity

We here state the relation between the local permittivity introduced in Chap. 2 and the corresponding local responses to the external electric field introduced in the present chapter (Sec. 3.3). For this purpose, we combine Eqs. (3.22), (3.24), (3.29), and (3.31) with Eqs. (2.3) and (2.4) of Chap. 2 to obtain [41]:

$$\varepsilon_{\beta\beta}(x,\omega) = \varepsilon^{\mathrm{r}}_t(x,\omega) \tag{3.37}$$

$$\varepsilon_{\alpha\alpha}(x,\omega) = [2-\varepsilon^{\mathrm{r}}_\ell(x,\omega)]^{-1}, \tag{3.38}$$

where α is along the longitudinal direction, and β along a transverse direction. We note that the off-diagonal components of the dielectric tensor vanish because of the planar average, which induces a tetragonal symmetry in the system (cf. Sec. 2.1.1).

It is interesting to observe that, while $\varepsilon_{\alpha\alpha}(x,\omega)$ in Eq. (3.38) is obtained by using the eigenmodes of the *longitudinal* dynamical matrix through Eq. (3.32), it can also be expressed by making use of the *transverse* eigenmodes. To show this, we first write $\varepsilon_{\alpha\alpha}(x,\omega)$ through the microscopic induced dipole density and the corresponding local selfconsistent field according to Eqs. (2.3) and (2.4):

$$\varepsilon_{\alpha\alpha}(x,\omega) = 1 + 4\pi \frac{\overline{\overline{p}}_\alpha(x;\omega)}{\overline{\overline{e}}_\alpha(x;\omega)}. \tag{3.39}$$

Then, we express the induced dipole density $\overline{\overline{p}}_\alpha(x;\omega)$ through Eq. (3.23) by setting α along the longitudinal direction:

$$\overline{\overline{p}}_\alpha(x;\omega) = \frac{1}{4\pi}(\varepsilon^\infty_{\alpha\alpha}(x) - 1)\overline{\overline{e}}_\alpha(x;\omega) + \frac{1}{A}\sum_{I\beta} \zeta_{I,\alpha\beta} u_{I\beta}(E_\alpha) w(x - X_I). \tag{3.40}$$

The combination of Eqs. (3.39) and (3.40) yields

$$\varepsilon_{\alpha\alpha}(x,\omega) = \varepsilon^\infty_{\alpha\alpha}(x) + \frac{4\pi}{A}\sum_{I\beta} \zeta_{I,\alpha\beta} \frac{u_{I\beta}(E_\alpha)}{\overline{\overline{e}}_\alpha(x;\omega)} w(x - X_I). \tag{3.41}$$

Now, the electric field $\overline{\overline{e}}_\alpha(x;\omega)$ in the last equation can be eliminated through Eq. (2.10), which relates this field to the dielectric functions $\varepsilon_{\alpha\alpha}(\omega)$ and $\varepsilon_{\alpha\alpha}(x,\omega)$, and to the macroscopic selfconsistent field $E_\alpha(\omega)$:

$$\varepsilon_{\alpha\alpha}(\omega) E_\alpha(\omega) = \varepsilon_{\alpha\alpha}(x,\omega)\, \overline{\overline{e}}_\alpha(x;\omega). \tag{3.42}$$

Indeed, by replacing $\overline{\overline{e}}_\alpha(x;\omega)$ from Eq. (3.42) in Eq. (3.41) we obtain

$$\varepsilon_{\alpha\alpha}(x,\omega)\Big\{1 - \frac{1}{\varepsilon_{\alpha\alpha}(\omega)}\frac{4\pi}{A}\sum_{I\beta} \zeta_{I,\alpha\beta} \frac{u_{I\beta}(E_\alpha)}{E_\alpha(\omega)} w(x - X_I)\Big\} = \varepsilon^\infty_{\alpha\alpha}(x). \tag{3.43}$$

Finally, we express the ionic displacements through the transverse dynamical matrix according to Eq. (3.15), and the ionic effective charges in terms of the Born dynamical charges through Eq. (2.25), obtaining

$$\begin{aligned} \mathrm{Re}[\varepsilon_{\alpha\alpha}(x,\omega)] \;=\; & \Bigg\{ [\varepsilon^\infty_{\alpha\alpha}(x)]^{-1} - [\varepsilon^\infty_{\alpha\alpha}\varepsilon_{\alpha\alpha}(\omega)]^{-1} \\ & \times \frac{4\pi}{A} \sum_{IJ,\beta\gamma,n} \frac{Z^{\mathrm{B}}_{I,\alpha\beta}\xi^{t,n}_{I\beta}}{\sqrt{m_I}} \frac{Z^{\mathrm{B}}_{J,\alpha\gamma}\xi^{t,n}_{J\gamma}}{\sqrt{m_J}} (\omega^2 - \omega^2_{t,n})^{-1} w(x - X_I) \Bigg\}^{-1}. \end{aligned} \tag{3.44}$$

Equation (3.44) shows that it is indeed possible to calculate the local permittivity introduced in Chap. 2 not only through the longitudinal dynamical matrix [Eq. (3.38)], but also using the transverse dynamical matrix [Eq. (3.44)].

Overall, Eqs. (3.37), (3.38), and (3.44) provide a scheme for calculating local permittivities which is completely consistent with the theory developed in

Chap. 2. The difference resides in that the dielectric response was evaluated within Chap. 2 by means of a finite electric field approach, while the present chapter deals with linear response techniques.

It is important to realize that, while the methods developed in Chap. 2 and in the present chapter formally address the same physical quantity, in practice the choice between these methods will rely on considerations related to the computational cost. Indeed, while in principle the formalism introduced in Chap. 2 holds for every ω, the calculation of the induced charge density for an extended set of frequencies is computationally very demanding, and therefore the methods of the present chapter are more convenient when the full frequency-dependent dielectric function is needed. Conversely, when only the static ($\omega = 0$) and the high-frequency ($\omega = \infty$) permittivity profiles are needed, a calculation based on finite electric fields is more convenient than the determination of the whole dynamical matrix.

The previous considerations can be roughly summarized by saying that, in terms of computational efficiency, the methods developed in Chap. 2 are more suited for the two boundaries of the infrared frequency range, while the methods of the present chapter are more convenient for intermediate frequencies.

3.5 Practical implementation

To calculate the infrared absorption spectra across the Si(100)-SiO_2 interface (Chap. 6), we described the electronic structure through the local density approximation to density functional theory [91]. The latter choice for the exchange-correlation functional results into vibrational eigenfrequencies rather close to the experimental data, unlike the generalized gradient approximation adopted in Chap. 2 and in Chap. 5 [92]. As already stated in Sec. 2.2.1, we explicitely treated only the valence electrons, accounting for core-valence interactions through norm-conserving (Si [93]) and ultrasoft pseudopotentials (O [71]). We sampled the Brillouin zone of the supercell at the Γ point. We expanded the wave functions and the charge density on plane waves basis sets with energy cutoffs of 24 and 200 Ry, respectively [68, 69].

We evaluated the matrix of force constants by taking numerical derivatives of the atomic forces for displacements of ± 0.05 Å. Finite electric fields of ± 0.05 V/Å were used for the evaluation of the dynamical charges and of the electronic permittivity [53]. The Dirac delta functions in the Eqs. (3.12) through (3.34) were effectively replaced by Gaussian functions with standard deviation of $40\,\mathrm{cm}^{-1}$ in order to overcome the limited statistics within the disordered oxide [55], unless specified otherwise. We adopted a Gaussian function with a standard deviation of 1.5 Å as the spatial weight function $w(x)$ appearing in Eqs. (3.23) through (3.44).

Chapter 4

Structural models of the Si(100)-SiO_2 interface

In order to apply the general theory developed in Chap. 2 and Chap. 3 to the Si(100)-SiO_2 interface, we need to define suitable structural models. The present chapter is devoted to the description of the interface models that we adopted, including the generation procedure, the structural and the electronic properties. In Sec. 4.1 we describe two structures where the interface is modelled by matching a crystalline phase of the oxide to Si(100). In Sec. 4.2 we consider more sophisticated models, which take into account the disordered reconstruction at the interface, as well as the amorphous nature of the oxide.

4.1 Crystalline models of the Si-SiO_2 interface

4.1.1 Model generation

To construct model Si(100)-SiO_2 interfaces, we matched pseudomorphically ideal β-cristobalite to Si(100). The Si lattice parameter was chosen equal to 5.48 Å, corresponding to the relaxed lattice constant in our theoretical framework. The lattice parameter of the oxide in the [100] direction was determined by a separate relaxation, which gave a Si-O bond length of 1.63 Å, Si-O-Si angles of 179°, and O-Si-O angles of 114.6° and 107.0°. The corresponding experimental values for the amorphous oxide at the Si-SiO_2 interface are 1.61 Å, 147°–151°, and 109.4°, respectively [94, 95]. The density of the relaxed structure is 1.9 g/cm^3, about 15% lower than the experimental value of vitreous silica (2.2 g/cm^3).

The choice of β-cristobalite as a model oxide was motivated by the following observations. First, this SiO_2 polymorph allowed us to build Si-SiO_2-Si superlattices with equivalent Si-SiO_2 and SiO_2-Si interfaces. In this way, dipolar effects arising from asymmetric interface structures were avoided. Second, the oxide thickness could be varied in steps as small as 1.7 Å (corresponding to one SiO_2

"molecular layer"), allowing us to study the dielectric permittivity as a function of thickness with an atomic-layer "resolution".

In order to obtain a structural transition without coordination defects between the substrate and the oxide in our model interfaces, we adopted two different interface constructions, models C-I and C-II, which have been introduced in Ref. [21] and Ref. [96], respectively. In model C-I, all the partial oxidation states of Si, Si^{+1}, Si^{+2}, and Si^{+3}, appear in equal amounts of 0.5 MLs each. The thickness of the suboxide region is about 3 Å, and its average stoichiometry is $SiO_{1.0}$. In model C-II, the transition region extends over about 3 Å and includes 1 monolayer (ML) of Si^{+1} and 0.5 MLs of Si^{+2} partially oxidized Si atoms, with an average stoichiometry of $SiO_{0.7}$ (Fig. 4.1). Overall, the amount and the spatial distribution of the suboxides in both models qualitatively agree with photoemission measurements [15, 16].

For each interface model, we constructed several Si-SiO_2-Si superlattices with various oxide thicknesses by folding the interface structures thus obtained. For each model, we constructed 6 superlattices with 13 Si monolayers ($\simeq$ 16 Å) and up to 10 SiO_2 molecular layers ($\simeq$ 17 Å). In the remainder of this section, we will describe in detail the properties of the two Si-SiO_2-Si superlattices with the thickest oxides. In the plane of the interface, we used a 2×2 interface Si unit. We determined an optimal supercell size in the direction orthogonal to the interface planes, by separately relaxing a corresponding interface structure with exposed surfaces saturated by H atoms.

4.1.2 Structural properties

The relaxed structures of both superlattices showed typical bond lengths and bond angles [21, 31, 97]. We found an average Si-O bond length of 1.63 Å in the stoichiometric oxide. In the suboxide region, we found slightly larger bond

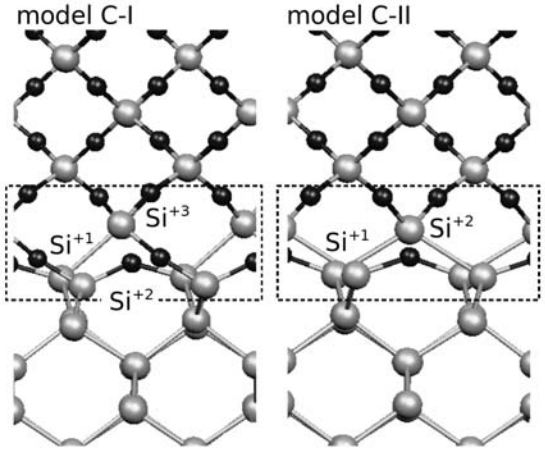

Figure 4.1: Ball-and-stick representation of model C-I (left) and model C-II (right) of the Si(100)-SiO_2 interface. Gray and black balls indicate Si and O atoms, respectively. The transition structure at the interface is indicated. In model C-I, the transition region includes 0.5 MLs of each of the intermediate oxidation states of Si, Si^{+1}, Si^{+2}, and Si^{+3}. In model C-II, the transition from Si to SiO_2 is achieved through 1 ML of Si^{+1} and 0.5 MLs of Si^{+2} species.

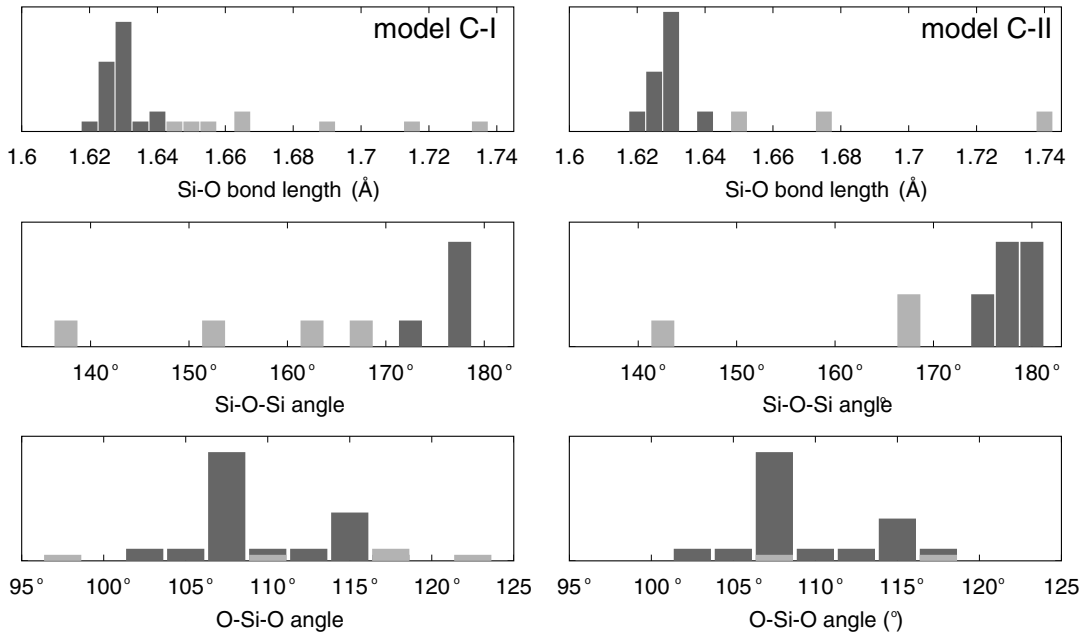

Figure 4.2: Si-O bond length, Si-O-Si and O-Si-O bond angles for model C-I (left) and model C-II (right) of the Si-SiO_2 interface. Dark bars pertain to the bulk SiO_2 region, while light bars correspond to interfacial bonds.

distances (1.67–1.74 Å), consistently with the less electronegative environment [31, 97]. The Si-O-Si and O-Si-O bond angles in the SiO_2 layers remain close to those of the corresponding bulk oxide. Figure 4.2 shows that the Si-O-Si and O-Si-O bond angles in the SiO_2 layers are close to those found for the corresponding bulk oxide.

4.1.3 Electronic structure

The local valence band maximum (VBM) and conduction band minimum (CBM) were determined as follows. First, we calculated the local density of states (DOS) according to

$$D(x;\epsilon) = 2\sum_n |\langle x|\psi_n\rangle|^2 \delta(\epsilon - \epsilon_n), \tag{4.1}$$

where x indicates a coordinate along the interface normal, $|\psi_n\rangle$ are the eigenstates of the Kohn-Sham Hamiltonian with eigenvalues ϵ_n, and the sum extends over both occupied and empty states. The Dirac delta functions in Eq. (4.1) were conveniently replaced by Gaussian functions with a standard deviation of 0.01 eV. Then, for every value of x, we determined the local band edges by requiring that the number of states falling between the supercell midgap and the band-edge equals a threshold value of 0.1 states/Å^3 [26]. The latter parameter was fixed by the condition that the minimum local band gap (i.e. the band gap deep inside Si) equals the supercell band gap. To determine the bulk VBM and CBM deep inside

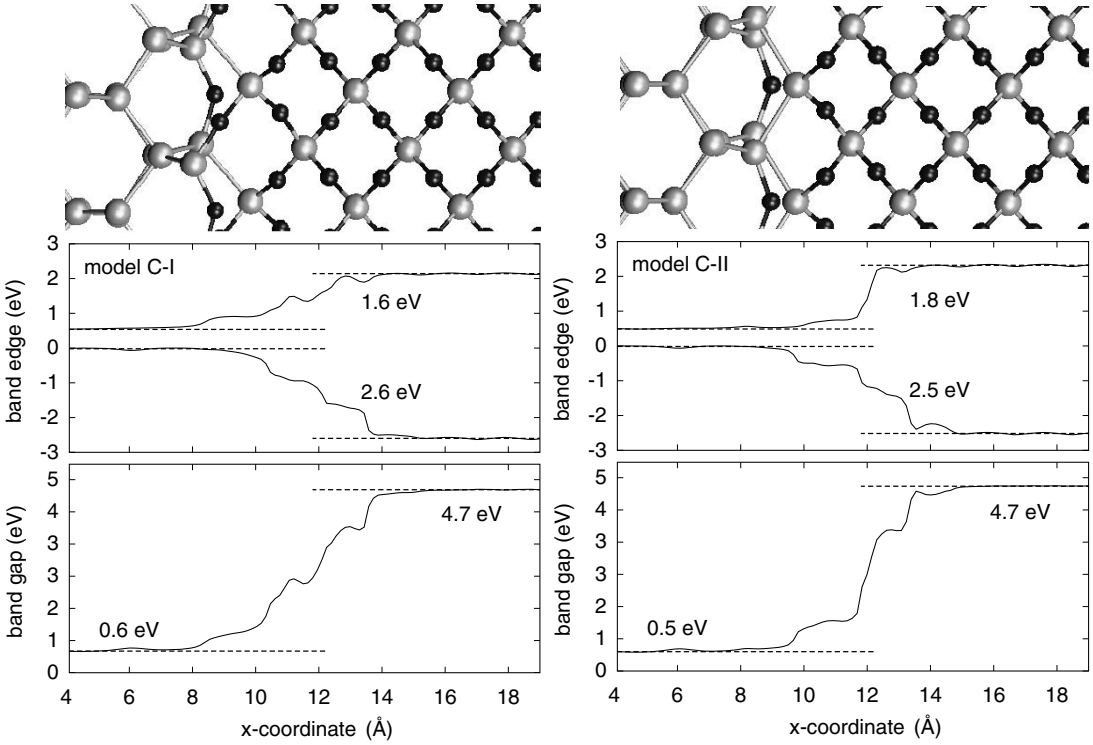

Figure 4.3: VBM, CBM and band gap for models C-I (left) and C-II (right) of the Si-SiO_2 interface (solid lines). The energy is referred to the Si VBM. The origin of the x-axis is taken at the Si midplane. The values in the respective bulk regions are shown as dashed lines. Ball-and-stick representations of the interface structure are shown on the top (gray balls correspond to Si atoms, black balls to O atoms). The band offsets at the interface and the band gaps deep inside each bulk region are given.

the Si and SiO_2 layers we adopted the double macroscopic average according to Ref. [98].

In Fig. 4.3, we report the local CBM, the VBM and the local band gap for both model interfaces. Deep inside the Si layer, we found band gaps of 0.6 eV and 0.5 eV for model C-I and C-II, respectively. The small difference between the models originates from the different quantum confinement effect experienced by the Si electrons due to the different suboxide structures. The gap in the oxide amounts to 4.7 eV for both models. The corresponding experimental values (1.1 eV and 8.9 eV for Si and SiO_2, respectively) are underestimated by about a factor two, as usual in density functional calculations. However, our results are in close agreement with calculations carried out on similar structures [99]. The calculated band offsets for model C-I (model C-II) are reported in Fig. 4.3 and amount to 1.6 eV (1.8 eV) for the conduction band and to 2.6 eV (2.5 eV) for the valence band. As for the band gaps, the calculated band offsets underestimate the experimental values of 3.1 and 4.3 eV [100, 101], but their magnitudes agree with other calculations for similar interface models [26, 102, 103]. The band edges in model

C-II are found to be shifted with respect to those in model C-I by 0.1 eV. These differences arise from the different interfacial dipoles in the two models. From Fig. 4.3, it is clear that the band gap and the band offsets are fully developed at a distance of only 5–6 Å from the substrate, in agreement with both theoretical [26] and experimental [5] investigations. The determination of the band edges allows the identification of silicon-induced gap states. Indeed, these states have energies located in the oxide gap. Their decay rate in the oxide can easily be evaluated through a linear fit of the charge density in a logarithmic plot. In particular, focusing on the *total* charge density of the induced gap states, we obtained a decay length of 1.2 Å for both valence and conduction states. This result implies that the silicon-induced gap states vanish at a distance of about 5–6 Å from the substrate, in accord with the transition width of the band edges. Thus, the present analysis clearly shows that the electronic structure of the interfacial oxide differs from its bulk counterpart.

The electronic structure of the model Si-SiO_2-Si superlattices can be alternatively described in terms of Wannier functions maximally localized along the direction orthogonal to the interfaces (Sec. 2.2.1). Indeed, a description in terms of localized electronic states allows us to identify and study specific bonding configurations. In Fig. 4.4, we show the yz average of the charge density associated to the maximally localized Wannier functions of our models C-I and C-II of the Si-SiO_2 interface. Outside of the suboxide region, both on the Si and SiO_2 side of the interface, the shape of the Wannier functions is almost independent of position, and is essentially the same in both models. The Wannier functions can be partitioned into three classes according to the location of their centers and the magnitude of their spreads [64]. At the Si-SiO_2 interface, we distinguish Wannier functions associated to Si-Si bonds, Si-O bonds, and nonbonding O orbitals.

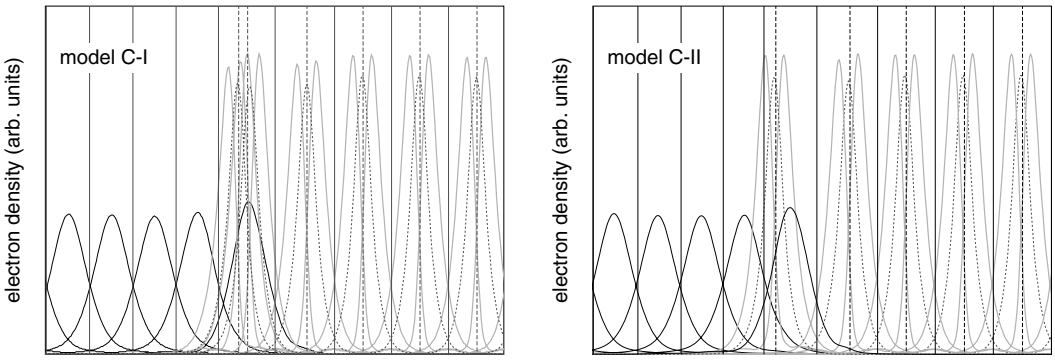

Figure 4.4: Planar average of the Wannier charge densities for model C-I (left) and C-II (right) of the Si-SiO_2 interface, along the [100] direction: Si-Si bonds (black solid), Si-O bonds (gray solid) and nonbonding O orbitals (black dotted). Vertical lines indicate planes of Si (solid) and O (dotted) atoms. As a reference, the Si interplane separation along the [100] direction is $\simeq$ 1.4 Å.

For the Wannier spreads of Si-Si bonds, Si-O bonds, and nonbonding O orbitals, we found 0.83 ± 0.05 Å, 0.43 ± 0.01 Å, and 0.40 ± 0.01 Å, respectively. Hence, the spread of the Wannier functions is a typical signature of the nature of these localized electronic states.

4.2 Disordered models of the Si(100)-SiO_2 interface

4.2.1 Model generation

More realistic models of the Si(100)-SiO_2 interface can be defined by requiring that the following atomic-scale properties derived from experiment be satisfied. First, the model structures should reproduce the disordered nature of the oxide [10]. Second, they should be consistent with the extremely low density of coordination defects (one defect out of 300 Si interface atoms) [12, 13]. Third, the mass density profile in the model structures should agree with X-ray reflectivity measurements, which yield an oxide density in proximity of the Si substrate between 2.3 and 2.4 g/cm^3 [104, 105], slightly denser than vitreous silica (2.2 g/cm^3). Fourth, the transition region should contain Si atoms in intermediate oxidation states in accord with Si 2p core-level photoemission experiments [15, 16]. Following the commonly accepted interpretation scheme [14, 17, 18], recent photoemission experiments yield 1.8 monolayers (1 ML $= 6.5 \cdot 10^{14}$ atoms/cm^2) of partially oxidized Si atoms, distributed between Si^{+1}, Si^{+2}, and Si^{+3} species according to the ratio of 1:2:3 [15, 16], with the Si^{+1} and Si^{+2} atoms located right at the interface, and the Si^{+3} ones distributed within a few Si-O bond lengths from the interface.

The Si(100)-SiO_2 model structures were generated by constructing -Si-SiO_2-Si- superlattices based on the transition structures obtained in Refs. [31, 32]. As already mentioned in Sec. 4.1.1, the superlattice geometry allowed us to avoid complications arising from silicon-vacuum and oxide-vacuum interfaces. Furthermore, the superlattice arrangement is a convenient way to model the substrate-oxide-polysilicon system within a supercell calculation. Hence, for each model considered, we mirrored the structure with respect to a Si substrate plane parallel to the interface, so as to obtain opposite Si-SiO_x and SiO_x-Si junctions, separated by a vacuum region. Then, in each case, we generated stoichiometric SiO_2 in the central vacuum by introducing Si and O atoms randomly, and performing a melt-end-quench cycle with classical pair-potentials [106]. The [100] cell parameters were chosen so as to obtain melts at the experimental density of vitreous SiO_2. This resulted in Si-SiO_2 superlattices with substoichiometric transition regions and disordered oxides. In order to release the residual strain, we further relaxed the atomic positions through first-principle molecular dynamics (cf. Secs. 2.2 and 3.5). Overall, we obtained three structural models of the

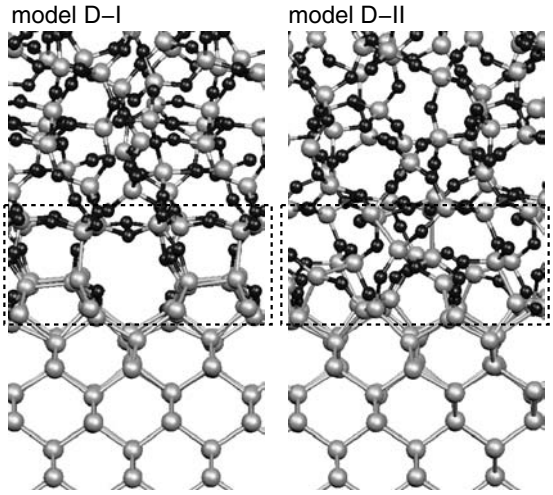

Figure 4.5: Ball-and-stick representation of model D-I (left) and model D-II (right) of the Si(100)-SiO_2 interface. In model D-I, the interfacial layer is characterized by a high density of in-plane Si-Si dimers with a large fraction of oxidized backbonds. In model D-II, the transition from Si to SiO_2 takes place through a highly disordered interfacial layer. The transition structure of model D-III (not shown) is similar to that of model D-II.

Si(100)-SiO_2 interface, which hereafter we will refer to as model D-I, D-II, and D-III, respectively (Fig. 4.5). Models D-I and D-II consist of 315 and 313 atoms, respectively, distributed in 13 Si layers and 2.5 nm of oxide, within simulation cells of size $\simeq 11\times11\times45$ Å^3. Model D-III consists of 217 atoms distributed in 9 Si layers and 1.6 nm of oxide, within a simulation cell of size $\simeq 11\times11\times30$ Å^3. The transition structure of model D-I corresponds to model B of Ref. [32], where the terminating Si layer shows a high density of in-plane Si-Si dimers, with a high fraction of oxidized backbonds. The transition structure of model D-II corresponds to model C' of Ref. [32], where the structure of the terminating Si layer is adapted from a structure generated previously by first-principles molecular dynamics [23]. The transition structure of model D-III was obtained from that corresponding to model D-II by replacing a Si-Si bond in the first Si layer by a Si-O-Si bridge. The latter model (D-III) was generated in order to reduce the computational cost in the calculation of the vibrational eigenmodes (cf. Chap. 6).

During the final relaxation of the atomic coordinates, the supercell parameter along the [100] direction was kept fixed for models D-I and D-II. This choice eventually led to some degree of strain in the structures. However, both the final density of the Si layers and the distribution of bond-lengths and bond-angles in the amorphous oxides (cf. Sec. 4.2.2) indicate that this effect is not significant. For model D-III, we relaxed the supercell parameter along the [100] direction since the vibrational frequencies are sensitive to small but finite values of the atomic forces in the relaxed configuration. To fully relax the structure we proceeded as follows. We first unfolded the Si-SiO_2-Si superlattice by cutting it at the Si midplane. Then, we saturated the resulting free surfaces by H atoms. The resulting structure was heated for 0.4 ps through two Nosé-Hoover thermostats [107, 108], one at 800 K for the oxide region, and the other at 40 K for the Si layers. Then, the system was cooled down in 0.4 ps and allowed to relax through damped molecular dynamics.

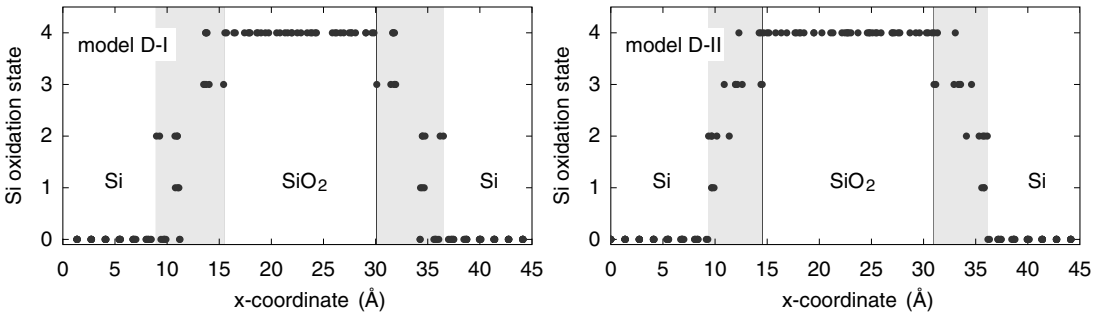

Figure 4.6: Spatial distribution of Si atoms in model D-I (left) and model D-II (right) of the Si-SiO_2-Si structure. The x axis is perpendicular to the interface, with the origin at the Si midplane. Si atoms are grouped according to the corresponding oxidation number (vertical axis). The shaded areas indicate the extent of the suboxide regions. The distribution for model D-III (not shown) is similar to that of model D-II.

4.2.2 Structural properties

Our model Si-SiO_2 transition structures are free of coordination defects, consistently with the extremely low density of interface states deduced from electrical and electron-spin measurements [12, 13]. The amount, distribution and location of Si atoms in intermediate oxidation states is in good agreement with angle-resolved Si-2p core-level photoemission spectroscopy [15, 16], as shown in Table 4.1. The spatial distribution of the suboxide species (Fig. 4.6) indicates that, for all the interface models considered, the Si^{+1} and Si^{+2} species are concentrated close to the outermost Si layer, while the Si^{+3} states are spread over a broader region, in accord with experiment [16]. The thickness of the substoichiometric oxides, which we here define as the distance between the farmost partially oxidized Si atoms, is 6.4 Å for model D-I, 5.1 Å for model D-II, and 6.1 Å for model D-III. The simulation of ion scattering experiments in the channeling geometry with ion energies between 0.4 and 1.0 MeV gives an excess Si yield of 2.7 ± 0.1 MLs for model D-I, of 2.9 ± 0.1 MLs for model D-II, and of ∼2.8 MLs for model D-III. The excess Si yield of model D-III was estimated by taking into account

Table 4.1: Distribution of partially oxidized Si atoms: comparison between our model Si(100)-SiO_2 interfaces and two recent photoemission experiments. Values are in monolayers.

	Model D-I	Model D-II	Model D-III	Ref. [15]	Ref. [16]
Si^{+1}	0.37	0.37	0.37	0.3	0.36
Si^{+2}	0.62	0.62	0.74	0.6	0.64
Si^{+3}	0.62	0.87	0.87	0.9	1.06

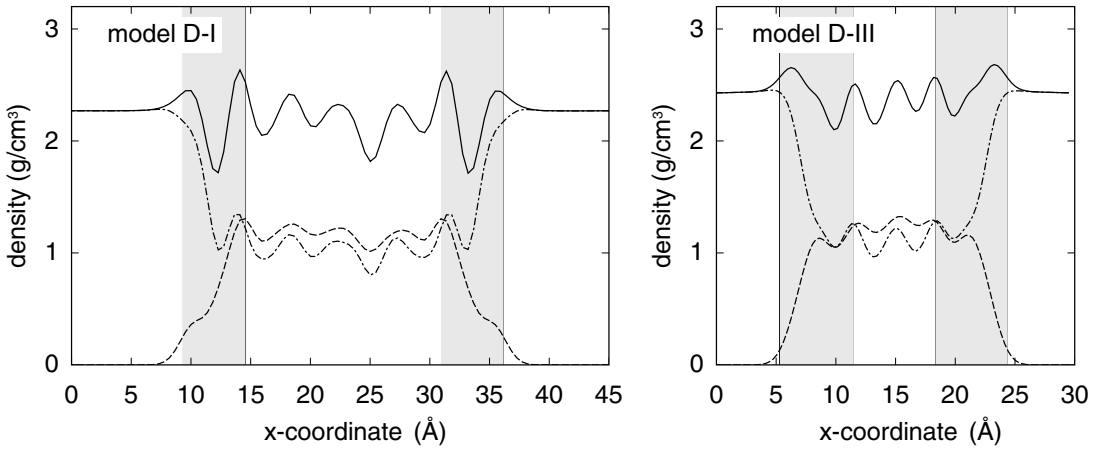

Figure 4.7: Mass-density profile across the model Si-SiO_2-Si structures D-I (left) and D-III (right). Full density is shown by a solid line, while partial Si and O densities are indicated by dashed and dash-dotted lines, respectively. We used a Gaussian broadening with a standard deviation of 1 Å along the interface normal (x), and a planar average in the directions parallel to the interface plane (yz). The origin of the x axis is taken at the Si midplane. The density profile for model D-II (not shown) is similar to that of model D-I.

a decrease of the suboxide Si yield of 0.06 MLs with respect to model D-II, according to Ref. [32]. These values are in good agreement with the experimental result of 3.0 ± 0.3 MLs [32]. In addition, model D-II was found to match the ion-scattering data for ion energies ranging up to 2 MeV [109], and to reproduce the experimental strain vs. depth profile [110] associated to distortions in the direction perpendicular to the plane of the interface [111].

Figure 4.7 shows the mass-density profile across the interface models D-I and D-III. The density of the oxide in proximity of the substrate is $\simeq 2.3$ g/cm^3 for model D-I and D-II, and $\simeq 2.4$ g/cm^3 for model D-III, in accord with reflectivity measurements [104, 105]. Inside the oxide region the density decreases down to 2.2 g/cm^3 (model D-I), 2.1 g/cm^3 (model D-II) and 2.3 g/cm^3 (model D-III). The latter values are close to the experimental density of vitreous silica (2.2 g/cm^3).

The bond-length and bond-angle distributions for the considered model structures are shown in Fig. 4.8, together with their decomposition into contributions from partially and fully oxidized Si atoms. The corresponding average values and standard deviations are reported in Table 4.2. The mean Si-O bond length in the stoichiometric oxide of the interface models D-I and D-II is slightly larger (2%) than the experimental value for vitreous silica. Conversely, the mean Si-O bond length in the oxide of model D-III is smaller (1%) than the experimental values. These differences arise from the use of the generalized gradient approximation to density functional theory for model D-I and D-II, and of the local density approximation for model D-III. Indeed, the local density approximation of the exchange

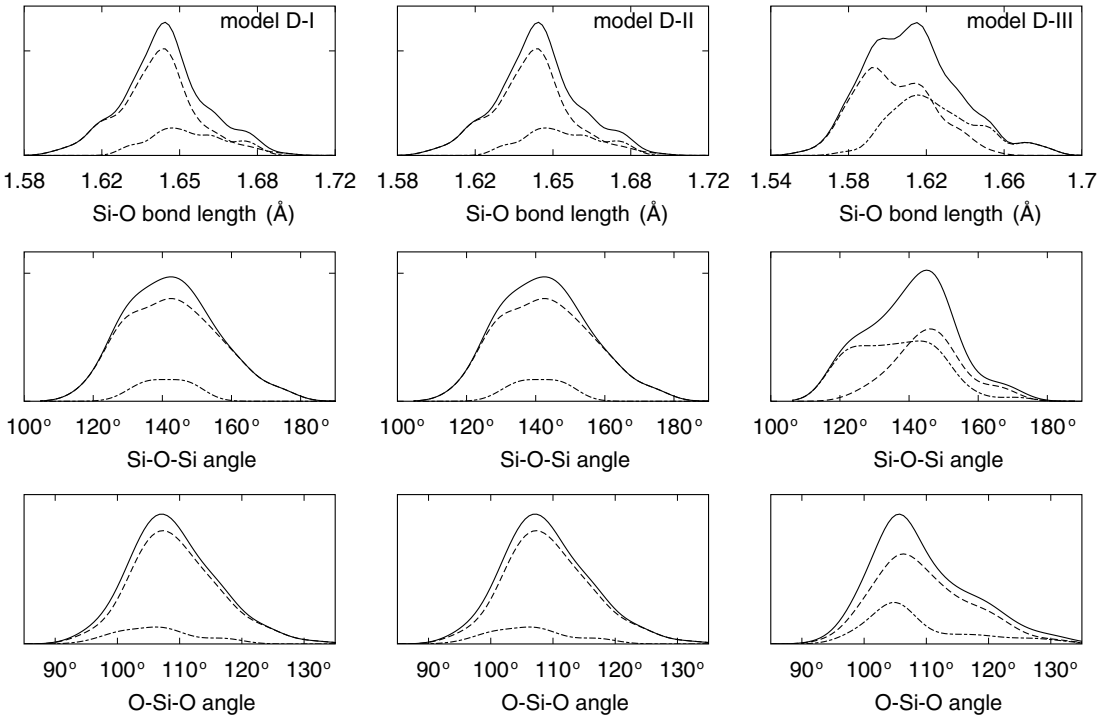

Figure 4.8: Distribution of Si-O bond-length, Si-O-Si and O-Si-O bond-angles for the model Si-SiO_2-Si structures considered in this work (solid): models D-I (left), D-II (middle) and D-III (right). The distributions corresponding to partially oxidized (dash-dotted) and to fully oxidized (dashed) Si atoms are reported separately. We used Gaussian broadenings of 0.005 Å for the bond length distributions, and of 5° (3°) for the Si-O-Si (O-Si-O) bond-angle distributions.

Table 4.2: Average Si-O bond-length, Si-O-Si and O-Si-O bond-angles calculated for the distributions shown in Fig. 4.8. Uncertainties represent the corresponding standard deviations. We report separately the values for the whole structures, for the suboxide regions, and for the stoichiometric oxides.

		Full	Suboxide	Si^{+4}
D-I	Si-O (Å)	1.64 ± 0.02	1.65 ± 0.02	1.64 ± 0.02
	∠ Si-O-Si	142.7° ± 12.6°	140.9° ± 6.1°	143.0° ± 13.2°
	∠ O-Si-O	109.1° ± 6.8°	106.4° ± 5.9°	109.5° ± 6.8°
D-II	Si-O (Å)	1.65 ± 0.03	1.67 ± 0.03	1.64 ± 0.02
	∠ Si-O-Si	142.0° ± 14.3°	130.7° ± 9.3°	144.3° ± 14.1°
	∠ O-Si-O	109.1° ± 6.5°	107.6° ± 7.3°	109.4° ± 6.3°
D-III	Si-O (Å)	1.61 ± 0.02	1.63 ± 0.02	1.60 ± 0.02
	∠ Si-O-Si	140.6° ± 13.1°	136.3° ± 13.0°	146.0° ± 11.0°
	∠ O-Si-O	109.3° ± 8.2°	108.6° ± 8.9°	109.5° ± 7.9°

and correlation energy is known to underestimate the experimental bond lengths, while the generalized gradient approximation usually yields bond lengths in excess of the experimental value [70]. The differences in the bond lengths are reflected in the different densities of the Si regions (Fig. 4.7): we calculated a relaxed Si crystal lattice constant of 5.48 Å within the generalized gradient approximation, and of 5.38 Å within the local density approximation. The Si-O bond-length in the suboxide regions is larger than that found in the stoichiometric oxide regions, due to the less electronegative suboxide environment, which is responsible for a weakening of the Si-O bond [97]. O-Si-O angles are peaked at the tetrahedral value within the stoichiometric oxide regions, indicating that tetrahedral coordination is well preserved in our models. Finally, the distributions of the Si-O-Si angle averages to 143° (model D-I), 144° (model D-II), and 146° (model D-III) in the SiO_2 regions, quite close to measured angles for vitreous silica (147°–151°) [95].

4.2.3 Electronic structure

Figure 4.9 shows the local conduction band minimum, the valence band maximum, and the local band gap calculated for the model interfaces with disordered oxides. Deep inside the Si layer, the band gaps are found to be 0.8 eV (models D-I and D-II) and 0.7 eV (model D-III). Deep into the oxide we calculated band gaps of 5.1 eV (model D-I), of 5.0 eV (model D-II), and of 4.7 eV (model D-III). The difference between the Si band gaps in models D-I, D-II and model D-III is due to the different exchange-correlation functional adopted in each case. The slightly smaller oxide band gap of model D-III arises from the overlap of the Si gap states in the middle of the oxide. The corresponding experimental values are underestimated by about a factor two, as is often the case in density functional calculations [112]. The calculated valence band offsets are 2.5 eV (model D-I), 2.4 eV (model D-II), and 2.2 eV (model D-III), while the corresponding conduction band offsets are 1.8 eV for all models. As for the band gaps, the calculated band offsets also underestimate the experimental values, consistently with our calculations on the crystalline interface models (cf. Sec. 4.1.3). Table 4.3 summarizes the calculated band gaps and band offsets and compares our results with previous calculations and with our results for the crystalline interface models. Despite the different model oxides, the calculated values follow approximately the same trend. We note, in particular, that the slightly different band gaps calculated for the Si layers relate to the specific degree of quantum confinement experienced by the Si electrons in the model structures. The difference of ∼0.5 eV between the valence band offsets evaluated in this work and those of Ref. [113] can be ascribed to differences in the evaluation procedure and in the model interfacial transition layers adopted. Finally, we point out that the asymmetry between the experimental valence and conduction band offsets is preserved in our results. Figure 4.9 shows that the oxide band gap and the band offsets are fully developed only about one

"SiO_2 molecular layer" (2–3 Å) away from the suboxide region, corresponding to a distance of about 8–9 Å from the last nonoxidized Si atoms in the substrate. The width of the transition region for the electronic properties is larger than what we found for the crystalline interface models (Sec. 4.1.3), consistently with the broader spatial distribution of the suboxide species in the disordered model structures.

Focusing on the silicon-induced gap states *near the Si band edges*, we calculated a decay length in the oxide of $\simeq 1.2$ Å for both hole and electron gap states. This result is in good agreement with measurements of leakage current density as a function of oxide thickness, which indicate a current decay rate of about one decade per 2 Å of oxide thickness [114]. In fact, on the basis of a simple model for the tunneling current [115], the latter estimate can be translated into a decay length of the gap states of 1.15 Å, rather close to the value we obtained for the oxide in our model structures.

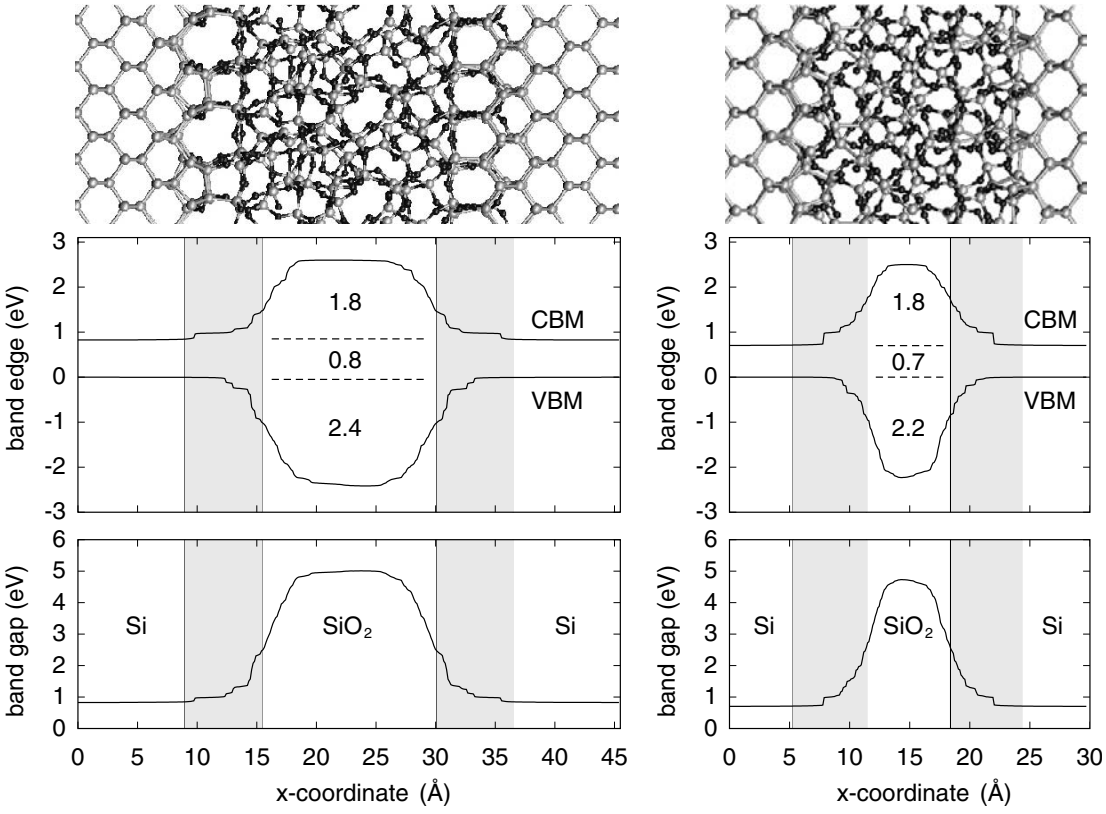

Figure 4.9: Conduction band minimum (CBM), valence band maximum (VBM) and band gap profiles across models D-I (left) and D-III (right) of the Si(100)-SiO_2 interface, plotted along the interface normal (x). The shaded areas indicate the suboxide regions. A ball-and-stick representation of the model structure is also shown on the top. The behavior of model D-II (not shown) is similar to that of model D-I.

Table 4.3: Calculated band gaps, valence and conduction band offsets for the model D-I–III of the Si-SiO_2 interface. All values are in eV and refer to the band edges evaluated in the middle of the Si and SiO_2 layers. For comparison, we also report our results for the crystalline models of the Si-SiO_2 interface, results of previous works, and the experimental data. The experimental valence band offset is from Ref. [100]. The conduction band offset is from Ref. [101], assuming a Si band gap of 1.1 eV.

	E_{2gap}^{Si}	$E_{gap}^{SiO_2}$	VBO	CBO
model D-I	0.8	5.1	2.5	1.8
model D-II	0.8	5.0	2.4	1.8
model D-III	0.7	4.7	2.2	1.8
model C-I	0.6	4.7	2.6	1.6
model C-II	0.5	4.7	2.5	1.8
Ref. [26], Q-model	1.2	5.4	2.2	2.0
Ref. [113]	–	–	3.0	–
Experiment	1.1	8.9	4.3	3.1

Chapter 5

Dielectric permittivity of ultrathin oxides on Si(100)

In this chapter, we address the dielectric permittivity across the Si(100)-SiO_2 interface. Using the interface models described in Chap. 4, we are able to show that the dielectric transition from the silicon to the oxide occurs within a width of only a few angstroms. The polarizability associated to intermediate oxidation states of Si is found to be enhanced with respect to bulk SiO_2, resulting in a larger permittivity of the interfacial suboxide layer with respect to the stoichiometric oxide. Furthermore, the silicon induced gap states are found to play a secondary role in the enhancement of the permittivity of the interfacial layer. Therefore, the dielectric transition at the Si-SiO_2 interface has to be associated to the chemical grading.

By adopting the crystalline structural models C-I and C-II (Sec. 5.1), we investigate first the limits of a classical description of the Si(100)-SiO_2 interface in terms of two adjacent dielectrics. Then, we apply the scheme developed in Chap. 2 to determine the local permittivity and the corresponding ionic and electronic polarizabilities (Sec. 5.2). Through the Wannier decomposition of the permittivity profile, we are able to identify the contribution of silicon-induced gap states to the permittivity in the interfacial oxide. The application of the local permittivity method to the more realistic interface models D-I and D-II (Sec. 5.3) confirms the picture outlined in Sec. 5.2 and provides more realistic estimates of the interfacial oxide permittivity.

5.1 Classical modeling of the permittivity of the interfacial layer

Before applying the local permittivity method to the model interfaces considered in Chap. 4, we here investigate the limits of a description of the Si(100)-SiO_2 interface based on classical dielectric slabs.

For this purpose, we calculated the permittivity of SiO_2 films on Si(100) as a function of oxide thickness. By applying finite electric fields to the superlattice structures C-I and C-II, we were able to determine the permittivities of the whole supercell, corresponding to two Si-SiO_2 interfaces connected back-to-back. We obtained the permittivity of a single interface relying on the following consideration. Every superlattice is symmetric with respect to both the semiconductor and oxide midplanes. Virtual cuts along these planes result in two identical Si-SiO_2 interfaces, connected back-to-back. Because of this symmetry, the permittivity of each interface taken separately equals that of the whole superlattice. In order to extract the permittivity of the oxide overlayer from the values corresponding to a single Si-SiO_2 interface, we removed the substrate contribution using the prescription for two capacitors connected in series:

$$\frac{t_{SiO_2^*}}{\varepsilon_{SiO_2^*}} = \frac{t_{SL}}{\varepsilon_{SL}} - \frac{t_{Si}}{\varepsilon_{Si}} \tag{5.1}$$

where SL stands for (half of the) superlattice, and t for thickness. SiO_2^* represents the oxide overlayer, including both 1.5 MLs of SiO_x suboxide and the pure SiO_2 oxide. The permittivity of the silicon substrate appearing in Eq. (5.1) was determined by a separate bulk calculation (Sec. 2.2.2). Applying Eq. (5.1) to each considered structure, we are able to extract the electronic $\varepsilon^{\infty}_{SiO_2^*}$ and static $\varepsilon^{0}_{SiO_2^*}$ permittivities of the oxide overlayer as a function of its thickness $t_{SiO_2^*}$.

The results of our calculations for the dielectric permittivity of the SiO_2^* overlayer are shown in Fig. 5.1. The static and high-frequency permittivities increase with decreasing oxide thickness for both model interfaces. This confirms that the first few atomic layers of oxide near the substrate do not behave as their bulk

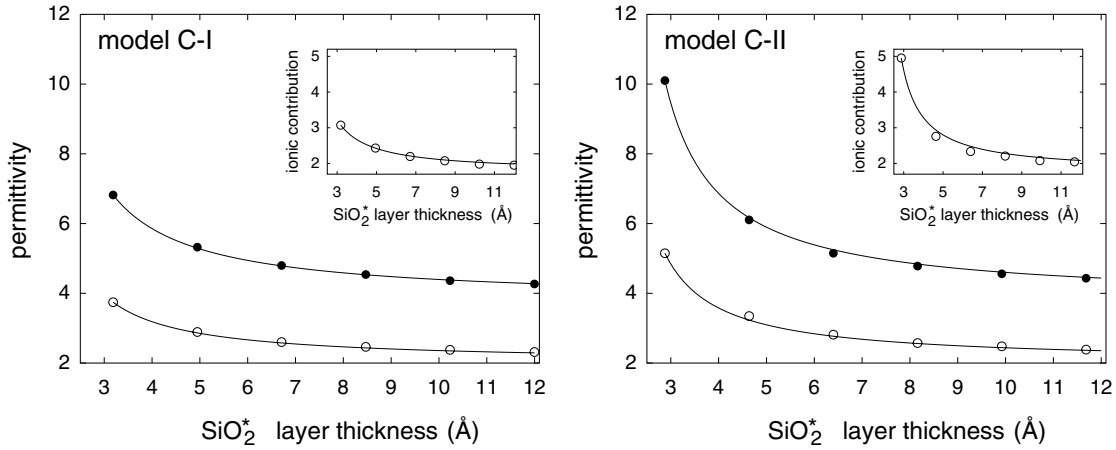

Figure 5.1: Static (disks) and high-frequency (open circles) dielectric permittivity of the oxide overlayer SiO_2^* plotted vs its thickness, together with the trend obtained from the simplified model discussed in the text (solid lines). In the insets, we report the ionic contributions to the static permittivity.

counterpart. In model C-II, the high-frequency permittivity reaches the value of $\varepsilon_\infty = 5.1$, while the static permittivity increases up to $\varepsilon_0 = 10.1$. In model C-I the enhancement is less pronounced, with maximal values for ε_∞ and ε_0 of 3.7 and 6.8, respectively. It is worth to point out that the increase in the static permittivity results from the enhancement of both the electronic and the ionic screening (Fig. 5.1, insets).

The permittivity increase with decreasing thickness shown in Fig. 5.1 can be accounted for by a hyperbolic relationship, as one can see by plotting $1/\varepsilon_{\mathrm{SiO}_2^*}$ vs $1/t_{\mathrm{SiO}_2^*}$. This led us to further decompose the permittivity of the SiO_2^* overlayer into contributions from the suboxide monolayer and the pure oxide, as if they were two distinct capacitors in series. For this purpose, we extracted the permittivities of the suboxide ($\varepsilon^\infty_{\mathrm{SiO}_x}$ and $\varepsilon^0_{\mathrm{SiO}_x}$) from the superlattices without any fully oxidized Si atoms. The permittivities of the stoichiometric oxide were obtained from separate bulk calculations as follows. We considered a β-cristobalite model of SiO_2 with lattice parameters adapted to match the Si lattice (Sec. 4.1). We used the same electric field as determined for silicon in Sec. 2.2.2, since the larger band gap of SiO_2 ensures that this field falls within the linear regime. The dependence of the electronic and static permittivities with cell size shows a L_x^{-2} asymptotic behavior. Extrapolation to infinite cell size gave an electronic permittivity of $\varepsilon^\infty_{\mathrm{SiO}_2} = 2.0$ and a static permittivity of $\varepsilon^0_{\mathrm{SiO}_2} = 3.8$. The permittivity of the oxide overlayer can then be written as

$$\varepsilon_{\mathrm{SiO}_2^*} = \left[\frac{t_{\mathrm{SiO}_x}}{t_{\mathrm{SiO}_2^*}}\varepsilon^{-1}_{\mathrm{SiO}_x} + \left(1 - \frac{t_{\mathrm{SiO}_x}}{t_{\mathrm{SiO}_2^*}}\right)\varepsilon^{-1}_{\mathrm{SiO}_2}\right]^{-1}. \tag{5.2}$$

The result of Eq. (5.2) is shown in Fig. 5.1 by solid lines. Comparing the values of $\varepsilon_{\mathrm{SiO}_2^*}$ from Eq. (5.2) with those obtained directly from the density-functional calculations, we found a maximum deviation of only 1.3%.

The agreement between the *three-layer model* and the first-principles calculations indicates that it is possible to describe classically the dielectric properties of the Si-SiO_2 interface, provided at least three distinct dielectric units are considered: the substrate, the suboxide, and the pure SiO_2 oxide.

5.2 Local permittivity at the Si-SiO_2 interface: crystalline models

5.2.1 Permittivity profile across the interface

Following the procedure outlined in Chap. 2, we calculated the *local* permittivity profiles along a direction normal to the interfaces for models C-I and C-II (Fig. 5.2). These profiles were obtained separately for the electronic and ionic permittivities.

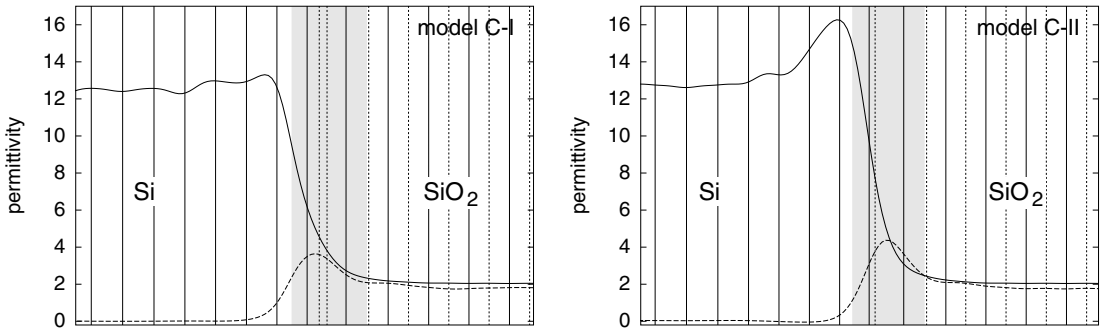

Figure 5.2: Permittivity profiles across model C-I (left) and model C-II (right) of the Si(100)-SiO_2 interface: electronic permittivity (solid) and lattice contribution $\varepsilon_0(x) - \varepsilon_\infty(x)$ (dashed). Vertical lines indicate planes of Si (solid) and O (dotted) atoms. The shaded area represents the suboxide transition layer.

The local electronic permittivity varies across the interface, decreasing from the silicon value to the SiO_2 one. The transition is about 6 Å thick and includes the full suboxide region. In the stoichiometric oxide, the electronic permittivity is constant and starts increasing only within the suboxide region. This result is consistent with recent Auger measurements which showed that the oxide permittivity agrees with that of bulk SiO_2 for distances from the interface larger than 6 Å [35]. To understand the enhancement of the local electronic permittivity on the silicon side of the interface, we carried out the decomposition into Wannier contributions introduced in Sec. 2.1.2 (Fig. 5.3). This decomposition shows that the observed bumps result from asymmetric dipolar contributions associated to Si-Si bonds of the suboxide, peaked towards the interior of the silicon slab (cf. Appendix C). This contribution is larger in model C-II, since (i) the number of Si-Si bonds in this model is about 30% larger than in model C-I, and (ii) the Si-Si bonds in

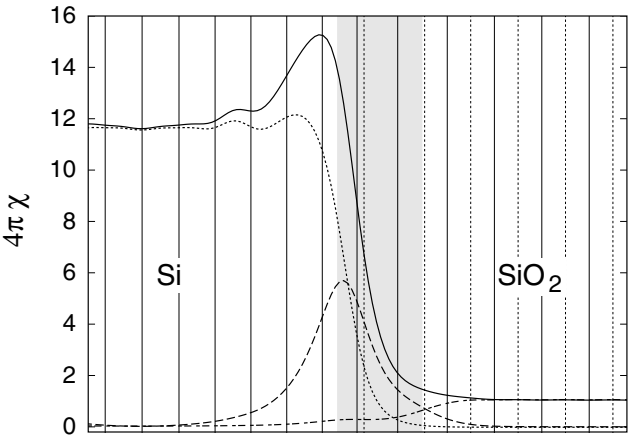

Figure 5.3: Profile of the local electronic susceptibility across model C-II of the Si(100)-SiO_2 interface (solid line). Contributions to the susceptibility arising from Wannier functions of the Si slab (dotted), the suboxide (dashed), and the oxide (dash-dotted) are shown separately. The shaded area represents the suboxide transition layer. Vertical lines indicate planes of Si (solid) and O (dotted) atoms.

model C-II are more polarizable than in model C-I due to their larger average bond length (2.66 Å in model C-II vs. 2.52 Å in model C-I), consistently with the discussion in Sec. 2.3.1. We refer to Appendix C for a detailed analysis of the origin of this effect.

We obtained the ionic contribution to the permittivity given in Fig. 5.2 by replacing the ionic point charges by Gaussian functions with standard deviations of 1 Å. In the stoichiometric oxide, the ionic contribution assumes a constant value corresponding to bulk SiO_2 (cf. Sec. 5.1). Similarly, the ionic contribution vanishes in the silicon bulk, because of the vanishing dynamical charges (Sec. 5.2.2). In the suboxide, the ionic contribution is found to exceed the SiO_2 bulk value in both models. The origin of this effect will be clarified in Sec. 6.2.1.

For practical applications, it is convenient to approximate the permittivity profile through a three-layer model, assigning an average permittivity to each of the three regions: Si, SiO_x and SiO_2. We defined the planes separating the silicon substrate and the suboxide on the basis of the amount of nonoxidized Si atoms and the bulk silicon density. We defined similarly the separation between the suboxide and the stoichiometric oxide. Using Eq. (2.11), we obtain the individual slab permittivities given in Table 5.1. Several comments are in order:

(i) The difference (1–2%) between the static and electronic permittivities of the Si slabs results from the contribution of the outermost Si layers. Analogously, the permittivities of the SiO_2 layers are within 2% from those estimated for the bulk (Sec. 5.1), due to the slightly larger polarizability of the first oxide layer.

(ii) It is particularly satisfactory to note that the slab permittivities derived here from the local permittivity profile differ by less than 10% from the values derived in Sec. 5.1 from a classical analysis. The small differences result from assigning *bulk* permittivities to the Si and SiO_2 slabs in the

Table 5.1: Electronic (ε_∞) and static (ε_0) permittivities of the Si, SiO_x and SiO_2 components of the Si(100)-SiO_2 model interfaces C-I and C-II. For each component, we also report separately the lattice contribution $\Delta\varepsilon = \varepsilon_0 - \varepsilon_\infty$. Values between brackets correspond to the local permittivity in the middle of the Si slab.

	model C-I				model C-II			
	Si		SiO_x	SiO_2	Si		SiO_x	SiO_2
ε_∞	12.6	(12.4)	3.8	2.1	13.5	(12.6)	5.0	2.1
ε_0	12.8	(12.4)	6.8	3.9	13.6	(12.6)	9.1	3.9
$\Delta\varepsilon$	0.2	(0.0)	3.0	1.8	0.1	(0.0)	4.1	1.8

classical analysis. Thus the enhanced screening in the outermost Si and SiO_2 layers is effectively transferred to the suboxide.

(iii) Note that the local permittivity in the Si interior (12.4 and 12.6 for models C-I and C-II, respectively) is smaller than the permittivity of an extended bulk, $\varepsilon_{\mathrm{Si}} = 14.3$ (Sec. 2.2.2). This effect arises from the size-dependence of the Berry-phase position operator in supercell calculations (Sec. 2.2.2), and counteracts the overestimation due to the transverse Brillouin zone sampling, thus bringing the permittivity of the Si region close to the fully converged value (cf. Sec. 2.3). While the size-dependence of the position operator introduces an error of 13% on the permittivity of the Si region, the corresponding errors for the suboxide and the oxide regions are smaller than 3%, as we estimated by applying a saw-tooth shaped potential to a SiO_2-Si-SiO_2 slab with oxide surfaces terminated by H atoms.

(iv) The suboxide shows a permittivity which is larger than that of bulk SiO_2: $\varepsilon^0_{\mathrm{SiO}_x} = 6.8$ for model C-I and $\varepsilon^0_{\mathrm{SiO}_x} = 9.1$ for model C-II (Table 5.1), to be compared with $\varepsilon^0_{\mathrm{SiO}_2} = 3.8$. This result is consistent with electrical measurements on Si-SiO_2-ZrO_2 gate stacks, which indicate that the oxide interlayer carries an enhanced permittivity ranging between 6 and 7 [33].

5.2.2 Discrete electronic and ionic polarizabilities

In this section, we describe the local polarizability in terms of discrete dipoles, both electronic and ionic, following Sec. 2.1.3. Electronic dipoles are primarily associated to bonds, while ionic dipoles are more easily related to atoms. To treat both kind of dipoles on an equal footing, we adopted Si-centered polarizable units based on the first-neighbor shell. We assigned all the Wannier functions pertaining to a given Si atom to the polarizable unit centered on that atom. The polarizability of such a unit is then obtained by adding up the individual polarizabilities of its component Wannier functions (Sec. 2.1.3). Care was taken to account for Wannier functions shared among different units, such as Si-Si bonds and nonbonding O orbitals, with the proper weight of 1/2.

The polarizabilities obtained in this way are shown in Fig. 5.4 for the two model Si-SiO_2 interfaces C-I and C-II. Again, we find that the Si and SiO_2 bulk behavior is recovered within a distance of a few angstroms from the interface, in accord with the analysis in Sec. 5.2.1. Notice that the outermost Si layers show a polarizability close to the value of the inner layers, while a bump is observed in the local permittivity profile (Fig. 5.2). In our discrete formulation, the contribution leading to the bump is concentrated in the polarizable units belonging to the suboxide region (cf. Appendix C). The insets of Fig. 5.4 show that there is a monotonic relation between the oxidation state of the central Si atom in the polarizable unit and the corresponding polarizability.

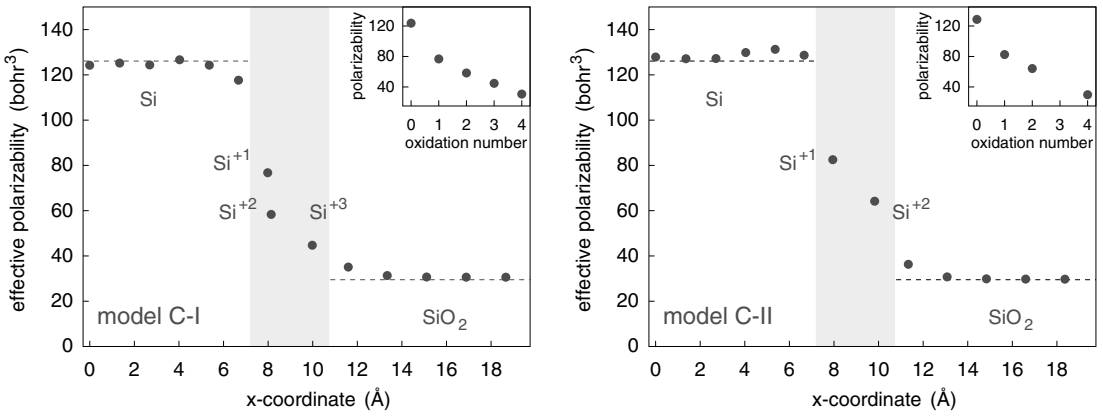

Figure 5.4: Effective electronic polarizabilities of Si-centered polarizable units, for model C-I (left) and model C-II (right) of the Si(100)-SiO$_2$ interface. The x axis is oriented along the [100] direction. Horizontal dashed lines indicate the values calculated for the corresponding bulk materials. The shaded area indicates the suboxide region. Insets: effective electronic polarizability vs the oxidation state of the central Si atom in the polarizable unit.

The lattice contribution to the dielectric screening was evaluated as described in Sec. 2.1.3. As a reference, we first determined the transverse Born charges for bulk SiO$_2$ (Sec. 4.1.1), obtaining $Z^{\mathrm{B}}_{xx,\mathrm{Si}} = 3.30$ and $Z^{\mathrm{B}}_{xx,\mathrm{O}} = 1.65$ for Si and O atoms, respectively. These values agree well with previous calculations for crystalline [116] and amorphous SiO$_2$ [55]. Figure 5.5 shows the calculated effective charges ζ_{xx} across our model Si-SiO$_2$ interfaces. The effective charges correctly reproduce the reference values obtained for bulk SiO$_2$ in the stoichiometric oxide, and vanish in the silicon substrate except for the outermost layer. The insets of Fig. 5.5 show a monotonic increase of the effective charges with the Si oxidation state.

The calculated effective charges ζ_{xx} were used to determine the effective ionic polarizabilities through Eq. (2.26). Figure 5.6 shows the calculated effective ionic polarizabilities pertaining to the polarizable units defined above for models C-I and C-II. Inside the silicon slab, these polarizabilities vanish due to the vanishing effective charges. Within the oxide, the polarizabilities coincide with the values determined for the corresponding bulk. For the polarizable units adjacent to the suboxide region, both on the Si and SiO$_2$ sides of the interface, we observe only slight departures from the bulk values. In the insets, we give the polarizability of the polarizable units as a function of the oxidation state of the central Si atom. Disregarding momentarily the value for the Si^{+2} oxidation state in model C-II, the polarizability vs oxidation state shows a rather smooth behavior with a maximum in correspondence of the Si^{+2} oxidation state. This result is in accord with the enhanced static permittivity recorded in the suboxide region (Fig. 5.2). The higher polarizability value found for the Si^{+2} oxidation state in model C-II is related to the occurrence of a Si-Si bond with a bond length of 2.66 Å, con-

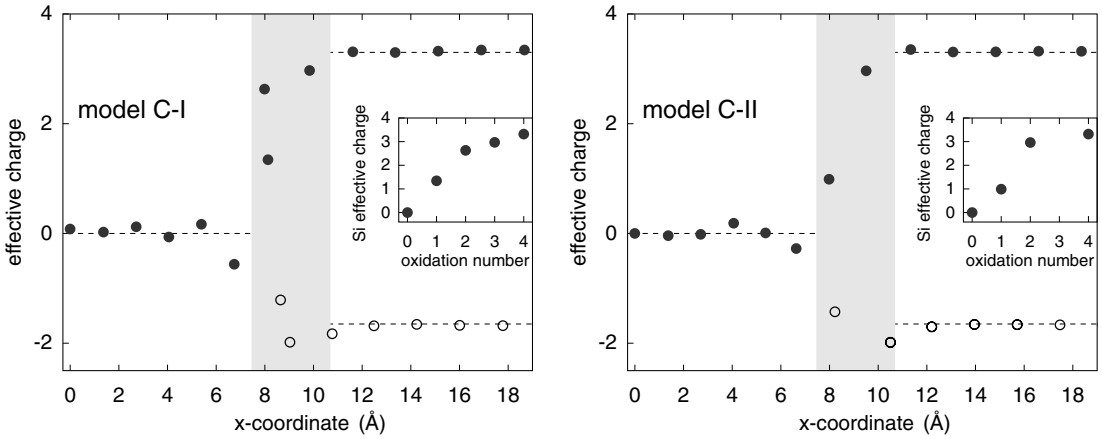

Figure 5.5: Effective charges $\zeta_{I,xx}$ for model C-I (left) and model C-II (right) of the Si(100)-SiO_2 interface. Disks correspond to Si atoms, circles to O atoms. The x axis is oriented along the [100] direction. Horizontal lines indicate the values of the Born dynamical charges calculated for each bulk material separately. Insets: Si effective charges vs Si oxidation state.

siderably larger than the bond length of 2.35 Å found for the corresponding Si^{+2} polarizable unit in model C-I.

Overall, the analysis in terms of discrete polarizabilities conveys the same picture as the local permittivity profile. In addition, this analysis highlights the relation between the dielectric transition across the Si-SiO_2 interface and the chemical grading.

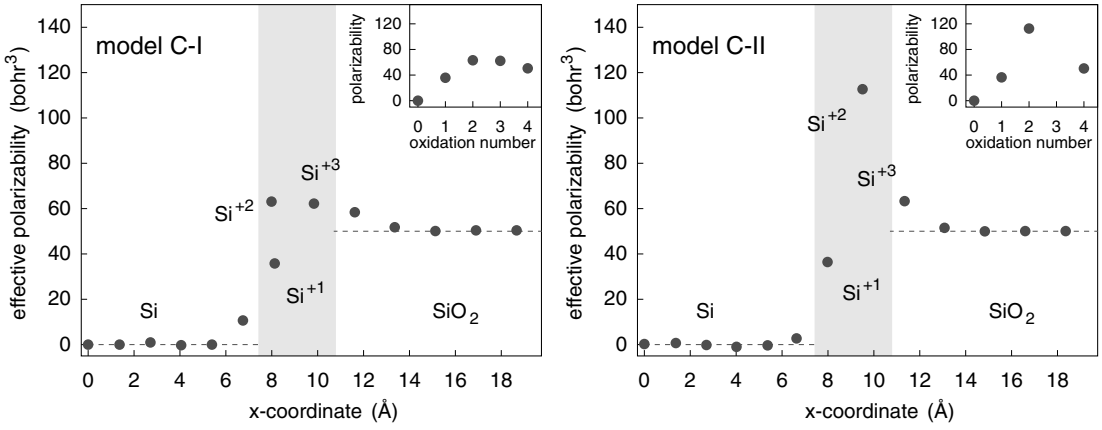

Figure 5.6: Effective ionic polarizabilities of the Si-centered polarizable units, for model C-I (left) and C-II (right) of the Si(100)-SiO_2 interface. The x axis is oriented along the [100] direction. Horizontal dashed lines indicate the values calculated separately for the corresponding bulk materials. The shaded area indicates the suboxide region. Insets: effective ionic polarizability vs Si oxidation state.

5.2.3 Role of silicon-induced gap states

At variance with our findings, the dielectric transition at Si-SiO_2 interfaces has previously been related to the tails of Si states at energies located inside the SiO_2 band gap [5, 7], in analogy to the metal induced gap states at metal-semiconductor contacts [117, 118, 119]. These tails extend into the oxide for about 5 Å, contributing to a reduction of the gap in the local density of states (cf. Secs. 4.1.3, 4.2.3). To investigate the role of such tails, we retain for each Wannier function a fraction of its contribution to the microscopic polarization, corresponding to its projection onto the occupied electronic states lying inside the oxide gap. Figure 5.7 shows that the combination of these contributions decays into the oxide on a similar length scale as the formation of the oxide gap (cf. Fig. 4.3). In the near-interface oxide (first 5 Å), the contribution from gap states amounts to only 13% of the total electronic permittivity, indicating that their role is secondary.

This assertion is further supported by considering the Schottky pinning factor S of the oxide. The pinning factor is used in the theory of metal-semiconductor contacts to describe the change in the band lineup due to metal-induced states in the semiconductor gap [120, 121, 122, 123]. It is related to the surface density of gap states ($D_{\rm GS}$), the corresponding extent into the semiconductor ($\delta_{\rm GS}$), and the permittivity of the interfacial layer ($\varepsilon_{\rm IL}$) through [122, 123]:

$$S \simeq \frac{1}{1 + 4\pi e^2 D_{\rm GS}\delta_{\rm GS}/\varepsilon_{\rm IL}}. \tag{5.3}$$

Furthermore, the contribution of the induced gap states to the permittivity of the interfacial oxide can be written to a first approximation as [124]:

$$\chi_{\rm GS} \simeq e^2 D_{\rm GS}\delta_{\rm GS}. \tag{5.4}$$

The combination of Eqs. (5.3) and (5.4) yields the following relation between the Schottky factor and the contribution of the silicon-induced gap states to the permittivity:

$$S \simeq \frac{1}{1 + 4\pi\chi_{\rm GS}/\varepsilon_{\rm IL}}. \tag{5.5}$$

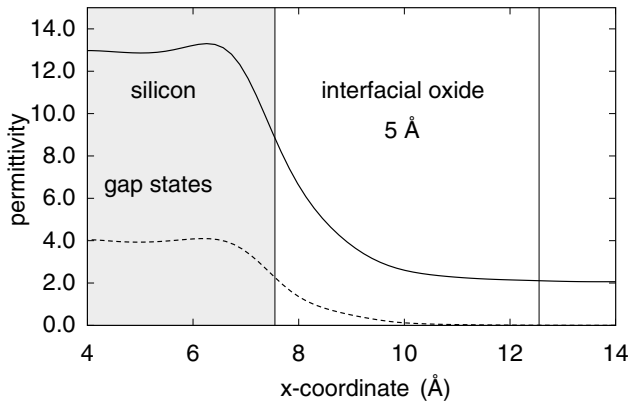

Figure 5.7: Local electronic permittivity (solid, from Fig. 5.2) for model C-I of the Si(100)-SiO_2 interface, together with the contribution from gap states (dots). The Si region is shaded. The first 5 Å of oxide where the contribution of the induced gap states was evaluated are indicated (interfacial oxide).

By using the calculated contribution of the gap states to the permittivity ($4\pi\chi_{\rm GS} = 0.13\ \varepsilon_{\rm IL}$) in Eq. (5.5), we estimated a Schottky factor for SiO_2 of 0.88. This result is in fair agreement with experimental data (0.70–0.86) [122, 123], supporting our conclusion that the induced gap states play a secondary role in the mechanism leading to an enchanced permittivity in the near-interface oxide.

5.3 Local permittivity at the Si-SiO_2 interface: disordered models

While Secs. 5.1 and 5.2 were mainly devoted to the understanding of the dielectric transition between Si(100) and SiO_2 through simplified structural models, we now address the permittivity of the near-interface oxide through the *realistic* models D-I and D-II introduced in Chap. 4.

5.3.1 Permittivity profile

Along the same lines of Sec. 5.2, we calculated the local permittivity profiles across the interface models D-I and D-II. These profiles were determined separately for the high-frequency and the static permittivities (Fig. 5.8). The high-frequency and static permittivities in the middle of the Si slab approximately coincide, due to the vanishing dynamical charges at a sufficiently large distance from the interface. The calculated static permittivity, $\varepsilon^0_{\rm Si} = 12.5$ for both model interfaces, slightly overestimates the experimental value of 11.9. This is mainly due to the inherent error of the adopted density functional scheme [125], since the convergence errors related to the transverse Brillouin zone sampling and to the Γ point representation of the position operator approximately cancel (cf. Sec. 5.2.1).

We evaluated an average high-frequency permittivitty of 2.3 for the stoichiometric oxides of both model interfaces. The corresponding static permittivities are 4.2 and 4.0 for model D-I and model D-II, respectively. Also in this case, the calculated permittivities slightly overestimate the experimental values (2.1 and 3.9 for the high-frequency and the static permittivity, respectively). The difference between the static permittivities of the oxides in our models can be traced back to their different mass densities. Indeed, a correlation between density and dielectric permittivity is clearly observed when comparing the corresponding profiles in Fig. 5.8 (a) and (b).

The permittivities of the substoichiometric oxide amount to $\varepsilon_{SiO_x} = 6.9$ and $\varepsilon_{SiO_x} = 5.7$ for model D-I and model D-II, respectively. The difference mainly arises from the different spatial distributions and orientations of the suboxide Si-Si bonds. Our calculations are consistent with indirect experimental measurements which assign a static permittivity between 6 and 7 to the interfacial layer [33]. Furthermore, Figure 5.8 shows that the permittivity of bulk SiO_2 is recovered as soon as the Si atoms become fully oxidized, i.e. at a distance of about 5–6 Å from

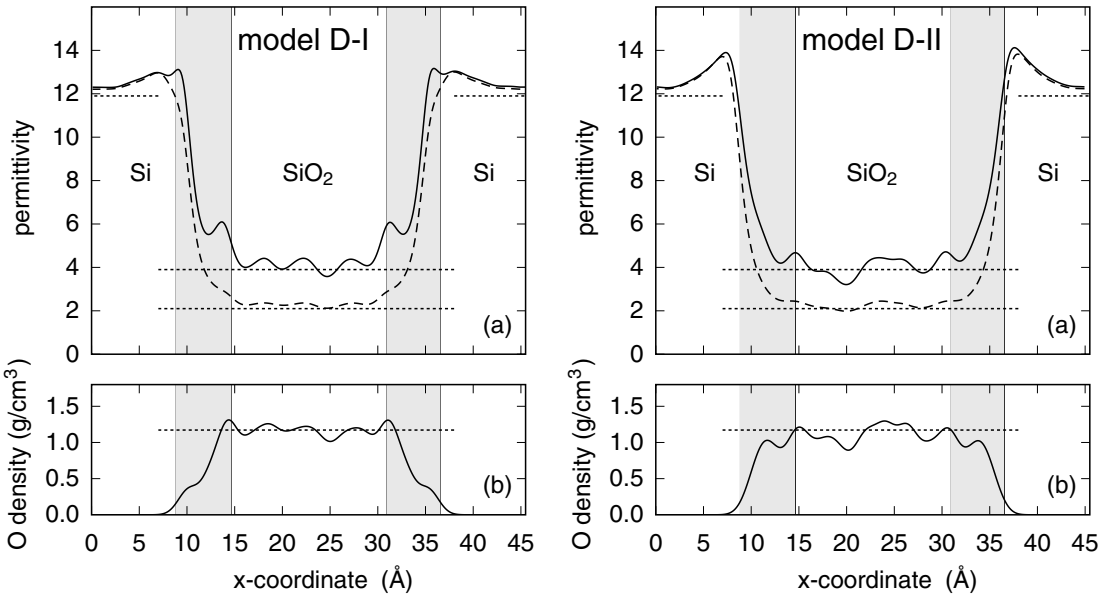

Figure 5.8: (a) High-frequency (dashed) and static (solid) permittivity profiles for model D-I (left) and D-II (right) of the Si(100)-SiO_2 interface. Horizontal dotted lines indicate the experimental values for bulk Si and bulk vitreous silica. (b) O density profile for model D-I (left) and D-II (right). The horizontal dotted lines indicate the density of O atoms in bulk SiO_2. The shaded regions indicate the location of partially oxidized Si atoms.

the substrate. This result is consistent with Auger measurements indicating that the bulk SiO_2 high-frequency permittivity is already recovered at a distance of 6 Å from the substrate. Finally, a detailed analysis shows once again that the enhanced permittivity in the outermost Si layers of the substrate results from the screening provided by Si–Si bonds in the adjacent suboxide (cf. Sec. 5.2.1 and Appendix C).

It is interesting at this stage to compare the permittivity profile with the shape of the local band edges. Indeed, from Figs. 4.9 and 5.8 we see that the local band edges approach the bulk levels only at a distance of 2–3 Å from the suboxide region, at variance with the local permittivity which becomes bulk-like as soon as the oxide becomes stoichiometric. This is consistent with our results for the crystalline interface models, which show that the enhanced screening of the interfacial oxide relates to the presence of partially oxidized Si atoms, and only little owes to the silicon-induced gap states (cf. Sec. 5.2.3).

In Table 5.2, we summarize our results and present a comparison with the permittivities calculated for the crystalline interface models and with experiment. Interestingly, the permittivities of the models C-I, D-I and D-II are all in good agreement. The larger screening of the suboxide in model C-II has been discussed in Sec. 5.2.1.

Table 5.2: Calculated high-frequency and static permittivities of the silicon, suboxide, and oxide regions for all the considered Si(100)-SiO_2 interface models. The experimental permittivity for the substoichiometric oxide is taken from Ref. [33].

	$\varepsilon^{\infty}_{\mathrm{Si}}$	$\varepsilon^{0}_{\mathrm{Si}}$	$\varepsilon^{\infty}_{\mathrm{SiO}_x}$	$\varepsilon^{0}_{\mathrm{SiO}_x}$	$\varepsilon^{\infty}_{\mathrm{SiO}_2}$	$\varepsilon^{0}_{\mathrm{SiO}_2}$
Model C-I	12.4	12.4	3.8	6.8	2.1	3.9
Model C-II	12.6	12.6	5.0	9.1	2.1	3.9
Model D-I	12.4	12.5	4.2	6.9	2.3	4.2
Model D-II	12.3	12.5	3.4	5.7	2.3	4.0
Experiment	11.9	11.9	—	6–7	2.1	3.9

5.3.2 Implications for device scaling and thin-film metrology

The enhanced permittivity of the substoichiometric oxide indicates that the equivalent oxide thickness of an oxide interlayer (including the substoichiometric region) between Si and a high-permittivity material is smaller than its physical thickness. In order to quantify this effect, we adopt the realistic models D-I and D-II to calculate the EOT of interfacial layers with physical thicknesses ranging from 0.5 to 2 nm (Fig. 5.9). Overall, the resulting EOT of the interlayer is smaller than the corresponding physical thickness by 0.2–0.3 nm.

As a consequence, the effect of a thin oxide layer between a Si substrate and a high-permittivity material in metal-oxide-semiconductor devices is less severe than expected on the basis of the permittivity of bulk SiO_2. Indeed, we consider for instance a HfO_2 gate oxide with a dielectric permittivity of 21.5 and a thickness of 50 Å [126]. Assuming the interlayer to be 5 Å thick, we would find the overall permittivity of the stack to be 15.2 when setting the interlayer permittivity equal to that of bulk SiO_2, but as high as 18.0 (17.1) when adopting the data calculated for model D-I (model D-II). Analogously, considering a stack composed of $SrTiO_3$ with a dielectric permittivity of 175 and a thickness of 110 Å [127] and of a 5-Å-thick interlayer, we would obtain an overall permittivity of 60 when using the value of bulk SiO_2, but of 85 (76) when using the results for model D-I (model D-II).

Based on similar considerations, the EOT reduction of 0.2–0.3 nm with respect to bulk SiO_2 leaves some limited yet useful margin to the allowed oxide thickness in multilayer gate dielectrics. As an example, we consider the targeted 0.8 nm EOT for the 50 nm technology node. Assuming that the equivalent thickness of the high-permittivity material were as small as 0.5 nm (the smallest value reported to our knowledge for HfO_2, see Ref. [126]), the maximum allowed *physical* thickness for the interlayer would result in 0.5–0.6 nm instead of 0.3 nm.

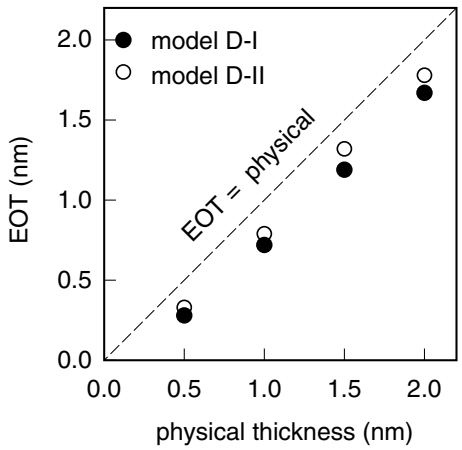

Figure 5.9: Equivalent oxide thickness vs physical thickness for the oxides in model D-I (disks) and model D-II (circles) of the Si-SiO_2 interface. For comparison, we also report the case of an oxide layer with a fixed permittivity corresponding to that of bulk vitreous silica (dashed). The EOT of ultrathin oxides is smaller than the corresponding physical thickness by 0.2–0.3 nm.

Our results carry also interesting implications in the area of thin-film metrology. Indeed, capacitance-voltage techniques for the measurements of the oxide thickness yield the *equivalent thickness* rather than the physical thickness, since they measure the capacitance of the oxide (which is proportional to d/ε_0, d being the physical thickness of the film). Therefore, the use of the bulk SiO_2 permittivity in the case of ultrathin films would lead to an *underestimation* of the measured thickness. We consider, for instance, the Si-SiO_2-HfO_2 gate stack described in Ref. [128]. On the basis of our data for model D-I (model D-II), we deduce that the reported interlayer EOT of 3.6 Å would correspond to a physical thickness of 6.4 Å (5.3 Å).

Similar considerations hold for thickness measurements based on spectroscopic ellipsometry [129]. Indeed, since ellipsometric measurements probe the *optical path* of a light beam (which is given by $\varepsilon_\infty^{1/2} d$), the determination of the film thickness must rely on some assumptions about the corresponding high-frequency permittivity. A comparison between film thicknesses measured by medium-energy ion scattering and ellipsometry shows that the latter *overestimate* the film thickness by about 0.2 nm when the enhanced screening of the interfacial oxide is not taken into account [34]. Therefore, to provide reliable ellipsometric thickness measurements in the sub-nanometer regime, it is necessary to take into account the enhanced screening of a thin interfacial layer between Si and SiO_2. This observation provides further support to our findings.

Chapter 6

Infrared spectra of ultrathin oxides on Si(100)

This chapter is devoted to the study of the transverse-optical and the longitudinal-optical infrared absorption spectra at the Si(100)-SiO_2 interface. For this purpose, we apply the formalism developed in Chap. 3 to the interface model D-III (cf. Sec. 4.2.1).

We first investigate the vibrational properties of this interface model by considering the local density of modes in the Si and SiO_2 regions (Sec. 6.1). Then, we compare the local static permittivity across the Si(100)-SiO_2 interface calculated by the method introduced in Chap. 2 and the alternative procedures proposed in Chap. 3 (Sec. 6.2). The latter method allowed us to identify the origin of the enhanced ionic screening in the substoichiometric interfacial layer (Sec. 6.2.1).

After these preliminary investigations, we turn to the analysis of the infrared spectra across the interface (Sec. 6.3). First, we study the TO and LO absorption within the SiO_2 region and compare our results with experiment. Then, we follow the evolution of the spectra across the interface. Finally, we investigate the red shift of the high-frequency peaks in the TO and LO spectra (Sec. 6.4), and we clarify the microscopic origin of this effect (Sec. 6.5).

6.1 Vibrational density of states across the Si(100)-SiO_2 interface

We evaluated the local vibrational density of states across the interface by using the analogous of Eq. (4.1) for the vibrational eigenmodes:

$$D_{\mathrm{v}}(x;\omega) = \sum_n \sum_{I\alpha} |\xi_{I\alpha}^{t,n}|^2 \, \delta(\omega - \omega_{t,n}) w(x - X_I), \tag{6.1}$$

where x indicates a coordinate along the interface normal, $\xi_{I\alpha}^{t,n}$ and $\omega_{t,n}$ are the eigenvectors and eigenfrequencies of the analytical part of the dynamical matrix,

and $w(x)$ is the spatial weight function introduced in Sec. 3.3.1. Figure 6.1 shows the evolution of the vibrational density of states across the Si(100)-SiO_2 interface as calculated for model D-III.

Within the substrate (Fig. 6.1, at a distance of 3.5 Å from the first O atom of the oxide), the spectral features of bulk Si are well reproduced. In particular, we found two transverse-acoustic peaks at 130 cm^{-1} and 190 cm^{-1}, and a longitudinal-optical peak at 480 cm^{-1}. These values compare favorably with inelastic neutron scattering experiments [130, 131] yielding ∼150, ∼200, and ∼480 cm^{-1} for the respective bands. The longitudinal-acoustic peak at ∼330 cm^{-1} and the transverse-optical peak at ∼410 cm^{-1} in the experimental density of states were not resolved in our calculations. This could be related to the approximate description of the vibrational band structure which results from the Γ-point sampling of the adopted Si(100) $\sqrt{8} \times \sqrt{8}$ repeat unit.

Within the stoichiometric oxide region (Fig. 6.1, at a distance of 8.5 Å from the Si substrate), the density of states is also in good agreement with inelastic neutron scattering experiments on vitreous silica [132, 133, 134]. The calculated peaks at 390 cm^{-1} and 830 cm^{-1} compare well with the experimentally observed peaks at ∼400 cm^{-1} and ∼820 cm^{-1}. In the high-frequency region, the splitting of T_2 modes (in-phase stretching motion of the O atoms around a Si atom) and A_1 modes (out-of-phase motion) [135] is not clearly distinguished in the calculated density of states. However, our calculations show a peak at 1130 cm^{-1} and a shoulder at 1220 cm^{-1}, which compare favorably with the A_1 and T_2 mode frequencies of ∼1090 and ∼1220 cm^{-1} in the neutron scattering data. The low-frequency peak at 140 cm^{-1} is absent in the experimental spectrum of Ref. [132] but has clearly been observed in Ref. [133], in agreement with our calculations. The calculated density of states was decomposed in terms of Si displacements and of O displacements in the reference frame associated to the Si-O-Si bridge [136]. This frame is defined by a bond rocking direction perpendicular to the Si-O-Si plane, a bond stretching axis directed from one Si atom to the other, and a bond bending axis along the bisector of the Si-O-Si angle. We found that the high-frequency band is mainly associated to the O stretching motion, the band around 800 cm^{-1} arises from the motion of Si atoms and from the vibration of O atoms along the bending directions, while the lower frequency band around 400 cm^{-1} results from O rocking and bending motion (Fig. 6.1). These findings are consistent with a previous first-principles calculation for vitreous SiO_2 [55].

The analysis of the vibrational density of states deep inside the Si and SiO_2 regions of the model Si(100)-SiO_2 interface D-III indicates that the bulk vibrational properties of the substrate and the oxide are recovered at a distance of only a few angstroms from the interface. When moving from the stoichiometric oxide towards the substrate across the interfacial layer, a few interesting features are observed (Fig. 6.1): (i) the A_1 shoulder at 1220 cm^{-1} disappears, (ii) the stretching band shifts towards lower frequencies, and (iii) the density of states in the

band around 400 cm^{-1} decreases. The disappearance of the A_1 shoulder arises from the breaking of the tetrahedral symmetry associated to the SiO_4 units of the bulk oxide. Indeed, in presence of partially oxidized Si atoms, the distinction

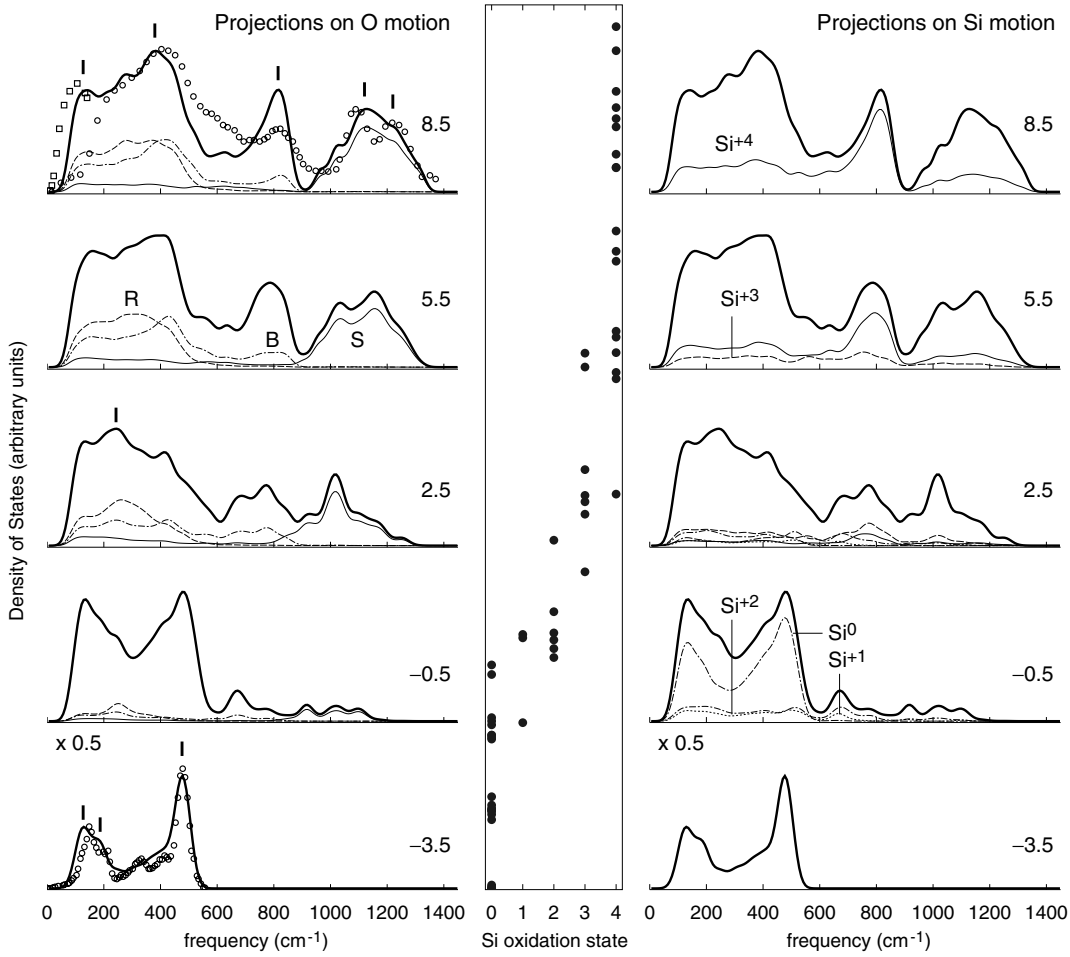

Figure 6.1: Local density of vibrational modes across model D-III of the Si(100)-SiO_2 interface (left and right panels), at various distances from the interface (indicated in Å). Full density of states are reported in both panels (bold solid). The effective neutron density of states for bulk vitreous SiO_2 are from Ref. [132] (circles) and Ref. [133] (squares). The density of states for bulk Si is from Ref. [131] (circles). Partial projections onto O (left panel) and Si (right panel) contributions are also shown: O rocking (dashed), bending (dash-dotted), and stretching (solid), and Si^{+4} (solid), Si^{+3} (dashed), Si^{+2} (dash-dotted), Si^{+1} (dotted), and Si^0 (double dash-dotted). A Gaussian broadening of 20 cm^{-1} was applied. Vertical bars indicate the spectral features discussed in the text. The central panel shows the distribution of partially oxidized Si atoms for comparison.

between A_1 and T_2 modes no longer holds and the corresponding bands merge into a single peak [137]. As it will be shown in Sec. 6.5, the softening of the stretching modes relates to the lengthening of Si-O bonds with decreasing Si oxidation state (cf. Sec. 4.2.2), and reflects the reduction of the force constants along the stretching direction as the bond length increases. The decrease of the density of states around $\sim$400 cm^{-1} is mainly due to the shift of the rocking band to lower frequencies, resulting into a peak at $\sim$250 cm^{-1} (Fig. 6.1). This effect will be shown to play a significant role in the enhancement of the static permittivity of the interfacial oxide with respect to bulk SiO_2 (cf. Sec. 6.2.1).

6.2 Local permittivity from the vibrational eigenmodes

The knowledge of the vibrational frequencies and eigenvectors allowed us to calculate the space- and frequency- dependent dielectric function of the adopted model Si(100)-SiO_2 interface, according to Eqs. (3.37)–(3.44). In view of comparing with experiment and with the approach described in Sec. 5.3.1, in the following we focus on two special cases:

(i) the frequency dispersion of the dielectric function in the middle of the oxide region (x fixed, ω varying), and

(ii) the spatial evolution of the static permittivity across the interface (ω fixed, x varying).

To obtain the frequency dispersion within the stoichiometric region of the interface model D-III, we used Eq. (3.37) together with Eqs. (3.26). The transverse diagonal component of the high-frequency permittivity $\varepsilon^{\infty}_{\alpha\alpha}(x)$ in Eq. (3.26) was evaluated approximately through the corresponding longitudinal component, following the procedure outlined in Sec. 2.1.1. The latter approximation corresponds to assuming that the microscopic layers in which the supercell can be decomposed behave isotropically, which is legitimate for the disordered oxide region which we are considering. Figure 6.2 shows a comparison between the calculated real and imaginary part of the dielectric function in the oxide of model D-III and experimental data for bulk vitreous silica [138]. The positions of the main peaks in the imaginary dispersion at about 450, 800 and 1100 cm^{-1} are well reproduced, the largest deviation from the experimental peak positions being $\sim$20 cm^{-1}. More significant is the deviation for the shoulder at around 1200 cm^{-1}, consistently with previous calculations on bulk SiO_2 [55].

The relative intensities of the peaks are also in good agreement with experiment, even though the absolute intensities are clearly underestimated (Fig. 6.2). This effect relates to the larger width of the theoretical peaks with respects to their experimental counterparts. Indeed, focusing on the high-frequency band,

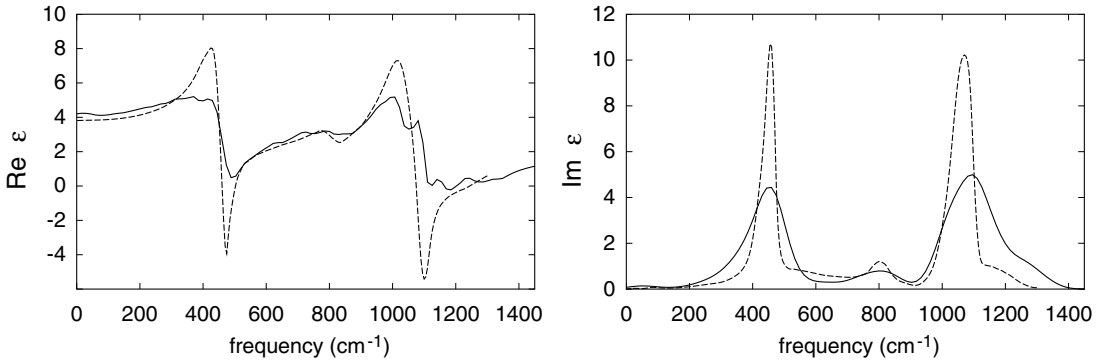

Figure 6.2: Real (left) and imaginary (right) part of the dielectric function within the oxide region of the Si(100)-SiO_2 interface model D-III (solid). Dashed lines indicate the experimental dispersions for bulk vitreous silica [138].

the width calculated through the *unbroadened* spectrum ($\sim$270 cm^{-1}) overestimates the experimental width ($\sim$110 cm^{-1}) [138]. Since the broadening of the infrared peaks in vitreous SiO_2 mainly results from the distributions of the structural parameters of the oxide [41], the overestimation of the experimental widths indicates that the distributions of bond lengths and bond angles in the model oxide considered (cf. Sec. 4.2.2) are broader than in experiment. The latter effect relates to the finite size of the computational cell adopted, which inhibits the full structural relaxation of the amorphous oxide. The same considerations apply to the real part of the dielectric function (Fig. 6.2), which provides in addition the static permittivity of the oxide $\varepsilon^0_{SiO_2} = 4.2$. The latter value is in agreement with the permittivities calculated in Sec. 5.3.1 for model D-I and model D-II of the Si(100)-SiO_2 interface.

Next, we consider the spatial evolution of the static permittivity across model D-III of the Si(100)-SiO_2 interface. This can be determined by setting $\omega = 0$ in Eqs. (3.37)–(3.44), or alternatively by applying a finite electric field as already done in Sec. 5.3.1. In particular, by fixing α along the longitudinal direction and β along a transverse direction, we can calculate:

(E1) $\varepsilon^0_{\alpha\alpha}(x)$ from the transverse dynamical matrix through Eq. 3.44,

(E2) $\varepsilon^0_{\alpha\alpha}(x)$ from the longitudinal dynamical matrix through Eq. 3.38,

(E3) $\varepsilon^0_{\alpha\alpha}(x)$ through the finite field method of Sec. 2.1.1, and

(E4) $\varepsilon^0_{\beta\beta}(x)$ from the transverse dynamical matrix through Eq. 3.37.

The cases (E1) and (E2) are compared in Fig. 6.3(a). Despite the rather different procedures, there is a very good agreement between the two curves. The small differences likely arise from the different way the convergence errors on the dynamical charges, the eigenfrequencies and the eigenmodes are combined within

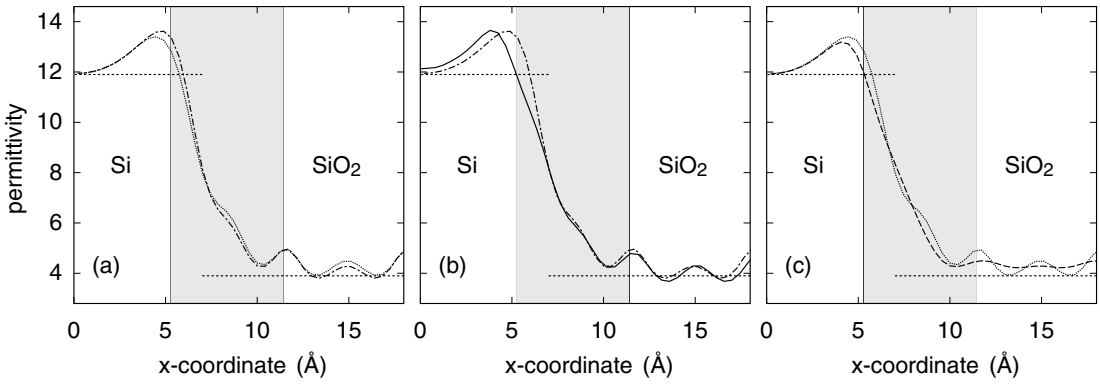

Figure 6.3: Local static permittivity across model D-III of the Si(100)-SiO_2 interface, calculated according to various procedures: (a) $\varepsilon^0_{\alpha\alpha}(x)$ from the transverse dynamical matrix [dotted, (E1)] vs. $\varepsilon^0_{\alpha\alpha}(x)$ from the longitudinal dynamical matrix [dash-dotted, (E2)]. (b) $\varepsilon^0_{\alpha\alpha}(x)$ from the longitudinal dynamical matrix [dash-dotted, (E2)] vs. $\varepsilon^0_{\alpha\alpha}(x)$ from the finite field method [solid, (E3)]. (c) $\varepsilon^0_{\alpha\alpha}(x)$ from the transverse dynamical matrix [dotted, (E1)] vs. $\varepsilon^0_{\beta\beta}(x)$ from the transverse dynamical matrix [dashed, (E4)]. α is along the longitudinal direction, β along a transverse direction. The horizontal dashed lines indicate the experimental static permittivities of Si and SiO_2. The shaded region indicates the suboxide. The curves in (a), (b) and (c) are obtained by using a Gaussian spatial weight with a standard deviation of 1 Å, in order to be consistent with the choice made in Chap. 5.

the final expressions Eqs. (3.44) and (3.38).

The cases (E2) and (E3) are compared in Fig. 6.3(b). Within the oxide, there is a very good agreement between the profiles calculated through the vibrational modes or through the finite electric field method. Within the Si region, the curve (E3) overestimates the permittivity due to the limited convergence of the supercell polarization (cf. 2.2.2). The difference between the curves (E2) and (E3) around $x = 5$ Å arise from the different ways the Gaussian functions replacing the ionic point charges enter the final expressions Eqs. (2.8) and (3.38).

Figure 6.3(c) shows a comparison between the cases (E1) and (E4), corresponding to the longitudinal and transverse components of the static permittivity. The Si and the SiO_2 regions show an isotropic behavior as expected. Interestingly, also the suboxide is rather isotropic.

6.2.1 Origin of the enhanced ionic screening in the suboxide

In Sec. 5.2.1 we have shown that the suboxide carries an ionic contribution to the permittivity larger than that of the bulk oxide. Furthermore, in Sec. 5.2.2 we have

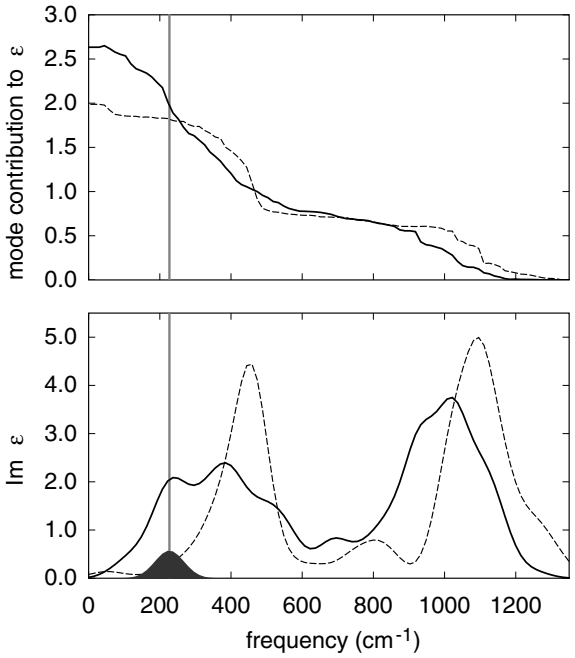

Figure 6.4: Upper panel: mode contribution $C(x;\omega)$ to the static permittivity, evaluated within the suboxide region (solid) and the stoichiometric oxide (dashed) for model D-III of the Si(100)-SiO_2 interface. Lower panel: imaginary part of the dielectric function vs frequency, for the suboxide (solid) and the pure oxide (dashed). The shaded region indicates the contribution of $Si^{+2}O_2$ structural units, giving rise to the peak at $\sim$230 cm^{-1}. In proximity of this resonance (vertical line), the mode contribution of the suboxide starts exceeding that of SiO_2.

found that the Si-centered polarizable unit with the largest ionic polarizability corresponds to the Si^{+2} oxidation state. Now, by considering the contributions of the vibrational eigenmodes to the local permittivity in the suboxide and in the oxide regions separately, we are able to identify the origin of these effects. For this purpose, we introduce the mode contribution to the static permittivity:

$$C(x;\omega) = \frac{4\pi}{\Omega} \sum_{IJ,\beta\gamma,n} \frac{Z^{\mathrm{B}}_{I,\alpha\beta}\xi^{t,n}_{I\beta}}{\sqrt{m_I}} \frac{Z^{\mathrm{B}}_{J,\alpha\gamma}\xi^{t,n}_{J\gamma}}{\sqrt{m_J}} \frac{1}{\omega^2_{t,n}} w(x - X_I)\theta(\omega_{t,n} - \omega), \tag{6.2}$$

where $\theta(\omega)$ stands for the Heavyside function. $C(x;\omega)$ defined by Eq. (6.2) gives the local contribution to the *static* permittivity arising from the eigenmodes with $\omega_{t,n} > \omega$, as can be verified by considering Eq. (3.26). In particular, we have $C(x;\omega = 0) = \varepsilon^0_{\alpha\alpha}(x)$. Figure 6.4 shows the mode contribution to the static permittivity calculated for the oxide and for the suboxide regions of model interface D-III, together with the corresponding imaginary dielectric functions. It is clear that the high-frequency modes are not involved in the enhanced ionic screening of the suboxide, and that the extra screening (from 2.0 to 2.6) arises from a suboxide peak around 230 cm^{-1}. Indeed, when the modes between 220 and 240 cm^{-1} are forced to be silent in Eq. (6.2), the suboxide ionic permittivity drops to the value calculated for the oxide. By looking at the atomic displacements corresponding to these modes within the suboxide, we further discovered that the main contribution to the extra screening arises from Si^{+2} atoms and their O nearest neighbors, with the motion of the latter mainly along rocking and bending directions (cf. Sec. 6.1). Correspondingly, when the the imaginary part of the

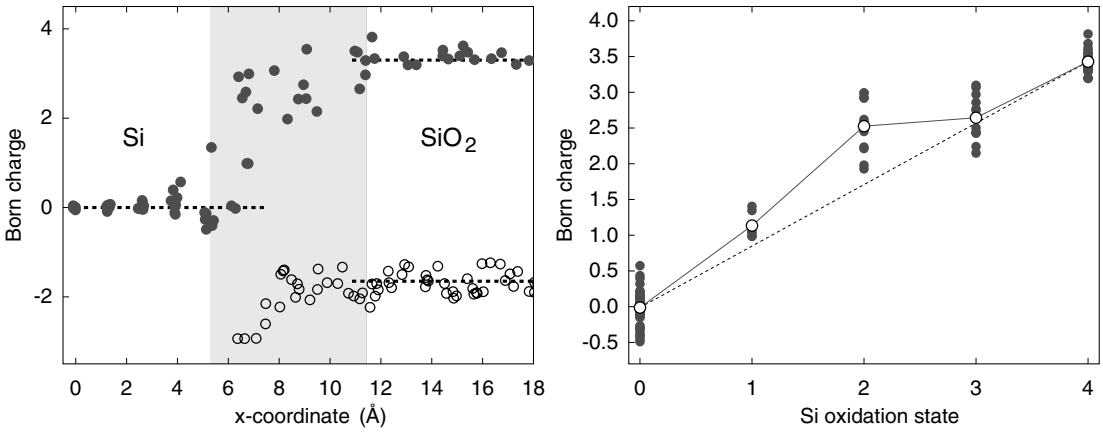

Figure 6.5: Left: Average diagonal components of the Born charges along the transverse directions for model D-III of the Si(100)-SiO_2 interface, plotted vs the atomic coordinate in the longitudinal direction. Disks (circles) correspond to Si (O) atoms. The horizontal dashed lines indicate the effective charges calculated within the silicon and the oxide region of the crystalline interface models C-I and C-II (Fig. 5.5). Right: Born charges in model D-III vs Si oxidation state (disks), together with their average values (circles). The solid line is a guide to the eye. The dashed line corresponds to an ideal linear dependence as determined by scaling the average charge of Si^{+4} atoms according to the oxidation state. The only significant deviation from the linear behavior correspond to Si^{+2} species.

permittivity is recalculated by including the sole contributions of Si^{+2} atoms and of their nearest neighbor O atoms, a distinct peak around 230 cm^{-1} is found (Fig. 6.4, shaded area).

This finding is consistent with the large ionic polarizability of Si^{+2} polarizable units calculated for the crystalline model structures C-I and C-II (Sec. 5.2.2). The large polarizability of the $Si^{+2}O_2$ structural units is a consequence of both the large dynamical charges of Si^{+2} atoms (Fig. 6.5), and the small associated vibrational frequency of 230 cm^{-1} (to be compared with 450 cm^{-1} for the corresponding SiO_2 modes). The large dynamical charges of the Si^{+2} atoms are consistent with the results of Sec. 5.2.2 for the crystalline model interfaces C-I and C-II (Fig. 5.5), indicating that this behavior does not relate to the specific structural arrangement, and must be a general feature of Si^{+2} species in silicon suboxides.

6.3 Infrared absorption across the Si(100)-SiO_2 interface

In this section we describe the *local* infrared absorption spectra across model D-III of the Si(100)-SiO_2 interface, calculated according to Eqs. (3.28) and (3.34).

Since the adopted superlattice structure consists of two Si-SiO_2 interfaces connected back-to-back, we here discuss the infrared response which results from taking the average of the local spectra calculated separately for each interface. This choice virtually corresponds to studying a model structure with one single interface and twice the supercell transverse area, and results in a larger sampling of the possible bonding configurations of the disordered oxide.

Figure 6.6 shows the calculated TO and LO infrared absorption spectra across our model interface, at various distances from the Si substrate. At a distance of 8–9 Å from the substrate, the absorption spectra closely match those of bulk vitreous silica (bold curves in Fig. 6.6). Indeed, the calculated positions of the main TO absorption peaks, 457, 810, and 1097 cm^{-1}, are in excellent agreement with the corresponding experimental peaks at 457, 810, and 1076 cm^{-1} [41], and with previous calculations on bulk disordered SiO_2 giving 453, 861, and 1106 cm^{-1}

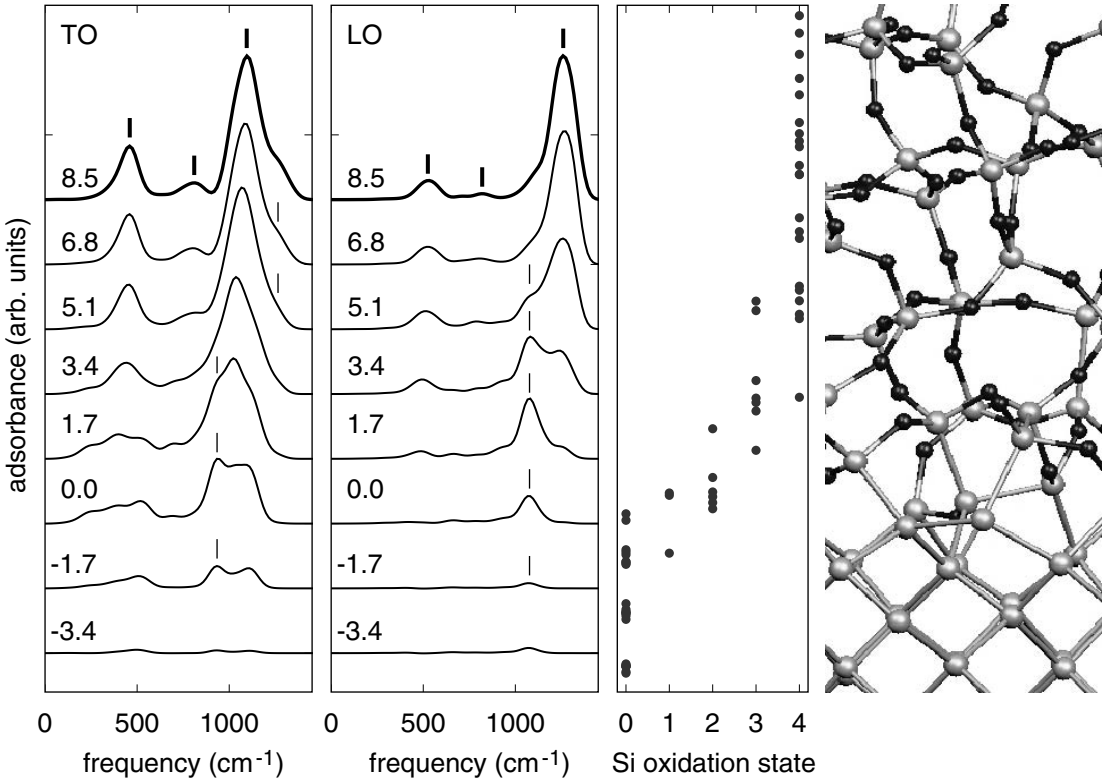

Figure 6.6: Local TO (first panel from the left) and LO (second panel) infrared absorption spectra calculated at various distances from the Si substrate, for model D-III of the Si(100)-SiO_2 interface. The distances are indicated in Å and refer to the first O atom of the oxide. The principal spectral features are highlighted. The third panel from the left shows the distribution of the various oxidation states of Si across the interface, and the last panel is a ball-and-stick representation of the D-III model interface.

[55]. Similarly, the calculated positions of the main LO peaks, 529, 820, and 1260 cm^{-1}, are also in excellent agreement with the corresponding experimental peaks at 507, 820, and 1256 cm^{-1} [41].

We focus hereafter on the high-frequency peaks, for which an extensive set of experimental data is available [42, 43, 44, 45, 46, 47, 48, 49]. As the distance from the Si substrate decreases, two shoulders develop around 939 and 1077 cm^{-1} in the TO and LO spectra, respectively (Fig. 6.6). In this region, the oxide is slightly oxygen-deficient and Si^{+2}, Si^{+3} species occur. In the vicinity of the substrate, these shoulders become the principal peaks. The corresponding oxide is highly oxygen-deficient, containing Si^{+1} and Si^{+2} species. Within the silicon substrate, the infrared activity is suppressed as the dynamical charges of Si atoms vanish (Fig. 6.5).

By inspection of the spectra in Fig. 6.6, we observe that a stretching peak with a frequency close to that of bulk SiO_2 persists in the TO spectrum even close to the substrate. This effect relates to a Si–O–Si bridge with rather small bond-lengths (1.61 Å), leading to higher vibrational frequencies (cf. Sec. 6.5). Since the corresponding Si-O bonds are oriented almost parallel to the interface plane, their stretching motion produces a negligible contribution to the LO absorption intensity.

The largest calculated redshift of the absorption peaks are 158 cm^{-1} for the high-frequency peak of the TO spectrum, and 183 cm^{-1} for the corresponding peak in the LO spectrum. Since these values refer to the *local* absorption, they cannot be compared directly to experiments on the Si-SiO_2 interface, which address the overall behavior of a structure with a strong chemical grading. Nonetheless, these data can be confronted with experiments on bulk substoichiometric silica (SiO_x). While for the LO spectrum there are no experimental data available to our knowledge, for the high-frequency region of the TO spectrum several

Table 6.1: Comparison between the calculated frequencies of the stretching peaks in the *local* infrared absorption spectra of the pure oxide (SiO_2) and the suboxide (SiO_x) regions of model interface D-III and the experimental values corresponding to bulk stoichiometric and substoichiometric silica. The experimental TO and LO peak frequencies for bulk silica are taken from Ref. [41], the TO data for the substoichiometric oxide are from Ref. [137] ($x < 0.1$) and Ref. [140] ($x = 0.1$), respectively. No experimental data are available to our knowledge for the LO spectrum of the substoichiometric oxide. All frequencies are in cm^{-1}.

	TO		LO	
	SiO_2	SiO_x	SiO_2	SiO_x
Expt.	1076	945,960	1256	–
Calc.	1097	939	1260	1077

investigations reported peak frequencies within the range 940–987 cm^{-1} for SiO_x with low O content [137, 139, 140, 141]. In particular, TO peak frequencies for suboxides SiO_x with $x \leq 0.1$ were observed within the range 945–960 cm^{-1}. Furthermore, a recent study of ultrathin SiO_2 layers on Si(100) recorded a shoulder at 980 cm^{-1}, and proposed the assignment of this feature to a substoichiometric interfacial layer [42]. Our calculated TO peak at 939 cm^{-1} is therefore in agreement with experimental data on substoichiometric silica with $x \leq 0.1$, and supports the assignment [42] of the shoulder at 980 cm^{-1} to the suboxide layer. Table 6.1 summarizes the main results.

6.4 Red shift of the stretching TO and LO peaks

To make a direct comparison with measured red shifts of the TO and LO peaks at Si(100)-SiO_2 interfaces, it is necessary to determine the *total* infrared absorption spectra corresponding to interfaces with varying oxide thicknesses. For this purpose, we determined the infrared spectrum for a given oxide thickness by integrating the density of absorption functions Eqs. (3.28) and (3.34) through Eq. (3.36). To cover a range of thicknesses extending up to 100 Å, the local contributions for distances from the Si substrate larger than 8.5 Å were taken from the local TO and LO spectra at 8.5 Å, which well reproduce the infrared response

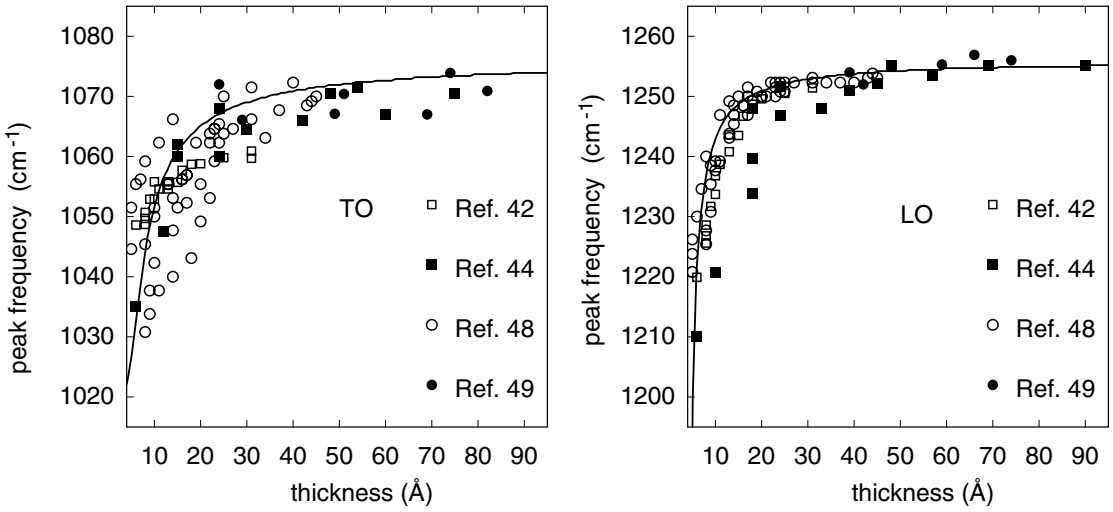

Figure 6.7: Position of the high-frequency TO (left) and LO (right) peaks of the Si(100)-SiO_2 interface vs oxide thickness (solid). The broadening of the spectra was performed by means of a Gaussian function with a standard deviation of 80 cm^{-1} in order to merge the high-frequency spectral features into a single peak. Experimental data are taken from the indicated references. To facilitate the comparison, the theoretical frequencies were rescaled to match the experimental peaks of bulk SiO_2 in the limit of thick oxides.

of bulk SiO_2 (Sec. 6.3).

From the spectra obtained in this way, we derived the positions of the high-frequency TO and LO peaks as a function of oxide thickness (Fig. 6.7). For this purpose, we assigned a single peak position to the high-frequency part of the spectra applying a suitable broadening to the high frequency band. With respect to the *local* spectra, the largest redshifts of the *total* absorption peaks are markedly reduced, and amount to $\sim$50 cm^{-1} for both the TO and the LO peaks, in agreement with experiment [44, 46]. The spread of the measured peak positions arise from the different compositions of the interfacial layers obtained by various preparation methods [42, 44, 46, 48, 49]. Our results account well for the observed trend in the experimental data (Fig. 6.7), clearly indicating that the origin of TO and LO red shifts in ultrathin oxide films on Si(100) resides in the softer vibrational modes of the substoichiometric interfacial layer.

6.5 Microscopic origin of the mode softening in the suboxide

In this section, we clarify the softening of the frequencies in the interfacial layer, by establishing a relation between the position of the high-frequency peak and the local bonding configuration.

For each Si-O bond, we re-calculated the infrared spectrum after projecting the vibrational eigenmodes on the corresponding Si-O stretching motion, and then identified the position of the high-frequency peak. In this way, we established a relation between a given Si-O bond and the frequency of its main contribution to the infrared spectrum ("principal frequency" from now on, Fig. 6.8). In order to identify the structural parameters which affect the position of the principal infrared peak, we analysed the role of the Si-O-Si bond angle [(Fig. 6.9(a)], the Si oxidation state [(Fig. 6.9(b)], and the Si-O bond length (Fig. 6.10).

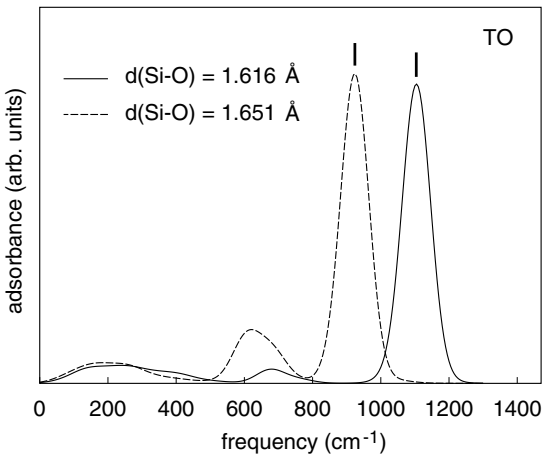

Figure 6.8: Transverse absorption spectra for model D-III of the Si(100)-SiO_2 interface calculated by projecting the eigenmodes on the stretching direction of a single Si-O bond. The spectra shown here correspond to Si-O bonds with bond lengths of 1.616 Å (solid) and 1.651 Å (dashed), respectively. The principal frequencies associated to these spectra are indicated by vertical bars and correspond to 1104 cm^{-1} and 924 cm^{-1}, respectively.

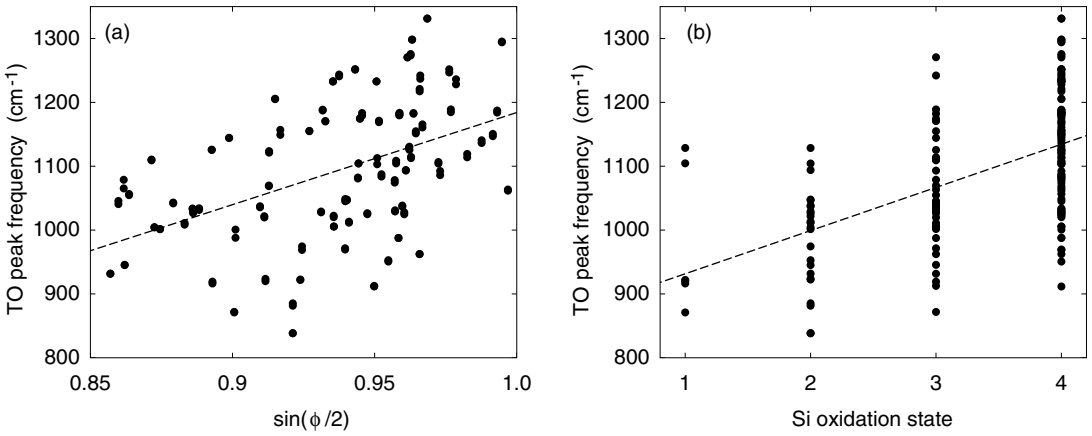

Figure 6.9: Principal TO stretching frequencies associated to individual Si-O bonds (a) vs Si-O-Si angle ϕ, and (b) vs Si oxidation state. Linear regressions (dashed) give frequency shifts of $\sim$3 cm^{-1} for a bond angle increase of 1°, and of 68 cm^{-1} for an oxidation state increase of one unit.

According to previous suggestions based on a simplified model for the vibrational eigenmodes of tetrahedral glasses [46, 142], the Si-O-Si angle ϕ should play the major role in determining the peak frequency, and would be related to the latter by $\omega \propto \sin(\phi/2)$ [143, 144]. However, Fig. 6.9 shows that only a poor correlation exists between the principal frequency and the Si-O-Si angle. Indeed, we obtained the rather small correlation coefficient r^2=0.22 for the corresponding data set. Similarly, a poor correlation exists between the principal frequency and

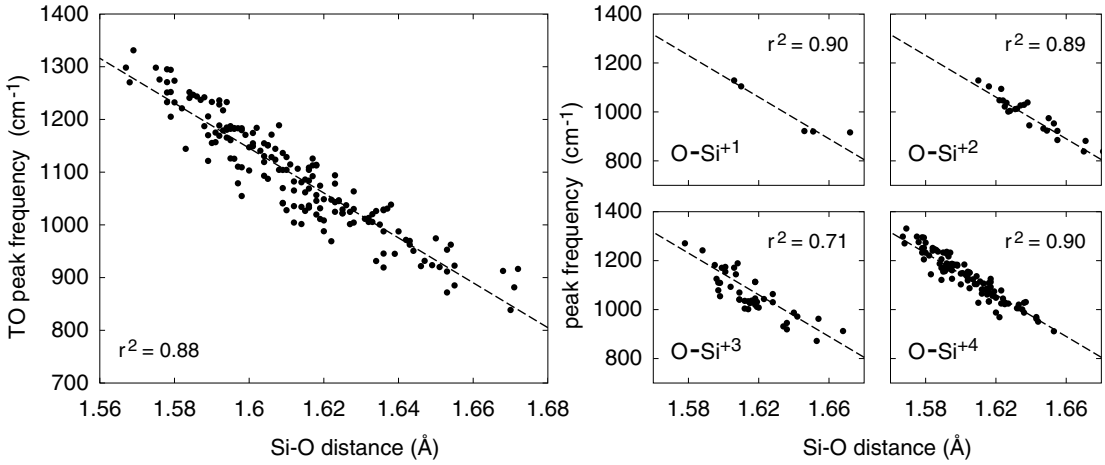

Figure 6.10: Principal TO stretching frequencies associated to individual Si-O bonds plotted against their bond length (left). A linear regression (dashed) gives a red shift of 43 cm^{-1} for a bond length increase of 0.01 Å. The small panels on the right display the frequency vs bond length for each Si oxidation state considered separately. The correlation coefficients are indicated for each case.

the Si oxidation state [r^2=0.28, Fig. 6.9(b)].

At variance, we found a distinct correlation between the principal frequency and the Si-O bond length (Fig. 6.10), corresponding to the large correlation coefficient $r^2 = 0.88$. Interestingly, the latter correlation holds *separately* for every Si oxidation state (Fig. 6.10), indicating that the Si-O bond length plays the major role in the determination of the infrared stretching peaks.

Once the relation between the infrared peak frequencies and the Si-O bond length established, it is possible to identify the origin of the observed red shifts of the infrared stretching peaks at the Si(100)-SiO_2 interface. Indeed, we know that the average bond length in the substoichiometric oxide is larger than in bulk SiO_2 (Sec. 4.2.2). Based on the frequency-bond length correlation, this must correspond to softer stretching frequencies in the suboxide layer. Hence, our analysis allows us to assign the *microscopic origin* of the observed red shifts at the Si(100)-SiO_2 interface to the *lengthening* of the Si-O bonds in the suboxide.

Similar conclusions can be reached by considering the vibrational frequencies of O atoms alone, i.e. the frequencies at which a given O atom would oscillate if all other atoms were kept frozen. The reason for considering only O atoms is that, within the suboxide region, the main contribution to the infrared intensity is found to arise from the O motion. These "effective frequencies" are obtained by diagonalizing the submatrices $C_{II}^{\alpha\beta}$ of the dynamical matrix (with I referring to an O atom) and provide a qualitative estimate of the effect of the local environment on the vibrational properties of the considered atom. The calculated effective frequencies $\omega_{I\gamma}^{\mathrm{eff}}$ ($\gamma = 1, 2, 3$) cluster into three groups, corresponding to O stretching, bending and rocking motions in the local reference frame defined by the Si-O-Si bridge. Focusing on the effective stretching frequency, we found again a strong correlation with the Si-O bond length, but only a weak correlation

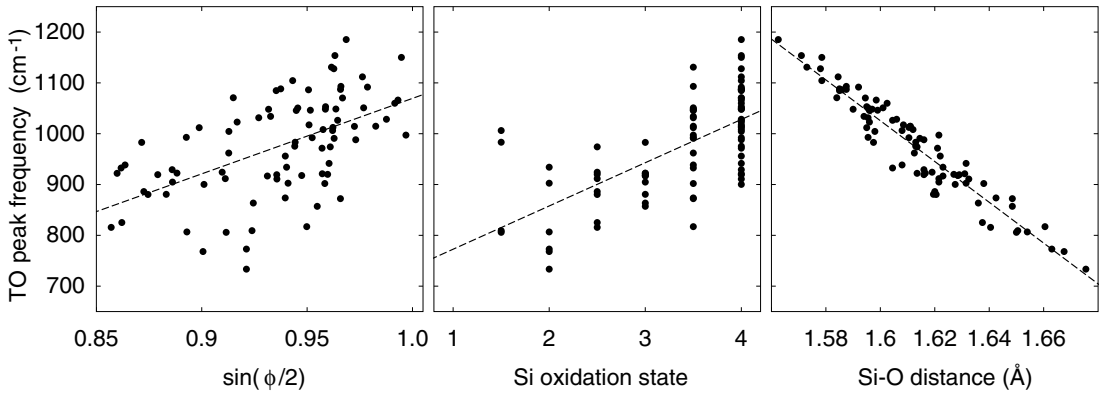

Figure 6.11: Effective O stretching frequencies plotted against the Si-O-Si angle ϕ (left), the average Si oxidation state (middle), and the average Si-O bond length (right). Linear regressions (dashed) give frequency shifts of $\sim$3 cm^{-1} for a bond angle increase of 1°, of 85 cm^{-1} for an oxidation state increase of one unit, and of 40 cm^{-1} for a bond length decrease of 0.01 Å.

with the Si-O-Si angle and the Si oxidation number (Fig. 6.11), in agreement with the previous analysis based on the selective projection of eigenmodes. It should be noted that the *effective* frequencies underestimate the corresponding *principal* frequencies. This effect arises because the effective frequency does not account for the coupling with neighboring Si atoms, which would induce a blue shift of the stretching band. This is most readily seen by considering a diatomic linear chain with a basis of Si and O atoms [145]: the relative shift induced by the mode coupling is $[(1 + m_{\mathrm{O}}/m_{\mathrm{Si}})^{1/2} - 1] \simeq 0.25$ and corresponds to $\sim$175–300 cm^{-1} for the range of effective O stretching frequencies 700–1200 cm^{-1}. This simple estimate is comparable to the frequency shift of $\sim$120 cm^{-1} observed between Figs. 6.9–6.10 and Fig. 6.11.

The dependence of the effective stretching frequencies of the O atoms on the Si-O bond length is also at the origin of the softening of the stretching band which is observed in the local vibrational density of states when approaching the Si substrate (cf. Sec. 6.1).

Chapter 7

Summary and conclusions

7.1 Summary

In this thesis, we investigated the permittivity (both high-frequency and static) and the infrared absorption at the Si(100)-SiO_2 interface.

We first developed a method for investigating atomic scale permittivity profiles across interfaces between insulators (Chap. 2). An expression for the local permittivity was derived from the microscopic polarization induced by an applied electric field (Sec. 2.1). We showed that the permittivity can conveniently be analysed in terms of maximally localized Wannier functions (Sec. 2.1.2). In this way, variations of the local permittivity can be associated to specific features of the bonding arrangement, such as for instance elongated bonds and first-neighbor shells. In our scheme, the difficulties related to the treatment of the nonlocality of the microscopic dielectric function were overcome by focusing on a dielectric response which is diagonal in real space. This was achieved at the cost of restricting the description to length scales which are of the order of interatomic distances. We generally found that such a local description is meaningful for length scales exceeding the spread of the maximally localized Wannier functions (Appendix A).

This method was applied to the interface between Si and SiO_2 (Chap. 5). Using several different interface models (Chap. 4), we found that the dielectric transition from Si to SiO_2 is rather abrupt, occurring over a width of a few angstroms (Secs. 5.2.1 and 5.3.1). We found that the effective polarizability associated to intermediate oxidation states of Si is enhanced with respect to the bulk oxide (Sec. 5.2.2), leading to a larger permittivity of the interfacial suboxide layer. In order to quantify the permittivity enhancement within the interfacial layer, we calculated the equivalent oxide thickness (EOT) of oxides with physical thicknesses ranging from 0.5 to 2 nm using realistic interface models (Sec. 5.3.2). We found that the EOT of the interlayer is smaller than the corresponding physical thickness by 0.2–0.3 nm. This results has beneficial implications for the scaling of

CMOS devices, since it indicates that the increase of the EOT of a gate dielectric stack due to an interfacial oxide layer is smaller than expected on the basis of the permittivity of bulk SiO_2.

In order to address the infrared absorption at the Si(100)-SiO_2 interface, we developed a general scheme for calculating both the transverse-optical and the longitudinal-optical infrared absorption spectra at surfaces and interfaces (Chap. 3). This scheme is based on the observation that, for systems such as surfaces and interfaces, the Maxwell boundary conditions result into TO and LO infrared dipoles oriented parallel and normal to the interface plane, respectively (Sec. 3.1). While the TO absorption intensity can be expressed in terms of the usual lattice dielectric function, the calculation of the LO absorption requires the inversion of the latter, and poses numerical difficulties. These difficulties were effectively overcome by adopting dielectric response functions defined with respect to the external electric field rather than to the internal selfconsistent electric field (Sec. 3.2.2). This choice eventually led to highly symmetric expressions for the TO and LO absorption functions. By resorting to the notion of local induced dipoles introduced in Sec. 2.1.3, we further derived a local decomposition of the infrared spectra in terms of the absorption of atomically thin slabs (Sec. 3.3), and we established the connection with the theory developed in Chap. 2 (Sec. 3.4).

This method was applied to the Si(100)-SiO_2 interface by adopting a realistic structural model of the interface (Chap. 6). The calculated local infrared spectra within the stoichiometric SiO_2 region were found in good agreement with the experimental TO and LO absorption of bulk vitreous silica. In addition, our calculations reproduced the observed red shift of the Si-O stretching peaks with decreasing oxide thickness (Sec. 6.3). By projecting the infrared-active modes onto localized stretching vibrations of neighboring Si and O atoms, we were able to establish a relation between the length of the Si-O bond and the frequency of the corresponding contribution to the infrared spectra. We found that a strong correlation exists between the bond lengths and the frequencies of the stretching peak, longer bonds resulting into softer modes. This finding allowed us to assign the microscopic origin of the red shifts of the high-frequency peaks in the infrared spectra of ultrathin oxide films on Si(100) to the lengthening of the Si-O bonds in proximity of the substrate (Sec. 6.5).

7.2 Conclusions

It is by now clear that the semiconductor technology has come to a point where experimental probes are no longer able to accurately describe the physical properties of interest without the support of atomic-scale quantum-mechanical modelling. Indeed, most spectroscopic techniques, such as for instance X-ray and Auger photoemission, infrared absorption, and ellipsometry, are sensitive to physical properties which result from a complex interplay of several factors, and this

poses serious difficulties to the interpretation of the measurements.

The determination of film thicknesses of ultrathin oxides on semiconducting substrates exemplifies these difficulties. Indeed, we have seen that the knowledge of the dielectric function of the material under investigation is crucial for the interpretation of capacitance-voltage measurements or ellipsometric spectra. As a consequence, the film thickness determined by means of the above techniques are necessarily dependent on the model assumed for the dielectric response. While this did not represent an issue when films with thicknesses in the range of hundreds of nanometers were studied, we are nowadays realizing that many challenging problems emerge when objects with physical dimensions around the nanometer are being considered.

A very similar problem is encountered in the study of the infrared spectra of ultrathin oxide films. We have seen that when classical models, established for bulk materials, are applied to the interpretation of the infrared spectra of the corresponding ultrathin oxides, the evaluation of similar experimental results can lead to conclusions in contrast with each other. This happens, for instance, when different phenomena show features in the measured spectra which are so similar that it is hard to distinguish between them without additional information.

As this work attempted to demonstrate for the interface between silicon and its oxide, a promising strategy to overcome such difficulties consists of *combining atomic-scale experimental probes with atomic-scale theoretical investigations*. For this goal to be achieved, theory must be complementary to experiment, and not subordinated to. It is precisely in the latter requirement that we recognize the importance of first principles methods for the future advancement of semiconductor technology.

Along this work we investigated the infrared properties of the interface between silicon and its oxide, a physical problem which is deeply routed in the silicon technology area. It is interesting to note, however, that such an "applied" problem stimulated the reflection on a wealth of basic theoretical issues. Indeed, in order to achieve our goal, we first needed to answer the very general question on how to calculate from first principles infrared properties at interfaces (including surfaces as a particular case). This was not obvious at the beginning, since the literature mostly focuses on bulk systems relying on reciprocal space approaches and symmetry considerations, while what we needed was a real-space method for systems where the bulk symmetry is broken by the occurrence of the interface. The main ideas developed throughout this thesis were based on the observation that it appears possible to define a "local" dielectric function, which can be calculated with a significantly lower computational effort than the fully nonlocal dielectric function. The length scale over which such a local description makes sense was found to be of the order of the interatomic distances, and appears to be related to the spread of the maximally localized Wannier functions of the system. The latter connection suggests a deeper relation between the real-space localiza-

tion of the dielectric matrix and the corresponding localization of the many-body electronic wavefunction, and certainly deserves further investigation.

A particular role was played within this work by the maximally localized Wannier functions. Their connection to the electronic dielectric response of the film appears to go well beyond the relation between their centers and the Berry-phase polarization of the system as established by the modern theory of polarization. Indeed, as we have shown, they allow to identify the dielectric response of single atomic bonds, holding promise for an unprecedented understanding of the dielectric properties at the single-atom level. An interesting application of the Wannier decomposition of the dielectric response would consist of validating the bond polarizability models commonly adopted for covalently bonded materials. Indeed, the parameters entering these models could be derived directly from first principles through the Wannier polarizabilities introduced within the present work. Such approach would avoid to resort to parameter-fitting procedures, rendering the classical models more reliable.

Other possible applications of our local dielectric function can be envisaged. We think in particular to the quasiparticle self-energy corrections to the electronic excitation energies. Indeed, density functional band gaps can be corrected by using the electronic dielectric function. This suggests that our local permittivity could be used to determine a local correction to the quasiparticle band gaps. Such a correction would be especially valuable for semiconductor heterojunctions and in general for systems where the reduced symmetry or dimensionality leads to modifications of the bulk band structure.

Certainly much work is still needed to develop these ideas. In the mean time, we hope that the methods introduced along the present work could serve as a basis for further studies of the dielectric and infrared properties of surfaces and interfaces.

Appendix A

Nonlocality and Wannier function spread

In this Appendix, we relate the typical decay length of the homogeneous real-space dielectric function [146] to the spread of the maximally localized Wannier functions. To this end, we sequentially make use of expressions relating the decay length to the dielectric constant, the dielectric constant to the band gap, and finally the band gap to the Wannier spread.

Within the Thomas-Fermi approximation, the homogeneous dielectric function in Fourier space can be expressed as [146]:

$$\varepsilon(k) = 1 + \frac{\varepsilon_{\mathrm{m}} - \sin(kR)/(kR)}{\sin(kR)/(kR) + (\lambda k)^2}, \tag{A.1}$$

where R is the screening radius [146], $\varepsilon_{\mathrm{m}} \equiv \varepsilon(k=0)$ is the macroscopic dielectric permittivity, and

$$\lambda^2 \equiv \frac{\pi^2 \hbar^2 \varepsilon_{\mathrm{m}}}{4\pi e^2 m k_{\mathrm{F}}}, \tag{A.2}$$

with k_{F} indicating the valence Fermi momentum, and m the electron mass. Instead of Eq. (A.1), we here consider an approximate expression for $\varepsilon(k)$,

$$\varepsilon(k) \simeq 1 + \frac{\varepsilon_{\mathrm{m}} - 1}{1 + (\lambda k)^2}, \tag{A.3}$$

which leaves its shape essentially unchanged and retains the correct limiting behavior at both small and large k. For the parameters adopted in Ref. [146], corresponding to silicon, germanium, and diamond respectively, we checked numerically that the dielectric functions obtained by using Eq. (A.1) and Eq. (A.3) differ by at most 20% over the full range of k. The Fourier transform of the $\varepsilon(k)$ defined by Eq. (A.3) is obtained analytically and gives the nonlocal dielectric function

$$\varepsilon(\mathbf{r}, \mathbf{r}') = \delta(\mathbf{r}, \mathbf{r}') + \frac{\varepsilon_{\mathrm{m}} - 1}{4\pi\lambda^3} \frac{\exp(-|\mathbf{r} - \mathbf{r}'|/\lambda)}{|\mathbf{r} - \mathbf{r}'|/\lambda}, \tag{A.4}$$

where $\delta(\mathbf{r}, \mathbf{r}')$ indicates a Dirac delta normalized to unity. Eq. (A.4) clearly defines a decay length λ for the extent of nonlocality effects in the dielectric function.

The dielectric permittivity ε_{m} can be related to the optical properties of the system through the Penn model [147]:

$$\varepsilon_{\mathrm{m}} = 1 + \Big(\frac{\hbar\omega_{\mathrm{p}}}{E_{\mathrm{P}}}\Big)^2, \tag{A.5}$$

where E_{P} is the Penn gap [148] and ω_{p} is the plasma frequency of the electrons:

$$\omega_{\mathrm{p}}^2 = \frac{4\pi e^2}{3\pi^2 m} k_{\mathrm{F}}^3. \tag{A.6}$$

Since we are interested in estimating order of magnitudes, we replace E_{P} with the direct band gap E_{g} and neglect the first term on the right hand side of Eq. (A.5), obtaining

$$\varepsilon_{\mathrm{m}} \approx \Big(\frac{\hbar\omega_{\mathrm{p}}}{E_{\mathrm{g}}}\Big)^2. \tag{A.7}$$

Finally, it has been shown that there exists a relation between the direct band gap and the spread ξ of the Wannier functions maximally localized along a given direction [64, 149]:

$$\xi^2 < \frac{\hbar^2}{2mE_{\mathrm{g}}}. \tag{A.8}$$

By combining the equations above, we obtain the relation

$$\lambda r_0 > (2\pi\sqrt{3})^{1/3}\, \xi^2 \simeq 2\,\xi^2, \tag{A.9}$$

where r_0 corresponds to the radius of the sphere occupied on average by one electron and constitutes a measure of the valence electron density. This equation provides a relation between the decay length of nonlocality effects λ and the Wannier spread ξ. When $r_0 \sim \xi$, as is the case in the systems considered in this work, relation (A.9) indicates that a local description of the dielectric properties can only be achieved on length scales which exceed the Wannier spread ξ.

Appendix B

Real-space average with Gaussian kernel

In this Appendix, we establish the connection between the averaging procedure through a Gaussian kernel and the well known macroscopic average [150]. For this purpose, consider an ideal superlattice of period L along the stacking direction, resulting from the alternation of two crystalline slabs with different lattice spacings $b_1 > b_2$, both much shorter than L. The prescription of the macroscopic average technique consists in filtering twice the function of interest by means of a rectangle kernel [98]. In reciprocal space this corresponds to applying a weight,

$$w(G) = \frac{\sin(Gb_1/2)}{Gb_1/2}\frac{\sin(Gb_2/2)}{Gb_2/2}, \tag{B.1}$$

to the coefficients in the Fourier expansion. This results in setting equal to zero all the Fourier coefficients which correspond to G's which are integer multiples of $2\pi/b_1$ or $2\pi/b_2$, without affecting in a significant way the behavior of the function on the scale of the superlattice periodicity since $2\pi/L \ll 2\pi/b_{1,2}$. This method is best suited for a superlattice composed of ideal crystalline slabs. However, when the crystals deviate from perfect periodicity, for instance in the presence of strain at the interfaces, the method is less efficient in filtering the spurious lattice spacings. Moreover, the extension of this technique to disordered three-dimensional systems with short-range order is not well defined.

We considered a generalization of the macroscopic average which overcomes these shortcomings. To this end, we determined the asymptotic form of the averaging kernel resulting from the serial application of rectangle filters with $b_1, b_2, \cdots b_N$ widths. In reciprocal space, the averaging kernel has the following weight function:

$$w_N(G) = \prod_{n=1}^{N} \frac{\sin(Gb_n/2)}{Gb_n/2}, \tag{B.2}$$

which, to lowest order in powers of G, corresponds to

$$\widetilde{w}_N(G) = \exp(-G^2\sigma_N^2/2), \tag{B.3}$$

where $\sigma_N = \overline{b}\sqrt{N/12}$, $\overline{b}$ being the root mean square period of the series. Now, the Gaussian weight in Eq. (B.3) corresponds to the asymptotic form of Eq. (B.2) in the limit of large N, as can be seen by invoking the central limit theorem of probability theory. Indeed, a rectangle function can be thought as the probability distribution of a uniform random variable. Furthermore, the probability distribution of independent random variables can be calculated as the convolution of the corresponding distributions [151]. Hence, the convolution of many rectangle functions, as given by Eq. (B.2), yields the probability distribution of the sum of the corresponding random variables [151]. Now, the central limit theorem states that this sum must converge to a normal random variable [151], therefore the convolution of rectangles must converge to a Gaussian function. By continuity, this function must be given by Eq. (B.3).

The difference between the rectangle and Gaussian filters resides in the fact that the former sets the coefficients of the frequencies which are multiples of $2\pi/b_n$ exactly to zero, while the latter only suppresses their amplitudes. The larger the width of the Gaussian kernel, the more effective will be this suppression. A compromise must therefore be found between the width of the kernel in real space and the degree of suppression of the undesired Fourier components. For the range of applications considered in this thesis, we found that the Gaussian filter reduces the amplitudes of the fluctuations to less than 1% of the average value when the full-width at half-maximum of the real-space kernel is $\sim 1.5\ \max(b_1, b_2)$, only slightly larger than the width of the trapezoidal filter corresponding to a double macroscopic average [98].

Appendix C

Asymmetric dipole densities at the Si-SiO_2 interface

We investigate the enhancement of the permittivity observed on the Si side of the Si(100)-SiO_2 interface (Sec. 5.2.1) by means of the Wannier function approach introduced in Sec. 2.1.2.

Focusing on interface model C-II, where the effect is more prominent, we distinguish the contributions to the susceptibility arising from Si-Si bonds in the Si slab and from Si-Si bonds in the suboxide (Fig. 5.3). We only address Si-Si bonds since Si-O bonds and nonbonding O orbitals were found to be far less polarizable so that their effect is negligible in this context. As shown in Fig. 5.3, the origin of the enhancement clearly results from the contribution due to the Si-Si bonds in the suboxide. Notice that this contribution peaks within the Si slab, although the suboxide Si-Si bonds from which it originates are located outside the Si slab.

To clarify this point, we focus on a Si^{1+}-Si^{2+} bond of the suboxide. We show in Fig. C.1 that the corresponding charge density induced by a positive electric field decays exponentially away from the center of the bond, with two different decay lengths in Si and SiO_2: $\lambda_{\mathrm{Si}} \simeq 1.7$ Å and $\lambda_{\mathrm{SiO_2}} \simeq 0.7$ Å. By means of a simple model, we show in the following that such different decay lengths give rise to an asymmetric contribution to the local susceptibility, which peaks in the Si slab.

We assume a sharp interface at $x = 0$ between a dielectric of permittivity ε_{l} on the left and one of permittivity ε_{r} on the right. Following Fig. C.1, we model the induced charge density of a single Wannier function as

$$\rho_{\mathrm{ind}}(x) = \begin{cases} -\rho^{\mathrm{l}}_{\mathrm{ind}} \exp(\quad x/\lambda_{\mathrm{l}}) & x < 0 \\ \rho^{\mathrm{r}}_{\mathrm{ind}} \exp(-x/\lambda_{\mathrm{r}}) & x > 0 \end{cases}, \tag{C.1}$$

where $\rho^{\mathrm{l}}_{\mathrm{ind}}$ and $\rho^{\mathrm{r}}_{\mathrm{ind}}$ are coeficients which satisfy the condition of charge neutrality:

$$\rho^{\mathrm{l}}_{\mathrm{ind}} \lambda_{\mathrm{l}} = \rho^{\mathrm{r}}_{\mathrm{ind}} \lambda_{\mathrm{r}}. \tag{C.2}$$

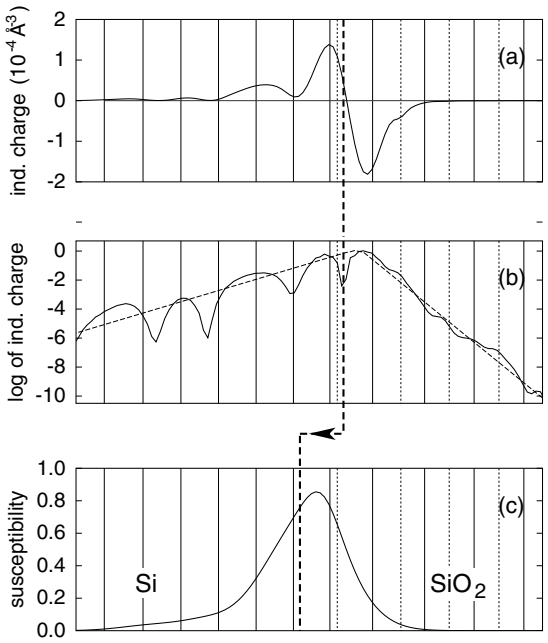

Figure C.1: (a) Induced charge density corresponding to a Si^{+1}-Si^{+2} bond in the suboxide of model C-II of the Si(100)-SiO_2 interface. The magnitude of the electric field applied to the simulation cell is 10^{-3} a.u. The vertical bold line indicates the center of the Wannier function. (b) Same as (a) but in absolute value and on a logarithmic scale (solid). We also show the corresponding approximation in terms of decaying exponentials (dashed). (c) Contribution to the susceptibility profile arising from the same bond as in (a)-(b). The bold dashed line indicates the center of the distribution, shifted towards the Si slab. In all panels, vertical lines represent planes of Si (solid) and O (dotted) atoms.

Using Eqs. (2.13)-(2.17), we derive the contribution $\delta\chi(x)$ of this Wannier function to the local susceptibility:

$$\delta\chi(x) \propto \begin{cases} \varepsilon_{\rm l}\exp(\ \ x/\lambda_{\rm l}) & x<0 \\ \varepsilon_{\rm r}\exp(-x/\lambda_{\rm r}) & x>0 \end{cases} . \tag{C.3}$$

The mean of this distribution is found to be

$$\langle x\rangle = \frac{\varepsilon_{\rm r}\lambda_{\rm r}^2 - \varepsilon_{\rm l}\lambda_{\rm l}^2}{\varepsilon_{\rm r}\lambda_{\rm r} + \varepsilon_{\rm l}\lambda_{\rm l}} \simeq -\lambda_{\rm l}, \tag{C.4}$$

where the last equality holds when $\varepsilon_{\rm r}\lambda_{\rm r} \ll \varepsilon_{\rm l}\lambda_{\rm l}$, as is the case at the Si-SiO_2 interface (with Si and SiO_2 on the left and right sides, respectively). Equation (C.4) indicates that, while the Wannier function is centered at $x=0$, its contribution to the susceptibility is shifted towards the left by an amount of $\lambda_{\rm l}$. For the Si^{1+}-Si^{2+} bond in the suboxide of model C-II, Eq. (C.4) gives a shift of the susceptibility distribution of about $-\lambda_{\rm Si} \simeq -1.7$ Å, which compares favorably with the shift of -1.62 Å calculated for the actual contribution to the local susceptibility of this bond [Fig. C.1(c)].

These considerations show that the origin of the asymmetric susceptibility distribution results from the different decay lengths of the induced charge at the interface. The decay length towards the Si side of the interface is characteristic of bulk Si, while the decay length towards the SiO_2 side results from the evanescent nature of the involved Si states in SiO_2. Indeed, we calculated a typical decay length of *mid-gap* evanescent states in the oxide of the interface model C-II of $\simeq$ 0.8 Å, close to the decay length of the induced charge density of the Si-Si bond in SiO_2 ($\lambda_{\rm SiO_2} \simeq 0.7$ Å).

Appendix D

Taylor expansion of the Berry-phase position operator

We consider a many-electron system in a supercell geometry with Γ point sampling. The matrix elements of the Berry-phase position operator [76] along the x direction are given by

$$S_{mn} = \langle \psi_m | e^{iqx} | \psi_n \rangle, \tag{D.1}$$

where $\{|\psi_n\rangle\}$ is a basis of single-particle orbitals, and $q = 2\pi/L$ with L the supercell size along x. We hereafter expand S_{mn} in powers of ξ/L, being ξ the maximum spread of the maximally localized Wannier functions $\{|W_n\rangle\}$ for the system considered. We start by calculating the matrix elements of the position operator in the Wannier function basis:

$$Q_{mn} = \langle W_m | e^{iqx} | W_n \rangle. \tag{D.2}$$

For this purpose, we first write the Wannier functions at the Γ point as

$$W_n(x) = \sum_{p=-\infty}^{+\infty} w_n(x - pL; x_n), \tag{D.3}$$

where p is an integer and the functions $w_n(x; x_n)$ are centered at $x = x_n$ and vanish for $|x - x_n| > \xi_n$. The latter assumption is based on the exponential localization of the Wannier functions [152], and can be removed by keeping track of the overlap between the states. The x_n in Eq. (D.3) correspond to the actual locations of the Wannier states in the supercell. We can take $x_n > x_m$ without loss of generality. To express Q in powers of ξ/L, we observe that Q_{mn} vanishes when $x_n - x_m > \xi_m + \xi_n$ because the states do not overlap. Conversely, when $x_n - x_m < \xi_m + \xi_n$, the overlap is finite and we have:

$$Q_{mn} = \int_{\text{cell}} dx\; W_m^*(x) e^{iqx} W_n(x) = \int_{\infty} dx\; w_m^*(x; x_m) e^{iqx} w_n(x; x_n), \tag{D.4}$$

where the first integral is over the supercell, while the second is over the whole space. In Eq. (D.4), only one element of the double summation arising from Eq. (D.3) is nonvanishing, because the integral in the second term is restricted to the supercell.

By defining $x_{mn} = (x_m + x_n)/2$ and $d_{mn} = (x_n - x_m)/2$, we can rewrite Eq. (D.4) as

$$Q_{mn} = \int_{\infty} dx\ w_m^*(x + d_{mn}; x_{mn}) e^{iqx} w_n(x - d_{mn}; x_{mn}). \tag{D.5}$$

By changing the integration variable into $x - x_{mn}$ we get:

$$Q_{mn} = e^{iqx_{mn}} \int_{\infty} dx\ w_m^*(x + d_{mn}; 0) e^{iqx} w_n(x - d_{mn}; 0). \tag{D.6}$$

From the localization properties of w_n and w_m, the integrand vanishes unless $\mid x \mid < d_{mn} + \xi_{mn}/2$, where $\xi_{mn} = \xi_m + \xi_n$. Furthermore, the condition of finite overlap implies that $d_{mn} < \xi_{mn}/2$, therefore the integrand in Eq. (D.6) is non-vanishing only for $\mid x \mid < \xi_{mn}$. These considerations imply that the argument in the exponential is $|qx| < 2\pi\xi_{mn}/L < 2\pi\xi/L < 1$, leading to the following power expansion:

$$Q_{mn} = e^{iqx_{mn}} \int_{\infty} dx\ w_m^*(x + d_{mn}; 0)\{1 + iqx - \frac{1}{2}q^2x^2 + i\mathcal{O}\Big(\frac{\xi}{L}\Big)^3\} w_n(x - d_{mn}; 0). \tag{D.7}$$

By considering each term separately, Eq. (D.7) can be rewritten through the *localized* functions $w_m(x; x_m)$ and $w_n(x; x_n)$:

$$\begin{aligned} Q_{mn} &= e^{iqx_{mn}}\{A_{mn} + iq(B_{mn} - A_{mn}x_{mn}) \\ &\quad -\frac{1}{2}q^2(C_{mn} + A_{mn}x_{mn}^2 - 2B_{mn}x_{mn}) + i\mathcal{O}\Big(\frac{\xi}{L}\Big)^3\}, \end{aligned} \tag{D.8}$$

where the auxiliary matrices A, B and C are defined as follows:

$$A_{mn} = \langle w_m | w_n \rangle, \tag{D.9}$$

$$B_{mn} = \langle w_m | x | w_n \rangle, \tag{D.10}$$

$$C_{mn} = \langle w_m | x^2 | w_n \rangle. \tag{D.11}$$

We note that Eq. (D.8), derived for the case of two overlapping Wannier states, maintains its validity also in the non-overlapping case. In fact, if W_m and W_n have negligible overlap, then A_{mn}, B_{mn} and C_{mn} vanish, in agreement with Eq. (D.8). If we now define the matrix $D_{mn} = x_m\delta_{mn}$, Eq. (D.8) can be rewritten in matrix notation:

$$\begin{aligned} e^{-iqD/2}Qe^{-iqD/2} &= A + iq(B - \frac{1}{2}AD - \frac{1}{2}DA) \\ &\quad -\frac{1}{2}q^2(C + \frac{1}{2}DAD + \frac{1}{4}D^2A + \frac{1}{4}AD^2 - BD - DB) \\ &\quad +i\mathcal{O}\Big(\frac{\xi}{L}\Big)^3. \end{aligned} \tag{D.12}$$

By introducing the anticommutator $\{\cdots\}$, the previous expression reads:

$$\begin{aligned} e^{-iqD/2}Qe^{-iqD/2} &= A + iq\Big(B - \frac{1}{2}\{A,D\}\Big) \\ &\quad -\frac{1}{2}q^2\Big(C + \frac{1}{4}\{D,\{A,D\}\} - \{B,D\}\Big) \\ &\quad +i\mathcal{O}\Big(\frac{\xi}{L}\Big)^3. \end{aligned} \tag{D.13}$$

Equation (D.13) simplifies when the states $|w_n\rangle$ are taken mutually orthogonal and normalized, so that the overlap A coincides with the identity matrix I:

$$\begin{aligned} e^{-iqD/2}Qe^{-iqD/2} &= I + iq(B - D) \\ &\quad -\frac{1}{2}q^2(C + D^2 - \{B,D\}) \\ &\quad +i\mathcal{O}\Big(\frac{\xi}{L}\Big)^3. \end{aligned} \tag{D.14}$$

Equation (D.14) states that the position operator expressed in a basis of localized Wannier functions is given, to zeroth order, by a diagonal matrix with the complex exponential of the corresponding positions on the diagonal. The more localized the Wannier states, the smaller the off-diagonal elements. This observation is in line with a recently proposed technique for determining maximally localized Wannier function, which consists of finding the unitary transform which makes the position operator *maximally diagonal* [75].

By using Eq. (D.14) we recover the usual expressions for the expectation values of the position of a set of Bloch functions and the corresponding localization tensor. Indeed, after a little algebra we find:

$$\mathrm{Im}\,\frac{1}{q}\ln\det Q = \mathrm{Tr}B + \mathcal{O}\Big(\frac{\xi}{L}\Big)^2, \tag{D.15}$$

$$-\frac{2}{q^2}\ln|\det Q| = \mathrm{Tr}[C - B^2] + \mathcal{O}\Big(\frac{\xi}{L}\Big)^2. \tag{D.16}$$

In obtaining Eqs. (D.15) and (D.16) we made use of the matrix property: ln det = Tr Ln, Tr being the matrix trace and Ln the matrix logarithm. By replacing the definitions of Eqs. (D.9), (D.10), and (D.11) in Eqs. (D.15) and (D.16) we find:

$$\mathrm{Im}\,\frac{1}{q}\ln\det Q = \sum_n \langle w_n|x|w_n\rangle + \mathcal{O}\Big(\frac{\xi}{L}\Big)^2, \tag{D.17}$$

$$-\frac{2}{q^2}\ln|\det Q| = \sum_n \langle w_n|x(1-\hat{P})x|w_n\rangle + \mathcal{O}\Big(\frac{\xi}{L}\Big)^2, \tag{D.18}$$

with $\hat{P}$ the projector onto the occupied states. Eq. (D.17) gives the position of the many-electron system, and Eq. (D.18) gives the corresponding localization tensor [153], within a single-particle picture.

Since the matrix determinant does not change upon unitary transforms, the previous expressions hold unchanged when the position operator is developed in a basis of Bloch functions (i.e. when using S_{mn} instead of Q_{mn}):

$$\mathrm{Im}\,\frac{1}{q}\,\ln\det S = \sum_n \langle w_n|x|w_n\rangle + \mathcal{O}\Big(\frac{\xi}{L}\Big)^2, \tag{D.19}$$

$$-\frac{2}{q^2}\,\ln|\det S| = \sum_n \langle w_n|x(1-\hat{P})x|w_n\rangle + \mathcal{O}\Big(\frac{\xi}{L}\Big)^2, \tag{D.20}$$

With Eqs. (D.19) and (D.20) we recover the well know results about the position and localization of a system of Bloch functions [153]. We observe that the present derivation constitutes an extension of the more familiar case of an isolated electron in a periodic box [153].

The L^{-2} convergence of the Berry-phase position operator has been obtained here by implicitly assuming a fixed k-point sampling of the electronic structure, and is in agreement with a previous analysis [77].

Appendix E

Local permittivity and inverse dielectric matrix

We here state the relation between the local permittivity introduced in Sec. 2.1.1 and the inverse dielectric matrix $\varepsilon^{-1}_{ij}(\mathbf{r},\mathbf{r}')$ [154] (we omit the frequency dependence for ease of notation). For this purpose, we first apply the planar average and the Gaussian filter to both sides of Eq. (2.1):

$$\int d\mathbf{r}' w(\mathbf{r}-\mathbf{r}') p_i(\mathbf{r}') = \int d\mathbf{r}' \int d\mathbf{r}'' w(\mathbf{r}-\mathbf{r}') \chi_{ij}(\mathbf{r}',\mathbf{r}'') e_j(\mathbf{r}''), \tag{E.1}$$

where the weight function $w(\mathbf{r})$ corresponds to the double averaging. Next, we rewrite Eq. (2.3) by making explicit the smoothing procedure:

$$\int d\mathbf{r}' w(\mathbf{r}-\mathbf{r}') p_i(\mathbf{r}') = \chi^{\mathrm{loc}}_{ij}(\mathbf{r}) \int d\mathbf{r}' w(\mathbf{r}-\mathbf{r}') e_j(\mathbf{r}'). \tag{E.2}$$

In the previous expression, the superscript "loc" has been introduced in order to distinguish between the inverse dielectric matrix and the local permittivity introduced in Sec. 2.1.1. Now, by combining Eqs. (E.1), (E.2) we obtain

$$\chi^{\mathrm{loc}}_{ij}(\mathbf{r}) = \frac{\int d\mathbf{r}' \int d\mathbf{r}'' w(\mathbf{r}-\mathbf{r}') \chi_{ij}(\mathbf{r}',\mathbf{r}'') e_j(\mathbf{r}'')}{\int d\mathbf{r}' w(\mathbf{r}-\mathbf{r}') e_j(\mathbf{r}')}. \tag{E.3}$$

The last equation can more conveniently be written in terms of the dielectric permittivity tensors [$\varepsilon^{\mathrm{loc}}_{ij}(\mathbf{r}) = \delta_{ij} + 4\pi\chi^{\mathrm{loc}}_{ij}(\mathbf{r})$ and $\varepsilon_{ij}(\mathbf{r},\mathbf{r}') = \delta_{ij}(\mathbf{r},\mathbf{r}') + 4\pi\chi_{ij}(\mathbf{r},\mathbf{r}')$]:

$$\varepsilon^{\mathrm{loc}}_{ij}(\mathbf{r}) = \frac{\int d\mathbf{r}' \int d\mathbf{r}'' w(\mathbf{r}-\mathbf{r}') \varepsilon_{ij}(\mathbf{r}',\mathbf{r}'') e_j(\mathbf{r}'')}{\int d\mathbf{r}' w(\mathbf{r}-\mathbf{r}') e_j(\mathbf{r}')}. \tag{E.4}$$

The selfconsistent microscopic field $e_i(\mathbf{r})$ in Eq. (E.4) is related to the external electric field $E^{\mathrm{ext}}_i(\mathbf{r})$ by

$$e_i(\mathbf{r}) = \int d\mathbf{r}' \varepsilon^{-1}_{ij}(\mathbf{r},\mathbf{r}') E^{\mathrm{ext}}_j(\mathbf{r}'), \tag{E.5}$$

with the dielectric matrices obeying the closure condition

$$\int d\mathbf{r}' \varepsilon_{ij}^{-1}(\mathbf{r}, \mathbf{r}') \varepsilon_{jk}(\mathbf{r}', \mathbf{r}'') = \delta_{ik}(\mathbf{r}, \mathbf{r}''). \tag{E.6}$$

By combining Eqs. (E.4)-(E.6) we obtain

$$[\varepsilon_{ij}^{\mathrm{loc}}(\mathbf{r})]^{-1} = \frac{\int d\mathbf{r}' \int d\mathbf{r}'' w(\mathbf{r} - \mathbf{r}') \varepsilon_{jk}^{-1}(\mathbf{r}', \mathbf{r}'') E_k^{\mathrm{ext}}(\mathbf{r}'')}{\int d\mathbf{r}' w(\mathbf{r} - \mathbf{r}') E_i^{\mathrm{ext}}(\mathbf{r}')}. \tag{E.7}$$

If we now take the external field uniform and oriented along the $i = 3$ direction, the diagonal component $\varepsilon_{33}^{\mathrm{loc}}(\mathbf{r})$ of the local dielectric tensor reads

$$[\varepsilon_{33}^{\mathrm{loc}}(\mathbf{r})]^{-1} = \int d\mathbf{r}' w(\mathbf{r} - \mathbf{r}') \int d\mathbf{r}'' \varepsilon_{33}^{-1}(\mathbf{r}', \mathbf{r}''). \tag{E.8}$$

If the smoothing kernel $w(\mathbf{r})$ is chosen to be close to unity for $|\mathbf{r}| < \lambda$ and vanishing for $|\mathbf{r}| > \lambda$ (with λ the localization length of the inverse dielectric matrix), then the integration on $\mathbf{r}''$ in Eq. (E.8) can be approximated as:

$$\int d\mathbf{r}'' \varepsilon_{33}^{-1}(\mathbf{r}', \mathbf{r}'') \simeq \int d\mathbf{r}'' w(\mathbf{r} - \mathbf{r}'') \varepsilon_{33}^{-1}(\mathbf{r}', \mathbf{r}''). \tag{E.9}$$

Therefore, Eq. (E.8) can be rewritten as

$$[\varepsilon_{33}^{\mathrm{loc}}(\mathbf{r})]^{-1} = \int d\mathbf{r}' \int d\mathbf{r}'' w(\mathbf{r} - \mathbf{r}') w(\mathbf{r} - \mathbf{r}'') \varepsilon_{33}^{-1}(\mathbf{r}', \mathbf{r}''), \tag{E.10}$$

providing a transparent relation between the local permittivity introduced in Sec. 2.1.1 and the inverse dielectric matrix.

Appendix F

Si $2p$ core-level shifts at Si(100)-$Zr_xSi_{1-x}O_2$ interfaces

Among the many candidates for the replacement of SiO_2 in gate insulator stacks on silicon, zirconium silicates $Zr_xSi_{1-x}O_2$ appear promising, showing thermal stability upon Si and excellent electrical properties [155, 156, 157]. Recently, Si $2p$ core-level photoemission spectroscopy has been used to assess the bonding properties at Si(100)-$Zr_xSi_{1-x}O_2$ interfaces. The measured binding energies were found to be shifted with respect to the SiO_2 line at Si(100)-SiO_2 interfaces by values scattered between 0 and 1.5 eV [156, 157, 158, 159, 160, 161].

In this Appendix, we investigate Si $2p$ core-level shifts at Si(100)-$Zr_xSi_{1-x}O_2$ interfaces using a first-principles approach. For a model interface obtained by matching crystalline zircon to a Si(100) substrate, we calculated Si $2p$ binding energies and we found a linear dependence on the number of second nearest neighbor Zr atoms. This result was validated through molecular cluster calculations, which in addition highlighted the role of the oxygen coordination of the Zr atoms. Combining these findings with structural models generated by classical molecular dynamics, we obtained the dependence of Si $2p$ shifts on the Zr content in the film, in good agreement with available experimental data.

First-principles calculations were performed with the same techniques described in Sec. 2.2.1. In particular, we used an ultrasoft pseudopotential for Zr atoms, with the $4s$ and $4p$ semicore states included among the valence states. We calculated Si $2p$ core-level shifts including the effect of core-hole relaxation by taking energy differences between two separate calculations. For this purpose, first the ground state energy was determined; then the pseudopotential of a given Si atom was replaced by another pseudopotential simulating the presence of a screened $2p$ hole in its core [162, 17, 18]. In the presence of a core hole, a neutralizing background was used to ensure charge neutrality. In this way, relative binding energies could be obtained.

We obtained a model Si(100)-$(ZrO_2)_{0.5}(SiO_2)_{0.5}$ interface by matching crystalline zircon to Si(100) through oxygen bridges. To achieve this attachment, the

zircon structure was compressed along the [100] and [010] directions by the ratio of lattice constants, $r = a_{ZrSiO4}/a_{Si} \cong 1.22$. We restored the zircon density by expanding the structure in the [001] direction by a factor r^2 before allowing for full relaxation. These adjustments lowered the O coordination of the Zr atoms from eight to four. We used a periodic slab structure defined by a $\sqrt{8} \times \sqrt{8}$ Si interface unit, containing 12 Å of oxide and 8 Si monolayers. Dangling bonds at exposed surfaces were saturated by H atoms. After relaxation, the silicate density was found to be 4.50 g/cm^3, consistent with the density of crystalline zircon (4.65 g/cm^3) and in fair agreement with the density of amorphous $Zr_xSi_{1-x}O_2$ with the same Zr content (3.96 g/cm^3) [163]. The distribution of Si-O bond lengths peaks at 1.65 Å. At the interface, we found a few larger Si-O bond lengths of about 1.73 Å for Si atoms in the Si^{+2} oxidation state (cf. Secs. 4.1.2 and 4.2.2). We found Zr-O bond lengths around 1.99 Å, slightly lower than measured values for amorphous $Zr_xSi_{1-x}O_2$ (2.1 and 2.3 Å) [164]. Such small Zr-O bond lengths owe little to the artificial strain in the structure, being conversely due to the oxygen coordination of the Zr atoms. Indeed, for relaxed $Zr(OH)_4(H_2O)_{p-4}$ clusters (with $p = 4, ..8$), the Zr-O bond lengths were found to increase with p from 1.96 to 2.08 Å for valence bonds, and from 2.39 to 2.48 Å for dative bonds.

The average calculated 2*p* core-level of silicon atoms in the Si^{+4} oxidation state for the model Si(100)-$Zr_xSi_{1-x}O_2$ interface was found to be displaced by 1.1 eV towards lower binding energies with respect to the corresponding SiO_2 line at the Si(100)-SiO_2 interface [22] (Fig. F.1, inset). The theoretical shift of 1.1 eV compares well with the experimental value of 0.9 eV [160], obtained for a film with a similar Zr content. Further analysis shows that the shifts increase linearly with the number of Zr atoms in the second coordination shell (Fig. F.1).

In order to examine how Si 2*p* core-levels are affected by the number of *Zr atoms in the second coordination shell*, we considered molecular clusters composed of Si, O, and Zr atoms: $Si(OSi(OH)_3)_{4-m}(OZr(OH)_3)_m$, with $m = 1, ..4$.

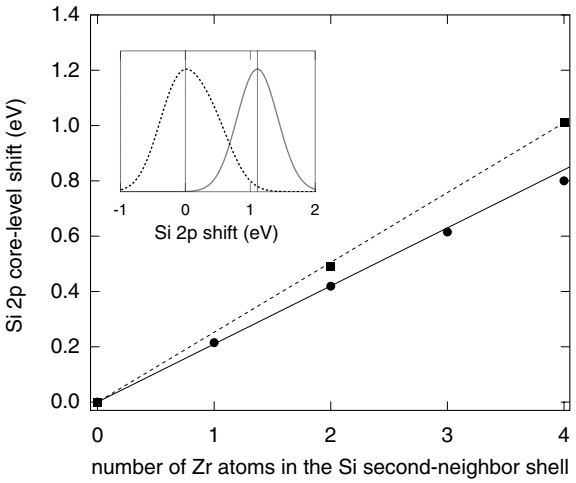

Figure F.1: Si 2*p* core-level shifts referred to the SiO_2 line vs Zr second-neighbors for the model Si(100)-$Zr_xSi_{1-x}O_2$ interface (squares) and the molecular clusters (disks). Positive shifts indicate lower binding energies. The solid line corresponds to Eq. (F.1). The dotted line is a guide to the eye. Inset: distributions of Si^{+4} shifts for model Si(100)-$Zr_xSi_{1-x}O_2$ (solid) and Si(100)-SiO_2 (dashed, from Ref. [22]) interfaces. A Gaussian broadening of 0.3 eV was used.

These clusters contain a tetrahedral SiO_4 core unit which is terminated by either $-Si(OH)_3$ or $-Zr(OH)_3$ groups. First, we only considered fourfold coordinated Zr atoms. We fixed the Si-O bond lengths to 1.62 Å corresponding to the relaxed bond length in our theoretical framework, and adjusted the structure around the Zr atom according to the geometry resulting from a separate relaxation of the Zr-centered cluster $Zr(OH)_4$. Other bond lengths were fixed to typical values. The Si-O-Si angles were taken equal to 180°. We used a periodic cubic cell with a side of 40 bohr, sufficiently large to minimize interactions between periodic neighbors. The shifts are hereafter referred to the binding energy for the cluster without Zr atoms ($m=0$). Calculated shifts were found to increase linearly with the number of Zr atoms in the second coordination shell, in good agreement with the shifts calculated for the model Si(100)-$Zr_xSi_{1-x}O_2$ interface (Fig. F.1). We attribute the small differences to substrate screening effects associated to the ultrathin oxide in our model. Since the thickness of Zr silicate films is generally much larger, such effects can be safely neglected. We verified in addition that our results are essentially unaffected by small structural modifications.

We then specifically considered how Si $2p$ shifts are affected by the *O coordination of second nearest neighbor Zr atoms*. For this purpose, we considered molecular clusters with a central Si atom and a single Zr atom in its second coordination shell: $Si(OSi(OH)_3)_3OZr(OH)_3$. By adding datively bonded water molecules [165], we could vary the O coordination p of the Zr atom from 4 to 8, covering the experimentally observed range of coordinations [164]. For every O coordination p, the structure around the Zr atom was adjusted according to the geometry of the fully relaxed $Zr(OH)_4(H_2O)_{p-4}$ cluster. The calculated Si $2p$ shifts increase approximately linearly with p, the largest deviation from linearity being about 0.1 eV for the sixfold coordinated Zr atom.

So far, we investigated the effect of the O coordination for a single Zr atom in the second coordination shell. On the basis of the results for fourfold coordinated Zr atoms, it is reasonable to assume that the linear dependence of the Si $2p$ shift on the composition of the second shell still holds. To check the validity of this assumption, we considered the extremal case in which the central Si atom is coordinated in its second shell by 4 Zr atoms, all eightfold coordinated by O atoms ($m = 4$ and $p = 8$). We found a shift of 1.89 eV, close to four times the value of 0.52 eV calculated for a single eightfold coordinated Zr atom in the second shell ($m = 1$ and $p = 8$). We therefore took the microscopic Si $2p$ shift to be linearly dependent on both m and p ($m = 1, ..4$, $p = 4, ..8$):

$$\Delta E \simeq \; m\,[0.21 + 0.07\,(\overline{p} - 4)] \text{ eV} \tag{F.1}$$

where $\overline{p}$ is the average O coordination of Zr atoms in the Si second coordination shell and the parameters optimally describe in a least square sense the full set of calculated shifts. This relation describes the calculated shifts with a rms error of 0.06 eV, and is expected to hold for m up to 4, corresponding to a Zr content $x \sim 0.5$ (Fig. F.2).

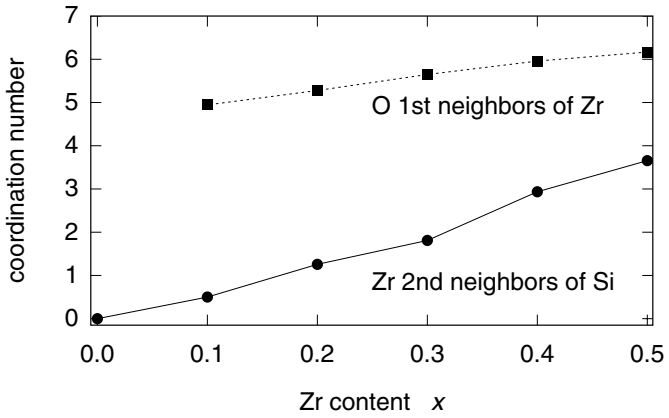

Figure F.2: Average number of Zr atoms in the second Si coordination shell (disks) and average number of O atoms in the first Zr coordination shell (squares) vs Zr content x for the amorphous Zr silicates model structures.

In order to compare with experimental shifts resulting from macroscopic samples, it is necessary to average the calculated microscopic shifts over appropriate network structures. For this purpose, we generated amorphous $Zr_xSi_{1-x}O_2$ model structures by adopting a classical molecular dynamics scheme based on Born-Mayer-Huggins potentials [166]. For each value of $x = 0, 0.1, .., 0.5$, we obtained three model structures, consisting of 60 $(ZrO_2)_x(SiO_2)_{1-x}$ units at the experimental density [163]. Starting from random atomic positions, the melts were equilibrated at 5500 K for 250 ps, and then quenched with a cooling rate of 10 K/ps to give the final structures. Figure F.2 shows the average number of Zr atoms in the Si second coordination shells $\langle m \rangle$ and the average O coordination of the Zr atoms $\langle p \rangle$, as a function of x. Coordination numbers are defined by cutoff distances of 1.8 Å for Si-O and 2.8 Å for Zr-O, corresponding to the first minima in the respective pair correlation functions. Both $\langle m \rangle$ and $\langle p \rangle$ were found to increase almost linearly with x. The increase of $\langle p \rangle$ is in fair accord with experimental results [164].

To obtain the average Si 2*p* shift $\langle \Delta E \rangle$ as a function of Zr content x, we combined the microscopic relation Eq. (F.1) with the coordination properties of

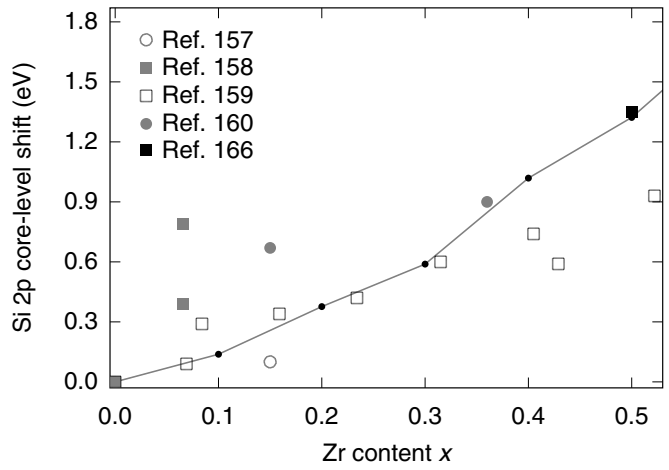

Figure F.3: Comparison between calculated (solid) and experimental Si 2*p* core-level shifts at Si(100)-$Zr_xSi_{1-x}O_2$ interfaces as a function of Zr content x. The shifts are given with respect to the bulk SiO_2 line, positive values indicating lower binding energies.

the amorphous $Zr_xSi_{1-x}O_2$ model networks. Since the distributions of m and p were found to be almost independent ($\langle mp\rangle \simeq \langle m\rangle\langle p\rangle$), $\langle \Delta E\rangle$ could be expressed for every x in terms of the averages $\langle m\rangle$ and $\langle p\rangle$ given in Fig. F.2. Figure F.3 shows the Si $2p$ shift $\langle \Delta E\rangle$ as calculated, together with the available experimental data for thin $Zr_xSi_{1-x}O_2$ films [158, 159, 160, 161] and for zircon [167]. The calculated Si $2p$ shifts increase steadily with the Zr content x. The same trend is also observed in the experimental data, despite the noticeable scattering. In particular, comparing with the systematic study of Ref. [160], we found a good quantitative agreement up to a Zr content of $x \sim 0.3$.

The overestimation of the experimental Si-$2p$ shifts for Zr content $x > 0.3$ can be rationalized as follows: the relaxation energy of the core-hole calculated through the molecular clusters does not include the electrostatic screening arising from the surrounding zirconium silicate of the actual system. Since the permittivity of the zirconium silicate increases with the Zr content, this approximation worsens with increasing x, explaining the deviation with respect to experiment at large Zr content. By using classical electrostatics arguments, the following *qualitative* estimate of the correction $\Delta E_{\rm corr}(x)$ to the calculated shifts is obtained:

$$\Delta E_{\rm corr}(x) = -e^2\Big(R_{\rm clus}^{-1} - R_{\rm cell}^{-1}\Big)\Big[\varepsilon_\infty^{-1}(x{=}0) - \varepsilon_\infty^{-1}(x)\Big], \qquad \text{(F.2)}$$

with e the electronic charge, $R_{\rm clus}$ and $R_{\rm cell}$ the average radii of the molecular cluster and of the computational cell, respectively, and $\varepsilon_\infty(x)$ the electronic permittivity of the zirconium silicate with a Zr content x. Typical values of $R_{\rm clus}$ and $R_{\rm cell}$ used in our calculations are $\sim$4 Å and $\sim$13 Å, respectively, while the permittivity of the zirconium silicate can be taken to vary linearly as a function of x between those of SiO_2 ($\varepsilon_\infty = 2.1$) and of ZrO_2 ($\varepsilon_\infty = 5.8$). By using these data in Eq. (F.2) we found a correction of -0.6 eV for $x = 0.5$, which brings the calculated values of Fig. F.1 closer to experiment.

In conclusion, in this Appendix we established a relation between the Si $2p$ core-level shifts at Si(100)-$(ZrO_2)_x(SiO_2)_{1-x}$ interfaces and the underlying microscopic structure. Our results support the use of the Si $2p$ shift as an indicator of the Zr content x in the silicate film.

Bibliography

[1] See the manufacturer website at `www.intel.com`.

[2] G. E. Moore, Electronics Magazine **38**, (1965).

[3] G. D. Wilk, R. M. Wallace, and J. M. Anthony, J. Appl. Phys. **89**, 5243 (2001).

[4] M. Schulz, Nature (London) **399**, 729 (1999).

[5] D. A. Muller, T. Sorsch, S. Moccio, F. H. Baumann, K. Evans-Lutterodt, and G. Timp, Nature (London) **399**, 758 (1999).

[6] *2003 International Technology Roadmap for Semiconductors*, Semiconductor Industry Association (`http://public.itrs.net`).

[7] D. A. Muller and G. D. Wilk, Appl. Phys. Lett. **79**, 4195 (2001).

[8] S. Van Elshocht, M. Caymax, S. De Gendt, T. Conard, J. Pétry, L. Daté, D. Pique, and M. M. Heyns, J. Electrochem. Soc. **151**, F77 (2004).

[9] M. L. Green, E. P. Gusev, R. Degraeve, and E. L. Garfunkel, J. Appl. Phys. **90**, 2057 (2001).

[10] A. C. Diebold, D. Venables, Y. Chabal, D. Muller, M. Weldon, and E. Garfunkel, Mat. Sci. Semic. Proc. **2**, 103 (1999).

[11] T. A. Rabedeau, I. M. Tidswell, P. S. Pershan, J. Bevk, and B. S. Freer, Appl. Phys. Lett. **59**, 3422 (1991).

[12] S. C. Witczak, J. S. Suehle, and M. Gaitan, Solid-State Electron. **35**, 345 (1992).

[13] A. Stesmans and V. V. Afanas'ev, J. Phys.: Condens. Matter **10**, L19 (1998).

[14] F. J. Himpsel, F. R. McFeely, A. Taleb-Ibrahimi, J. A. Yarmoff, and G. Hollinger, Phys. Rev. B **38**, 6084 (1988).

[15] F. Rochet, C. Poncey, G. Dufour, H. Roulet, C. Guillot, and F. Sirotti, J. Non-Crystall. Sol. **216**, 148 (1997).

[16] J. H. Oh, H. W. Yeom, Y. Hagimoto, K. Ono, M. Oshima, N. Hirashita, M. Nywa, A. Toriumi, and A. Kakizaki, Phys. Rev. B **63**, 205310 (2001).

[17] A. Pasquarello, M. S. Hybertsen, and R. Car, Phys. Rev. Lett. **64**, 1024 (1995).

[18] A. Pasquarello, M. S. Hybertsen, and R. Car, Phys. Rev. B **53**, 10942 (1996).

[19] L. C. Feldman, P. J. Silverman, J. S. Williams, T. E. Jackman, and I. Stensgaard, Phys. Rev. Lett. **41**, 1396 (1978).

[20] A. Pasquarello, M. S. Hybertsen, and R. Car, Appl. Phys. Lett. **68**, 625 (1996).

[21] A. Pasquarello, M. S. Hybertsen, and R. Car, Appl. Surf. Sci. **104/105**, 317 (1996).

[22] A. Pasquarello and M. S. Hybertsen, in *The Physics and Chemistry of SiO_2 and the Si-SiO_2 Interface-4*, edited by H.Z. Massoud, I. Baumvol, M. Hirose, and E. H. Poindexter, (Electrochem. Soc. Pennington, 2000), p. 271.

[23] A. Pasquarello, M. S. Hybertsen, and R. Car, Nature (London) **396**, 58 (1998).

[24] R. Buczko, S. J. Pennycook, and S. T. Pantelides, Phys. Rev. Lett. **84**, 943 (2000).

[25] Y. Tu and J. Tersoff, Phys. Rev. Lett. **84**, 4393 (2000).

[26] T. Yamasaki, C. Kaneta, T. Uchiyama, T. Uda, and K. Terakura, Phys. Rev. B **63**, 115314 (2001).

[27] M. Hane, Y. Miyamoto, and A. Oshiyama, Phys. Rev. B **41**, 12637 (1990).

[28] K. O. Ng and D. Vanderbilt, Phys. Rev. B **59**, 10132 (1999).

[29] T. Watanabe, H. Fujiwara, H. Noguchi, T. Hoshino, and I. Ohdomari, Jpn. J. Appl. Phys. **38**, L366 (1999).

[30] T. Watanabe and I. Ohdomari, Thin Solid Films **343-344**, 370 (1999).

[31] A. Bongiorno and A. Pasquarello, Appl. Phys. Lett. **83**, 1417 (2003).

[32] A. Bongiorno, A. Pasquarello, M. S. Hybertsen, and L. C. Feldman, Phys. Rev. Lett. **90**, 186101 (2003).

[33] C. M. Perkins, B. B. Triplett, P. C. Mclntyre, K. C. Saraswat, S. Haukka, and M. Tuominen, Appl. Phys. Lett. **78**, 2357 (2001).

[34] H. S. Chang, H. D. Yang, H. Hwang, H. M. Cho, H. J. Lee, and D. W. Moon, J. Vac. Sci. Technol. B **20**, 1836 (2002).

[35] K. Hirose, H. Kitahara, and T. Hattori, Phys. Rev. B **67**, 195313 (2003).

[36] J. R. Jameson, W. Harrison, and P. B. Griffin, J. Appl. Phys. **92**, 4431 (2002).

[37] Y. J. Chabal, Surf. Sci. Rep. **8**, 211 (1988).

[38] S. Abbet, U. Heiz, H. Häkkinen, and U. Landman, Phys. Rev. Lett. **25**, 5950 (2001).

[39] B. H. Erné, F. Ozanam, and J.-N. Chazalviel, Phys. Rev. Lett. **80**, 4337 (1998).

[40] Y. J. Chabal and K. Raghavachari, Surf. Sci. **502**, 41 (2002).

[41] C. T. Kirk, Phys. Rev. B **38**, 1255 (1988).

[42] K. T. Queeney, M. K. Weldon, J. P. Chang, Y. J. Chabal, A. B. Gurevich, J. Sapjeta, and R. L. Opila, J. Appl. Phys. **87**, 1322 (2000).

[43] H. Ono, T. Ikarashi, K. Ando, and T. Kitano, J. Appl. Phys. **84**, 6064 (1998).

[44] R. A. B. Devine, Appl. Phys. Lett. **68**, 3108 (1996).

[45] I. W. Boyd and J. I. B. Wilson, J. Appl. Phys. **62**, 3195 (1987).

[46] S. Miyazaki, H. Nishimura, M. Fukuda, L. Ley, and J. Ristein, Appl. Surf. Sci. **113/114**, 585 (1997).

[47] T. Owhaki, M. Takeda, and Y. Takai, Jpn. J. Appl. Phys. **36**, 5507 (1997).

[48] A. R. Chowdhuri, D.-U. Jin, J. Rosado, and C. G. Takoudis, Phys. Rev. B **67**, 245305 (2003).

[49] C. Martinet and R. A. B. Devine, J. Appl. Phys. **77**, 4343 (1995).

[50] D. E. Aspnes, J. B. Theeten, and F. Hottier, Phys. Rev. B **20**, 3292 (1979).

[51] K. T. Queeney, N. Herbots, J. M. Shaw, V. Atluri, and Y. J. Chabal, Appl. Phys. Lett. **84**, 493 (2004).

[52] X. Gonze and C. Lee, Phys. Rev. B **55**, 10355 (1997).

[53] P. Umari and A. Pasquarello, Phys. Rev. Lett. **89**, 157602 (2002).

[54] S. Baroni, S. de Gironcoli, A. Dal Corso, and P. Giannozzi, Rev. Mod. Phys. **73**, 515 (2001).

[55] A. Pasquarello and R. Car, Phys. Rev. Lett. **79**, 1766 (1997).

[56] N. Marzari and D. Vanderbilt, Phys. Rev. B **56**, 12847 (1997).

[57] L. L. Hirst, Rev. Mod. Phys. **69**, 607 (1997).

[58] P. Umari, A. Dal Corso, and R. Resta, in *Proceedings of the 11th Williamsburg workshop on fundamental physics of ferroelectrics*, (APS, Williamsburg, 2001), Vol. 582, p. 107.

[59] G. Nenciu, Rev. Mod. Phys. **63**, 91 (1991).

[60] R. W. Nũnes and D. Vanderbilt, Phys. Rev. Lett. **73**, 712 (1994).

[61] I. Souza, J. Iñiguez, and D. Vanderbilt, Phys. Rev. Lett. **89**, 117602 (2002).

[62] P. Fernández, A. Dal Corso, and A. Baldereschi, Phys. Rev. B **58**, R7480 (1998).

[63] R. D. King-Smith and D. Vanderbilt, Phys. Rev. B **47**, 1651 (1993).

[64] C. Sgiarovello, M. Peressi, and R. Resta, Phys. Rev. B **64**, 115202 (2001).

[65] P. Ghosez, J-P. Michenaud, and X. Gonze, Phys. Rev. B **58**, 6224 (1998).

[66] A. A. Maradudin, E. W. Montroll, G. H. Weiss, and I. P. Ipatova, in *Solid State Physics: Advances in Research and Applications*, edited by H. E. Ehrenreich, F. Seitz, and D. Turnbull (Academic, New York, 1971), Suppl. 3, Chap. 4.

[67] J.P. Perdew and Y. Wang, Phys. Rev. B **46**, 12947 (1992).

[68] A. Pasquarello, K. Laasonen, R. Car, C. Lee, and D. Vanderbilt, Phys. Rev. Lett. **69**, 1982 (1992).

[69] K. Laasonen, A. Pasquarello, R. Car, C. Lee, and D. Vanderbilt, Phys. Rev. B **47**, 10142 (1993).

[70] A. Dal Corso, A. Pasquarello, A. Baldereschi, and R. Car, Phys. Rev. B **53**, 1180 (1996).

[71] D. Vanderbilt, Phys. Rev. B **41**, 7892 (1990).

[72] R. Car and M. Parrinello, Phys. Rev. Lett. **55**, 2471 (1985).

[73] R. Resta, Ferroelectrics **136**, 51 (1992).

[74] R. Resta, Rev. Mod. Phys. **66**, 899 (1994).

[75] F. Gygi, J.-L. Fattebert, and E. Schwegler, Comput. Phys. Comm. **155**, 1 (2003).

[76] R. Resta, Phys. Rev. Lett. **80**, 1800 (1998).

[77] P. Umari and A. Pasquarello, Phys. Rev. B **68**, 85114 (2003).

[78] A. Dal Corso, S. Baroni, and R. Resta, Phys. Rev. B **49**, 5323 (1994).

[79] Z. H. Lu, D. J. Lockwood, and J.-M. Baribeau, Nature (London) **378**, 258 (1995).

[80] P. Carrier, L. J. Lewis, and M. W. C. Dharma-Wardana, Phys. Rev. B **64**, 195330 (2001).

[81] R. Tsu, D. Babić, and L. Ioriatti, Jr., J. Appl. Phys. **82**, 1327 (1997).

[82] L.-W. Wang and A. Zunger, Phys. Rev. Lett. **73**, 1039 (1994).

[83] M. Lannoo, C. Delerue, and G. Allan, Phys. Rev. Lett. **74**, 3415 (1995).

[84] C. Delerue, M. Lannoo, and G. Allan, Phys. Rev. B **68**, 115411 (2003).

[85] B. K. Agrawal and S. Agrawal, Appl. Phys. Lett. **77**, 3039 (2000).

[86] D. W. Berreman, Phys. Rev. **130**, 2193 (1963).

[87] R. Ruppin and R. Englman, Rep. Prog. Phys. **33**, 149 (1970).

[88] E. Burstein, S. Iwasa, and Y. Sawada, in *Proceedings of the E. Fermi International School of Physics, Course XXXIV, Optical Properties of Solids, Varenna, 1965*, edited by J. Tauc (Academic, New York, 1966), p. 431.

[89] A. Debernardi, Phys. Rev. B **57**, 12847 (1998).

[90] W. Cochran and R. A. Cowley, J. Phys. Chem. Solids **23**, 447 (1962).

[91] J. P. Perdew and A. Zunger, Phys. Rev. B **23**, 5048 (1981).

[92] F. Favot and A. Dal Corso, Phys. Rev. B **60**, 11427 (1999).

[93] G. B. Bachelet, D. R. Hamann, and M. Schlüter, Phys. Rev. B **26**, 4199 (1982).

[94] P. A. V. Johnson, A. C. Wright, and R. N. Sinclair, J. Non-Cryst. Solids **58**, 109 (1983).

[95] F. Mauri, A. Pasquarello, B. G. Pfrommer, Y. Yoon, and S. G. Louie, Phys. Rev. B **62**, R4786 (2000).

[96] N. Tit and M. W. C. Dharma-Wardana, J. Appl. Phys. **86** 387 (1999).

[97] A. Bongiorno and A. Pasquarello, Phys. Rev. B **62**, R16326 (2000).

[98] L. Colombo, R. Resta, and S. Baroni, Phys. Rev. B **44**, 5572 (1991).

[99] S. Tang, R. M. Wallace, A. Seabaugh, and D. King-Smith, Appl. Surf. Sci. **135**, 137 (1998).

[100] J. W. Keister, J. E. Rowe, J. J. Kolodziej, H. Niimi, T. E. Madey, and G. Lucovsky, J. Vac. Sci. Technol. B **17**, 1831 (1999).

[101] V. V. Afanas'ev, M. Houssa, A. Stesmans, and M. M. Heyns, Appl. Phys. Lett. **78**, 3073 (2001).

[102] B. R. Tuttle, Phys. Rev. B **67**, 155324 (2003).

[103] M. Watarai, J. Nakamura, and A. Natori, Phys. Rev. B **69**, 35312 (2004).

[104] N. Awaji, S. Ohkubo, T. Nakanishi, Y. Sugita, K. Takasaki, and S. Komiya, Jpn. J. Appl. Phys. **35**, L67 (1996).

[105] S. D. Kosowsky, P. S. Pershan, K. S. Krish, J. Bevk, M. L. Green, D. Brasen, and L. C. Feldman, Appl. Phys. Lett. **70**, 3119 (1997).

[106] P. Vashishta, R. K. Kalia, J. P. Rinó, and I. Ebbsjö, Phys. Rev. B **41**, 12197 (1990).

[107] S. Nosé, J. Chem. Phys. **81**, 511 (1984).

[108] W. G. Hoover, Phys. Rev. A **31**, 1695 (1985).

[109] A. Bongiorno, A. Pasquarello, M. S. Hybertsen, and L. G. Feldman, Microelectron. Eng. **72**, 197 (2004).

[110] K. Nakajima, S. Joumori, M. Suzuki, K. Kimura, T. Osipowicz, K. L. Tok, J. Z. Zheng, A. See, and B. C. Zhang, Appl. Phys. Lett. **83**, 296 (2003).

[111] A. Bongiorno and A. Pasquarello, Appl. Surf. Sci. **234**, 190 (2004).

[112] L. J. Sham and M. Schlüter, Phys. Rev. B **32**, 3883 (1985).

[113] B. R. Tuttle, Phys. Rev. B **70**, 125322 (2004).

[114] M. L. Green, T. W. Sorsch, G. L. Timp, D. A. Muller, B. E. Weir, P. J. Silverman, S. V. Moccioi, and Y. O. Kim, Microelectron. Eng. **48**, 25 (1999).

[115] J. K. Tomfohr and O. F. Sankey, Phys. Stat. Sol. B **233**, 59 (2002).

[116] X. Gonze, D. C. Allan, and M. P. Teter, Phys. Rev. Lett. **68**, 3603 (1992).

[117] J. Bardeen, Phys. Rev. **71**, 717 (1947).

[118] V. Heine, Phys. Rev. **138A**, 1689 (1965).

[119] A. M. Cowley and S. M. Sze, J. Appl. Phys. **36**, 3212 (1965).

[120] S. Kurtin, T. C. McGill, and C. A. Mead, Phys. Rev. Lett. **22**, 1433 (1969).

[121] M. Schlüter, Phys. Rev. B **17**, 5044 (1978).

[122] W. Mönch, Phys. Rev. Lett. **58**, 1260 (1987).

[123] W. Mönch, Surf. Sci. **299**, 928 (1994).

[124] C. Berthod, N. Bingeli, and A. Baldereschi, Europhys. Lett. **36**, 67 (1996).

[125] X. Gonze, P. Ghosez, and R. W. Godby, Phys. Rev. Lett. **74**, 4035 (1995).

[126] H. Harris, K. Choi, N. Mehta, A. Chandolu, N. Biswas, G. Kipshidze, S. Nikishin, S. Gangopadhyay, and H. Temkin, Appl. Phys. Lett. **81**, 1065 (2002).

[127] K. Eisenbeiser, J. M. Finder, Z. Yu, J. Ramdani, J. A. Curless, J. A. Hallmark, R. Droopad, W. J. Ooms, L. Salem, S. Bradshaw, and C. D. Overgaard, Appl. Phys. Lett. **76**, 1324 (2000).

[128] K. Yamamoto, S. Hayashi, M. Niwa, M. Asai, S. Horii, and H. Miya, Appl. Phys. Lett. **83**, 2229 (2003).

[129] D. E. Aspnes and J. B. Theeten, Phys. Rev. Lett. **43**, 1046 (1979).

[130] W. A. Kamitakahara, H. R. Shanks, J. F. McClelland, U. Buchenau, F. Gompf, and L. Pintschovius, Phys. Rev. Lett. **52**, 644 (1984).

[131] W. A. Kamitakahara, C. M. Soukoulis, H. R. Shanks, U. Buchenau, and G. S. Grest, Phys. Rev. B **36**, 6539 (1987).

[132] J. M. Carpenter and D. L. Price, Phys. Rev. Lett. **54**, 441 (1985).

[133] U. Buchenau, M. Prager, N. Nücker, A. J. Dianoux, N. Ahmad, and W. A. Phillips, Phys. Rev. B **34**, 5665 (1986).

[134] A. Pasquarello, J. Sarnthein, and R. Car, Phys. Rev. B **57**, 14133 (1998).

[135] J. Sarnthein, A. Pasquarello, R. Car, Science **275**, 1925 (1997).

[136] R. J. Bell, P. Dean, and D. C. Hibbins-Butler, J. Phys. C **4**, 1214 (1971).

[137] P. G. Pai, S. S. Chao, Y. Takagi, and G. Lucovsky, J. Vac. Sci. Technol. A **4**, 689 (1986).

[138] H. R. Philipp, J. Appl. Phys. **50**, 1053 (1979).

[139] M. Nakamura, Y. Mochizuki, K. Usami, Y. Itoh, and T. Nozaki, Solid State Commun. **50**, 1079 (1984).

[140] J.-P. R. Wells, E. D. van Hattum, P. J. Phillips, D. A. Carder, F. H. P. M. Habraken, and J. I. Dijkhuis, J. Lumin. **108**, 173 (2004).

[141] L. Schumann, A. Lehmann, H. Sobotta, V. Riede, U. Teschner, and K. Hübner, Phys. Stat. Sol. B **110**, K69 (1982).

[142] G. Lucovsky, J. T. Fitch, E. Kobeda, and E. A. Irene, in *The Physics and Chemistry of SiO_2 and the Si-SiO_2 Interface*, edited by C. R. Helms and B. E. Deal (Plenum, New York, 1988), p. 139.

[143] P. N. Sen and M. F. Thorpe, Phys. Rev. B **15**, 4030 (1977).

[144] F. L. Galeener, Phys. Rev. B **19**, 4292 (1979).

[145] C. Kittel, *Introduction to Solid State Physics*, (Wiley, New York, 1986), p. 89.

[146] R. Resta, Phys. Rev. B **16**, 2717 (1977).

[147] D. R. Penn, Phys. Rev. B **128**, 2093 (1962).

[148] S. H. Wemple and M. Di Domenico, Jr., Phys. Rev. B **3**, 1338 (1971).

[149] I. Souza, T. Wilkens, and R. M. Martin, Phys. Rev. B **62**, 1666 (2000).

[150] A. Baldereschi, S. Baroni, and R. Resta, Phys. Rev. Lett. **61**, 734 (1988).

[151] C. M. Grinstead and J. L. Snell, *Introduction to Probability*, (American Mathematical Society, 1997), p. 291 and p. 345.

[152] W. Kohn, Phys. Rev. **115**, 809 (1959).

[153] R. Resta, *Berry's phase and geometric quantum distance: macroscopic polarization and electron localization*, Lecture Notes for the "Troisième Cycle de la Physique en Suisse Romande" (Lausanne, 2000).

[154] O. V. Dolgov and E. G. Maksimov, in *The Dielectric Function of Condensed Systems*, edited by L. V. Keldysh, D. A. Kirzhnitz, and A. A. Maradudin, (North-Holland, Amsterdam, 1989), Secs. 2.1 and 4.1.

[155] G. D. Wilk and R. M. Wallace, Appl. Phys. Lett. **76**, 112 (2000).

[156] M. Gutowski, J. E. Jaffe, C. Liu, M. Stoker, R. I. Hegde, R. S. Rai, and P. J. Tobin, Appl. Phys. Lett. **80**, 1897 (2002).

[157] J. P. Chang and Y. S. Lin, Appl. Phys. Lett. **79**, 3824 (2001).

[158] T. Yamaguchi, H. Satake, N. Fukushima, and A. Toriumi, Appl. Phys. Lett. **80**, 1987 (2002).

[159] R. L. Opila, G. D. Wilk, M. A. Alam, R. B. van Dover, and B. W. Busch, Appl. Phys. Lett. **81**, 1788 (2002).

[160] G. B. Rayner, Jr., D. Kang, Y. Zhang, and G. Lucovsky, J. Vac. Sci. Technol. B **20**, 1748 (2002).

[161] H. Kato, T. Nango, T. Miyagawa, T. Katagiri, K. S. Seol, and Y. Ohki, J. Appl. Phys. **92**, 1106 (2002).

[162] E. Pehlke and M. Scheffler, Phys. Rev. Lett. **71**, 2338 (1993).

[163] M. Nogami, J. Non Crystall. Sol. **69**, 415 (1985).

[164] G. Lucovsky and G. B. Rayner, Jr., Appl. Phys. Lett. **77**, 2912 (2000).

[165] H. A. Kurtz and R. A. B. Devine, Appl. Phys. Lett. **79**, 2342 (2001).

[166] J. M. Delaye and D. Ghaleb, Phys. Rev. B **61**, 14481 (2000).

[167] M. J. Guittet, J. P. Crocombette, and M. Gautier-Soyer, Phys. Rev. B **63**, 25117 (2001).

Acknowledgements

I am grateful to Professor Alfredo Pasquarello for providing me with guidance and support during the last four years. I had the privilege to discuss with him almost every day, and I greatly appreciated his tremendous pragmatism and his contagious enthusiasm.

I would also like to thank Professor Alfonso Baldereschi for giving me the opportunity to practice teaching with undergraduate students. I always enjoyed his precious advices during these years, and I appreciated its kindness and availability to discuss when I had to make a decision for the future.

I am indebted to many friends and colleagues of IRRMA for the stimulating and funny working atmosphere, Paolo, Massimiliano, Stephane, Claudia, Luigi, Fabien, Julien, Vincent, Zeljiko, Giovanni, Giuseppe, Nicolas, Cedric, Andreas and Jean-Baptiste. I am especially grateful to Angelo for the patience and the willingness he demonstrated during the first months of my doctorate. Many thanks go also to Carol Bonzon, Suzanne Claudet and Noemi Porta for their help during these years.

A special thank goes to all the "non-academic" friends that I met during my stay in Lausanne, Stephane, Philippe, Elena, Joanne, Antoine, Virginie, Blaise, Jo-Anne, Davide M., Nicoletta, Laura, Davide D.C., Isabelle, and to my unbreakable high-school friends Cristian, Marco, Federico, Luca, Vanni. Despite the distance which separate us, they still represent my best friends.

Without the continuous support and encouragement of my family I would have not arrived here. A big thank goes to Anna, Laila and Nicola for being the most amazing, friendly and funny family I know.

I would like to conclude this thesis by expressing my gratitude to Natacha. Meeting her five years ago has been a turning point in my life. This thesis is for her.

Curriculum Vitae

Name Feliciano Giustino

Nationality Italian

Date of birth February 22, 1976

Affiliations Institut de Théorie des Phénomènes Physiques, Ecole Polytechnique Fédérale de Lausanne (EPFL), and Institut Romand de Recherche Numérique en Physique des Matériaux (IRRMA), Lausanne, Switzerland.

2001–2005 Ph.D. Physics, Ecole Polytechnique Fédérale de Lausanne (EPFL), Lausanne, Switzerland.
Thesis: *Infrared Properties of the Si(100)-SiO_2 Interface from First-Principles.*
Advisor: Prof. A. Pasquarello.

2000–2001 Engineer, Microelectronic Group, European Laboratory for Particle Physics (CERN), Geneva, Switzerland.
Research project: *Experimental characterization of the effects of X-ray, proton and neutron irradiations on bipolar transistors.*
Supervisors: Dr. P. Jarron, Dr. F. Faccio.

1995–2001 M.S. Nuclear Engineering, Politecnico di Torino, Torino, Italy.
Thesis: *Radiation Effects on Semiconductor Devices: Study of the Enhanced Low Dose-Rate Sensitivity.*
Advisor: Prof. P. Quarati.

Publications related to the thesis

[1] F. Giustino, A. Bongiorno, and A. Pasquarello, *Modeling of Si 2p core-level shifts at $Si/(ZrO_2)_x(SiO_2)_{1-x}$ interfaces*, Appl. Phys. Lett. **81**, 4233 (2002).

[2] F. Giustino, P. Umari, and A. Pasquarello, *Dielectric discontinuity at interfaces in the atomic-scale limit: Permittivity of ultrathin oxide films on silicon*, Phys. Rev. Lett. **91**, 267601 (2003).

[3] F. Giustino and A. Pasquarello, *Atomic-scale investigation of the dielectric screening at the interface between silicon and its oxide*, Mat. Res. Soc. Symp. Proc. **786**, E5.1.1 (2004).

[4] F. Giustino, P. Umari, and A. Pasquarello, *Dielectric effect of a thin SiO_2 interlayer at the interface between silicon and high-κ oxides*, Microel. Eng. **72**, 300 (2004).

[5] F. Giustino, A. Bongiorno, and A. Pasquarello, *Electronic structure at realistic Si(100)-SiO_2 interfaces*, Jap. J. of Appl. Phys. **43**, 7895 (2004).

[6] F. Giustino, A. Bongiorno, and A. Pasquarello, *Atomic-scale modelling of the Si(100)-SiO_2 interface*, to appear in the Proceedings of the 27th International Conference on the Physics of Semiconductors (ICPS-27, Flagstaff, AZ, 2004).

[7] F. Giustino and A. Pasquarello, *Theory of atomic-scale dielectric permittivity at insulator interfaces*, Phys. Rev. B **71**, 144104 (2005).

[8] F. Giustino, A. Bongiorno, and A. Pasquarello, *Atomistic models of the Si(100)-SiO_2 interface: structural, electronic and dielectric properties*, J. Phys.: Condens. Matter. **17**, S2065 (2005).

[9] F. Giustino, A. Bongiorno, and A. Pasquarello, *Equivalent oxide thickness of a thin oxide interlayer in gate insulator stacks on silicon*, Appl. Phys. Lett. **86**, 192901 (2005).

[10] F. Giustino and A. Pasquarello, *Infrared properties of ultrathin oxides on Si(100)*, Microel. Eng. **80**, 420 (2005).

[11] F. Giustino and A. Pasquarello, *Electronic and dielectric properties of a suboxide interlayer at the silicon-oxide interface in MOS devices*, to appear in Surf. Sci.

Other publications

[1] J. Böch, F. Saigné, T. Maurel, F. Giustino, L. Dusseau, R. D. Schrimpf, K. F. Galloway, J. P. David, R. Ecoffet, J. Fesquet, and J. Gasiot, *Dose and dose-rate effects on NPN bipolar junction transistors irradiated at high temperature*, IEEE Trans. Nucl. Sci. **49**, 1474 (2002).

[2] J. Böch, F. Saigné, V. Mannoni, F. Giustino, R. D. Schrimpf, L. Dusseau, K. F. Galloway, J. Fesquet, J. Gasiot, and R. Ecoffet, *Model for high-temperature radiation effects in NPN bipolar junction transistors*, IEEE Trans. Nucl. Sci. **49**, 2990 (2002).

[3] F. Devynck, F. Giustino, and A. Pasquarello, *Abrupt model interface for the 4H(1000)SiC-SiO_2 interface*, Microel. Eng. **80**, 38 (2005).

Invited talks at international conferences

[1] *Equivalent Oxide Thickness of a suboxide layer at the interface between Si and SiO_2*, Workshop on Atomistic Processes at semiconductor/oxide interfaces for microelectronics devices, Centre Européen de Calcul Atomique et Moleculaire (CECAM), September 2004, Lyon, France.

[2] *Dielectric permittivity at surfaces et interfaces*, XXV International Workshop on Computational Physics and Material Science: Total Energy and Force Methods, January 2005, Trieste, Italy.

Contributed talks at international conferences

[1] *Si-2p core-level shifts at $Si/(ZrO_2)_x(SiO_2)_{1-x}$ interfaces*, Semiconductor Interface Specialists Conference (SISC), December 2002, San Diego, CA.

[2] *Dielectric effect of a thin SiO_2 interlayer at the interface between silicon and high-κ oxides*, Insulating Films on Semiconductors Conference (INFOS), June 2003, Barcelona, Spain.

[3] *Dielectric permittivity of atomic-layer thin SiO_2 films on silicon substrates, Workshop on the position operator in extended systems*, Centre Européen de Calcul Atomique et Moleculaire (CECAM), September 2003, Lyon, France.

[4] *Atomic-scale investigation of the dielectric screening at the interface between silicon and its oxide*, Material Research Society (MRS) Fall Meeting, December 2003, Boston, MA.

[5] *Infrared absorption spectra at interfaces from first principles: Origin of LO and TO red shifts in ultrathin oxide films on silicon*, American Physical Society (APS) March Meeting, March 2005, Los Angeles, CA.